MAGNETIC, THERMAL, STRUCTURAL AND ELECTRICAL PROPERTIES OF UNDOPED AND DOPED EuTi$_{1-x}$M$_x$O$_3$ (M= Nb, V)

By

Susmita Roy

PHYS05201304006

Condensed Matter Physics Division

Saha Institute of Nuclear Physics, Kolkata

A thesis submitted to the
Board of Studies in Physical Sciences

In partial fulfillment of the requirements
For the Degree of

DOCTOR OF PHILOSOPHY

of

HOMI BHABHA NATIONAL INSTITUTE

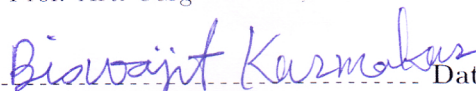March, 2019

Homi Bhabha National Institute
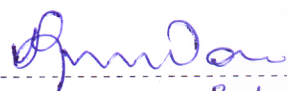
Recommendations of the Viva Voce Board

As members of the Viva Voce Board, we recommend that the dissertation prepared by **Susmita Roy** entitled "**Magnetic, thermal, structural and electrical properties of undoped and doped EuTi$_{1-x}$M$_x$O$_3$ (M= Nb, V)**" may be accepted as fulfilling the dissertation requirement for the Degree of Doctor of Philosophy.

-- Date : 14.06.2019

Chairman : Prof. Pradeep Kumar Mohanty

P. Mondal -- Date : 14.06.2019

Guide : Prof. Prabhat Mandal

-- Date : 14/6/2019

Member : Prof. Arti Garg

Biswajit Karmakar Date : 14/6/19

Member : Prof. Biswajit Karmakar

-- Date : 14.06.2019

External Examiner : Prof. A. SUNDARESAN

Final approval and acceptance of this dissertation is contingent upon the candidate's submission of the final copies of the dissertation to HBNI.

I hereby certify that I have read this dissertation prepared under my direction and recommend that it may be accepted as fulfilling the dissertation requirement.

P. Mandal -- Date : 14.06.2019 (Kolkata)

Guide : Prof. Prabhat Mandal

STATEMENT BY AUTHOR

This dissertation has been submitted in partial fulfillment of requirements for an advanced degree at Homi Bhabha National Institute (HBNI) and is deposited in the library to be made available to borrowers under rules of the HBNI.

Brief quotations from this dissertation are allowable without special permission, provided that accurate acknowledgement of source is made. Requests for permission for extended quotation from or reproduction of this manuscript in whole or in part may be granted by the Competent Authority of HBNI when in his or her judgment the proposed use of the material is in the interests of scholarship. In all other instances, however, permission must be obtained from the author.

Susmita Roy

Susmita Roy

DECLARATION

I, hereby, declare that the investigation presented in the thesis has been carried out by me. The work is original and the work has not been submitted earlier as a whole or in part for a degree/diploma at this or any other Institution or University.

Susmita Roy
Susmita Roy

List of Publications arising from the thesis

Journal

1. "Giant low-field magnetocaloric effect in single-crystalline $EuTi_{0.85}Nb_{0.15}O_3$", Susmita Roy, N. Khan, and P. Mandal, *APL MATERIALS* **4**, 026102 (2016).

2. "Large low-field magnetic refrigeration in ferromagnetic insulator $EuTi_{0.9}V_{0.1}O_3$", Susmita Roy, M. Das, and P. Mandal, *PHYSICAL REVIEW MATERIALS* **2**, 064412 (2018).

3. "Unconventional transport properties of the itinerant ferromagnet $EuTi_{1x}Nb_xO_3$ ($x = 0.10$-0.20)", Susmita Roy, Nazir Khan, and Prabhat Mandal, *PHYSICAL REVIEW B* **98**, 134428 (2018).

Chapters in books and lecture notes

NIL

Conferences

1. **Oral Presentation**
   at the International Meeting on Highly Correlated Systems-2017 (IMHCS-2017), "Itinerant Ferromagnetism in Strongly Correlated $EuTi_{1-x}Nb_xO_3 (x = 0.15)$ Single Crystal", Susmita Roy, Nazir Khan, and Prabhat Mandal.

2. **Oral Presentation**
   at the Condensed Matter Days- 2017 (CMDAYS17), "Giant low-field magnetocaloric effect in single crystalline $EuTi_{0.85}Nb_{0.15}O_3$", Susmita Roy, Nazir Khan, and Prabhat Mandal.

3. **Oral Presentation**
   at the conference on Magnetism and Magnetic Materials (MMM 2017), "Itinerant Ferromagnetism in Strongly Correlated $EuTi_{1-x}Nb_xO_3$ Single Crystal", Susmita Roy, Nazir Khan, and Prabhat Mandal.

4. **Poster Presentation**
   at the International Conference on Condensed Matter Physics (ICCMP) , "Itinerant ferromagnetism in strongly correlated $EuTi_{1-x}Nb_xO_3$ (x= 0.15) single crystal", Susmita Roy, Nazir Khan, and Prabhat Mandal.

Others

1. "Analysis of critical behavior associated with the antiferromagnetic and structural phase transition of single crystalline $EuTiO_3$",
   Susmita Roy, Nazir Khan, Arindam Midya, and Prabhat Mandal. (under preparation)

Susmita Roy
Susmita Roy

Dedicated to
my beloved parents, elder sister,
and
Husband

ACKNOWLEDGEMENTS

Contents

SYNOPSIS

Introduction: In recent times, rare-earth titanates (RTiO$_3$) with perovskite structure (ABO$_3$) received considerable attention due to the interplay between charge, orbital and spin degrees of freedoms [1, 2]. Usually, in RTiO$_3$, both R and Ti ions are in trivalent states. But, EuTiO$_3$ (ETO) is somehow exceptional among the perovskite titanates where Eu is divalent and Ti is tetravalent. ETO is a quantum paraelectric and band insulator. ETO has been studied extensively due to the observation of large magneto-dielectric effect below the antiferromagnetic (AFM) ordering temperature T_N=5.5 K [3, 4]. Also, the biaxial-strain induced multiferrocity has been reported in the thin films of ETO [5]. Theoretical studies on the observed positive value of Curie-Weiss temperature (θ_{CW}) reveal that the next-to-nearest neighbor ferromagnetic (FM) interaction is slightly larger than the nearest neighbor AFM interaction which makes the ground state very unstable against any perturbation [6]. Therefore, chemical doping at A or B or O site in ETO will be an effective way to tune the magnetic as well as transport properties. Substitution of a heterovalent ion at A site transfers either hole or electron to the transition metal ion site which increases the conductivity of the system. There already exists several reports on chemical doping at A site (Eu^{2+}). As examples, doping with La^{3+} and Gd^{3+} at A site transform ETO into a FM metallic system [6, 7]. In contrary to this, normally B site substitution creates disorder which favors carrier localization effect. As a consequence, insulator to metal transition with B site doping is a rare phenomenon. Therefore, our main focus is to dope foreign atoms at Ti site of ETO and study different physical properties of in details.

Experimental Details: In the present thesis, we have doped Nb^{4+} and V^{4+} at

Ti^{4+} site of ETO. In this regard, we have synthesized single crystalline $EuTiO_3$ and $EuTi_{1-x}Nb_xO_3$ ($x = 0.10, 0.15, 0.20$) (ETNO) and polycrystalline $EuTi_{0.9}V_{0.1}O_3$ (ETVO). Polycrystalline samples were prepared in conventional solid state reaction method. Then, single crystals were grown by travelling solvent floating zone method in a four-mirror float zone image furnace. All the heat treatments were done in the reduced atmosphere (5% H_2 and 95% Ar) to obtain Eu^{2+} instead of Eu^{3+}. Phase purity and the structural analysis are done by using high-resolution powder XRD. The magnetization has been measured in a SQUID-VSM whereas electrical and thermal transport measurements were done by standard four-probe technique in a 9 T PPMS. The thermal expansion and magnetostriction have been measured in a cryogen free system by capacitive method using a miniature tilted-plate dilatometer.

Analysis of critical behavior associated with the antiferromagnetic and structural phase transition of single crystalline $EuTiO_3$:

To investigate the effect of magnetic field on the nature of magnetic ground state
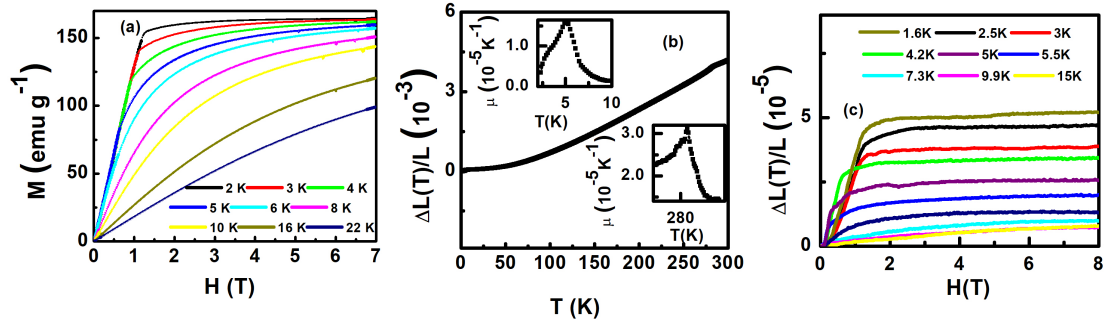
Figure 1: For ETO single crystal (a)M(H) in the vicinity of T_N. (b) T variation of $\Delta L/L$ at zero magnetic field. The upper and lower insets show of μ(T) at T_N and T_S respectively. (c) Magnetic field variation of $\Delta L/L$ across T_N.

of ETO, M is plotted in Fig. 1(a) as a function of H for few representative temper-

atures across the magnetic ordering temperature T_N. It can be seen that below T_N, M increases almost linearly with increasing H but above a critical field H_C it starts to saturate. The value of saturated magnetic moment (M_S) is 7 μ_B/Eu at 2 K and 7 T. The T variation of the thermal expansion $\Delta l/l_{1.5K}$=[L(T)-L$_{1.5K}$]/L$_{1.5K}$ [L$_{1.5K}$ is the sample length at 1.5 K] at zero-field as shown in Fig. 1(b) exhibits two anomalies at T_N=5.78 K due to magnetic ordering and T_S=281 K due to cubic to tetragonal phase transition. We have observed the field variation of $\Delta l/l_{1.5K}$ [not shown] and found that magnetic field has significant influence on the T_N whereas T_S is insensitive. The upper and lower insets of Fig. 1(b) show T dependence of the coefficient of thermal expansion μ=d/dT($\Delta l/l_{1.5K}$) which also reflects sharp λ-like peaks at T_N and T_S. Thus, both the transitions are second order in nature. The field dependence of the thermal expansion, i.e., the magnetostriction ($\Delta l(H)/l_0$=[L(H)-L$_0$]/L$_0$ [L$_0$ = sample length at zero field]), is investigated below and above the T_N in Fig. 1(c). We observe that the magnetostriction is quite large below T_N but decreases rapidly with increasing T. The value of $\Delta l(H)/l_0$ at 1.8 K is as high as 5.2×10^{-5}. There are two distinct regimes. Below T_N and the critical field H_{C_1}=0.2 T, $\Delta l(H)/l_0$ is very small and negative. Above H_{C_1}, $\Delta l(H)/l_0$ increases rapidly up to another critical field H_{C_2}, and then starts to saturate. The nature of $\Delta l(H)/l_0$ mimics M(H) curve as can be seen from Figs. 1(a) and (c).

The magnetic ordering is also reflected in the heat capacity curve as a sharp λ-like anomaly at T_N which is a signature of a second order phase transition and another anomaly at T_S=281 K in the zero-field C_p as shown in Fig. 2(a). With the application of field, the peak broadens and shifts progressively towards higher temperature. To get a clear look of the anomaly at T_S, C_p is plotted in the inset of Fig. 2(a). No field dependence of the T_S is noticeable. The lattice part of the

C_p is deduced by a fitting of combined Debye-Einstein model. As heat capacity measurement is much more sensitive at low temperature, it has been considered for critical study. The experimentally observed C_p is well fitted in the vicinity of T_N to the following equation [8] shown in Fig. 2(b)

$$C_p^* = (A_\pm)|T - T_N|^{-\alpha} + B_\pm + D(T - T_N) \tag{1}$$

where the subscripts + and - stand for $T > T_N$ and $T < T_N$ respectively and α, A, B and D are adjustable parameters. The linear term represents the background contribution to the specific heat, while the last term is the anomalous contribution to the specific heat. This fitting yields the values of the critical exponent α=-0.081 and the critical amplitude ratio A_+/A_-=1.58 which indicate the low temperature magnetic transition corresponds to 3D Heisenberg model.
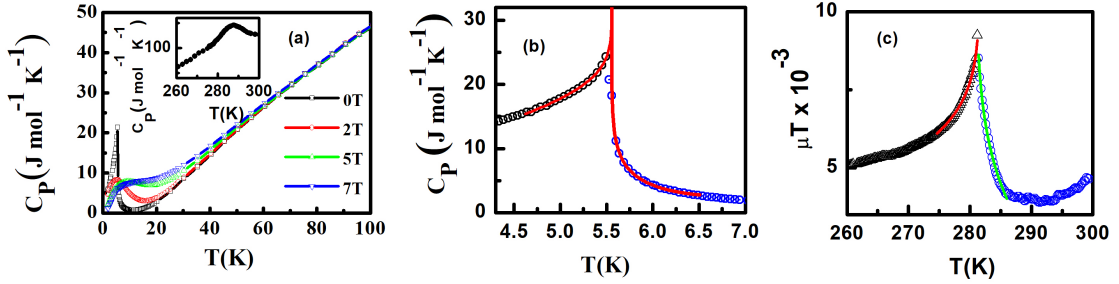
Figure 2: (a) H variation of C_p(T) at different magnetic fields. The inset shows the broad view of anomaly at T_S. Critical analysis (b) of the magnetic phase transition at T_N from C_p(T). The solid line is the fitting of eq.(1) to C_p. (c) of the structural phase transition at T_S from μ(T). The solid lines are the individual fitting of eqs. (2) and (3) respectively for T<T_S and T<T_S.

The critical analysis has been also done for the structural transition. As the peak in C_p is broad and rounded due to the large measuring heat pulses in the thermal relaxation technique, the μ(T) is considered for critical analysis due to its sharpness. Near the transition temperature, μT scales as C_P^* with a scale factor

λ. Therefore, $\mu T \lambda$ is fitted with the same function as C_p^* [9].

$$\mu T = \left(\frac{A_+}{\alpha_+}\right)\left[\left(\frac{T_S - T}{T_S}\right)^{-\alpha} - 1\right] + B \quad \forall \quad T < T_S \tag{2}$$

$$\mu T = \left(\frac{A_-}{\alpha_-}\right)\left[\left(\frac{T - T_S}{T_S}\right)^{-\alpha} - 1\right] + B \quad \forall \quad T > T_S \tag{3}$$

$A_\pm$ and B are the adjustable parameters. The data are individually fitted with the two functions for $T > T_S$ and $T < T_S$ respectively. The fitted curve is shown in Fig. 2(c). From the fitted data, we have calculated the value of $A_+/A_- = 1.58$ and the value of critical exponent α is -0.16. This also suggests that the high temperature structural transition belongs to the 3D Heisenberg family.

Unconventional transport in single-crystalline $EuTi_{1-x}Nb_xO_3$ ($x = 0.10 - 0.20$): It has been shown that Nb doping at Ti^{4+} site destabilizes the AFM ground state of ETO and transforms it into a FM system above a critical doping level $x \sim 0.05$ [10, 11, 12]. However, no detailed magnetic and transport properties have been reported so far. The T dependence of dc magnetic susceptibility ($\chi = M/H$) and the specific heat (C_p) for the ETNO compounds are shown in Figs. 3(a) and (b) respectively. These two figures show that ETNO undergoes a para-to-ferromagnetic transition at Curie temperatures T_C=8, 9.5 and 6 K respectively for x=0.10, 0.15 and 0.20. To understand the correlation between transport and magnetism, the magnetic excitation spectrum has been investigated by estimating the spontaneous magnetization (M_S) using the Arrott plots and the T dependence of M_S is plotted in Fig. 3(c) for x=0.15 as a representative. Well below the T_C, where the critical fluctuation is absent, $M_S(T)$ is fitted well to the Bloch's $T^{3/2}$ law [13]. ρ(T) for all three ETNO crystals is shown in Fig. 4(a). ρ
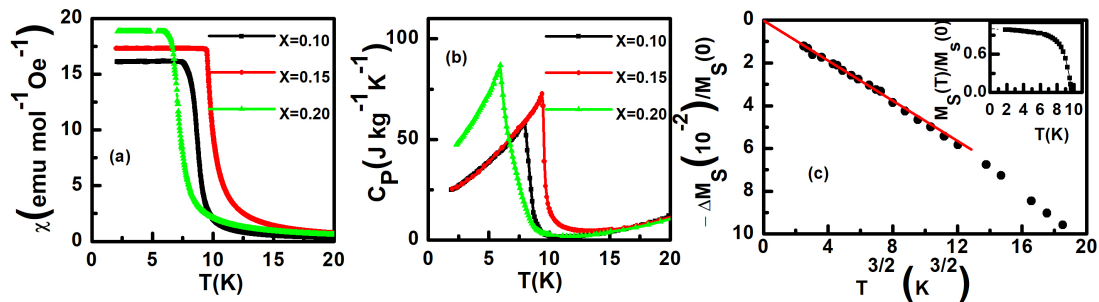
Figure 3: (a) $\chi(T)$ at 50 Oe and (b) C_p at low T for ETNO single crystals. (c) $T^{3/2}$ dependence of ΔM_S for $x = 0.15$ crystal below T_C. Solid line is the fit to Bloch's law. Inset: $M_S(T)$ normalized at T = 0 K.

is metallic over the entire temperature range except a narrow region just above T_C, where a weak increase in ρ has been observed with decreasing T. Just below T_C, ρ drops sharply due to the suppression of spin-disorder scattering. The rate of decrease of ρ in the FM state is much faster than that in the paramagnetic (PM) state. One can notice that ρ in the PM state cannot be fitted with a single power law expression over the entire temperature range. In the PM state above the minima, ρ exhibits a T^2 dependence [Fig. 4(b)] followed by a $T^{3/2}$ dependence at high temperatures [Fig. 4(c)], suggesting a non-Fermi liquid (NFL) behavior. The observed crossover from T^2 to $T^{3/2}$ at high temperatures is quite unusual. Also, we observe T^2 behavior of ρ in the FM state [Fig. 4(d)] which is due to the dominant electron-magnon scattering unlike that observed in the PM state, which is due to the electron-electron scattering. Similar T dependence of ρ has been observed for both $x=$ 0.10 and 0.20 compounds. Unlike the heavy-fermion systems, in many transition metal oxides [14, 15] like $SrRuO_3$ and the present system, no hallmarks of the NFL behavior have been observed in the C_p and χ [16]. This generic NFL behavior is still far from understood and very challenging to explain. In this context, we compare and contrast our results with the $T^{3/2}$ or $T^{5/3}$ dependence of

the ρ, observed away from the magnetic transitions, reported in some oxide and intermetallic itinerant systems [17, 18]. All the three ETNO compounds exhibit a
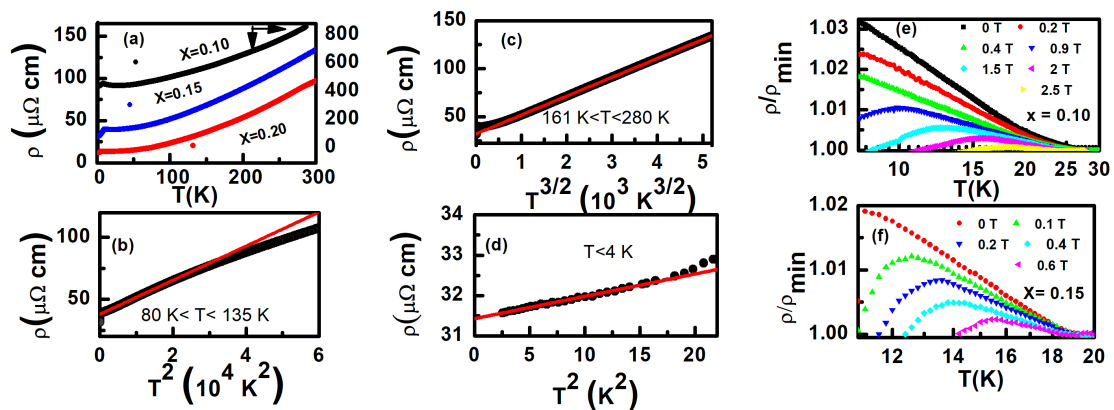
Figure 4: (a)ρ(T) for all the three ETNO crystals. For x = 0.15 crystal, (b) T^2 dependence of ρ in the PM region, (c) $T^{3/2}$ variation of ρ in the PM region, and (d) T^2 fitting to ρ in the FM region. The log(T) dependence of ρ in the range $T_C<T<T_{min}$ at different magnetic fields for the (e) x = 0.10 and (f) x = 0.15 crystals.

unique resistivity minimum at $T = T_{min}$, below which a logarithmic increase in ρ as a function of T is noticed for $T_C<T<T_{min}$ which suppresses strongly with increasing H. This behavior of ρ suggests Kondo scattering of $4d^1$ itinerant electrons of Nb by the localised 4f moments of Eu^{2+}. The effect of magnetic field on the log(T) dependence of ρ is shown for $x=0.10$ and 0.15 compounds, respectively in Figs. 4(e) and (f). Therefore, the present ETNO system is a FM Kondo lattice, which is relatively less numerous and exhibits rather complicated physical pictures [19, 20]. As the increase in ρ below $T = T_{min}$ is marginal for $x=0.20$, the fit in insensitive.

The influence of the magnetic field on ρ is displayed in Fig. 5(a) in which one can see that the sharp anomaly at T_C weakens with increasing field and disappears just above a critical field and the system becomes metallic over the entire temperature
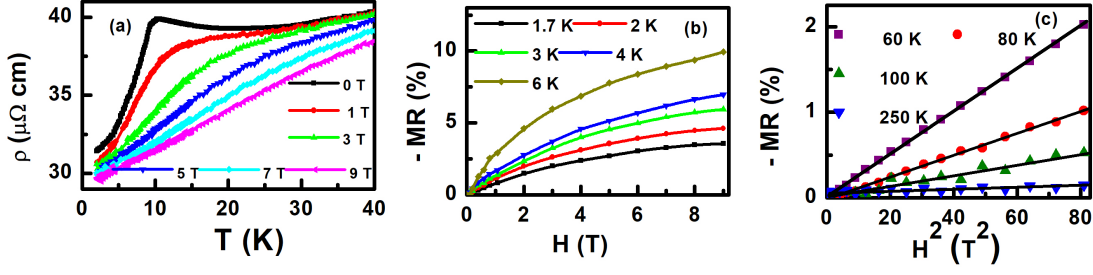
Figure 5: (a) $\rho(T)$ for different magnetic fields. (b) MR versus H below T_C and (c) H^2 dependence of the MR well above T_C for the $x = 0.15$ crystal. Solid black lines correspond to a linear fit.

range. This suggests that the conduction electron is strongly coupled with localized Eu^{2+} spin. Magnetoresistance (MR) defined as $\Delta\rho/\rho=[(\rho(H)-\rho(0))/\rho(0)]$, is small and negative, except in the vicinity of T_C. We have also measured $\Delta\rho/\rho$ in both electron-magnon and electron-electron scattering dominated regions. Well below T_C, where electron-magnon scattering dominates, $\Delta\rho(H)/\rho$ increases rapidly with field and then starts to saturate at high field as shown in Fig. 5(b) for some representative temperatures. $\Delta\rho/\rho$ approximately scales with the magnetization offset $\Delta M_S/M_S(0)$ at low temperature where ρ tends to saturate with field. These observations support spin wave scattering. Contrary to this, the nature of $\Delta\rho(H)/\rho$ curves well above T_C [Fig. 5(c)] is very different. $\Delta\rho/\rho$ is very small and shows H^2 dependence. This relation comes into play as the carriers get scattered by the thermally fluctuating spins. Thus, the presence of several scattering mechanisms and the NFL behavior make ETNO a unique ferromagnetic metallic system.

Giant low-field magnetocaloric effect in single-crystalline $EuTi_{1-x}Nb_xO_3$ ($x = 0.15$) The magnetocaloric effect (MCE) in single crystal of ETNO (x=0.15) has been investigated using M(H)and C_p data. The T dependence of susceptibility (χ) of ETNO (x=0.15) is plotted in Fig. 6(a) which has been already discussed ear-
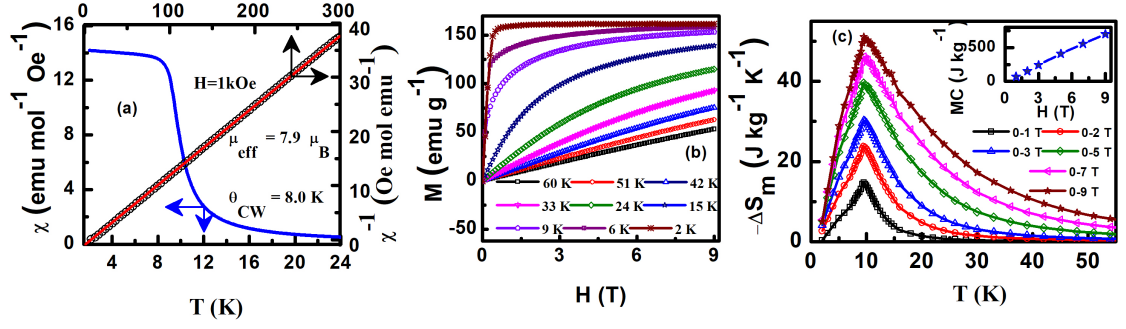
Figure 6: For ETNO (x=0.15) single crystal (a) χ(T) and χ^{-1} at 1 kOe. The solid line is the Curie-Weiss fit. (b) Isothermal magnetization curves. (c) T dependence of the ΔS_m. Inset shows the field variation of MC.

lier. The FM ordering of Eu^{2+} spins in ETNO is mediated by the itinerant electrons of the dopant Nb^{4+}. The high temperature linear fit to the inverse susceptibility (χ^{-1}) in Fig. 6(a) yields the value of θ_{CW}=8 K which is more than two times larger than that in ETO and both have positive θ_{CW}. The effective paramagnetic moment=$P_{eff} = 7.9\mu_B$/Eu for ETNO is closed to the undoped one. In order to investigate the effect of H on the magnetic ground state, isothermal magnetization (M(H))for ETNO for different fields at few representative T across the transition temperature has been plotted in Fig. 6(b). M(H) in ETNO exhibits almost similar behavior as ETO but compared to it M in ETNO increases sharply and gets saturated at lower value of critical field H$_C$ than ETO. The value of saturated magnetic moment (M$_S$) is 7.3 μ_B/Eu at 2 K and 9 T in ETNO which is slightly larger than the expected moment of Eu^{2+}, indicating an additional contribution from the 4d^1 electron of Nb^{4+} [9, 10]. This large value of M with no hysteresis suggests that ETNO (x=0.15) may have large value of MCE parameters. The magnetic entropy change (ΔS_m) for ETNO is calculated from the Maxwell's relation ΔS_m(T,H)= $\int_0^H (\frac{dM}{dT})_H dH$ and plotted against T for different field changes in Fig. 6(c). With

the application of H, the spin entropy is strongly suppressed and a giant ΔS_m is observed near T_C. Both of the ETO and ETNO (x=0.15) exhibit giant MCE [21]. The magnetic cooling/heating capacity (MC) which determines the amount of heat exchange between the cold and hot reservoirs in an ideal heating/cooling cycle depends on the height and width of the peak of the ΔS_m(T) curve and is defined as MC=$\int_{T_1}^{T_2} \Delta S_m dT$ where T_1 and T_2 are the temperatures corresponding to both sides of the half-maximum of the ΔS_m peak. The field variation of MC is shown in the inset of Fig. 6(c). Nb doping at ETO suppresses the value of ΔS_m slightly especially for higher fields but MC enhances due to the broadening of ΔS_m curve than the undoped one [21]. To check the consistency between the values of ΔS_m calculated from M(H) data, the magnetic entropy is recalculated by using the heat capacity data from the following equation

$$S_m(T, H) = S_m(0, H) + \int_0^T \frac{C_m(H, T)}{T} dT \tag{4}$$

where the magnetic contribution of heat capacity (C_m) is estimated by subtracting the lattice part from C_p. The lattice part has been estimated using a combined Debye Einstein model. The ΔS_m calculated from ΔS_m=S$_m$(T,H) - S$_m$(0,H) are comparable with that calculated from M(H) data. To determine the adiabatic temperature change (ΔT_{ad}), we have calculated total zero-field entropy S(0,T) using $\int_0^T \frac{C_P(0,T)}{T} dT$ and then S(H,T) is estimated by subtracting the corresponding ΔS_m determined from M(H) data from the calculated value of S(0,T). Then, the change in temperature for a fixed value of total entropy is the ΔT_{ad}. The values of entropy change ΔS_m and adiabatic temperature change ΔT_{ad} are as high as 51.3 J kg^{-1}K^{-1} and 22 K, respectively, for a field change of 0-9 T. The corresponding MC is 700 J kg^{-1}. This compound also shows large MCE even at low magnetic fields.

x

In particular, the values of ΔS_m reach 14.7 and 23.8 J kg^{-1}K^{-1} for field changes of 0-1 T and 0-2 T, respectively. The low-field giant MCE, together with the absence of thermal and field hysteresis makes EuTi$_{0.85}$Nb$_{0.15}$O$_3$ a very promising candidate for low temperature magnetic refrigeration.

Large low-field magnetic refrigeration in ferromagnetic insulator EuTi$_{0.9}$V$_{0.1}$O$_3$
Though in ETNO, MC enhances due to the broadening of ΔS_m curve but due to its metallic nature, eddy current loss may reduce the magnetic cooling/heating efficiency significantly. Therefore, our aim is to keep the insulating property of the ground state of ETO unchanged by doping so that eddy current loss can be avoided. As vanadium (V) belongs to the same group of Nb in Periodic Table and their ionic radius are almost equal, Ti can be replaced by V. In this aspect, we doped V at Ti site of ETO and carried out the similar measurements as ETNO. ETVO becomes a FM insulator having T$_C$=4.84 K. The T dependence of zero-
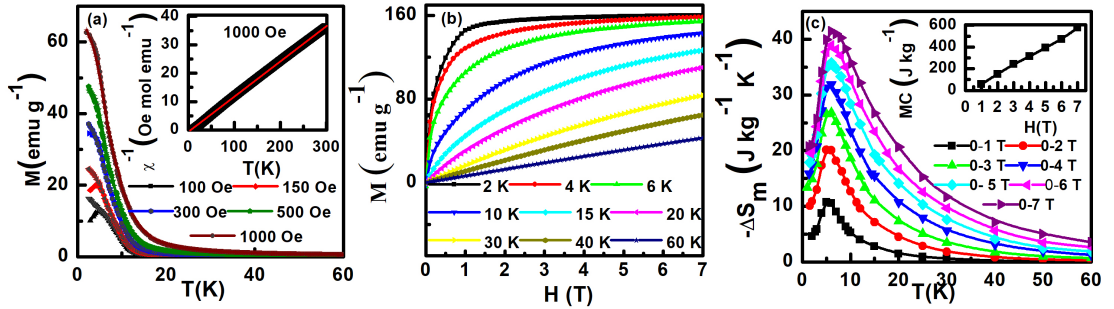
Figure 7: For ETVO (a)T dependence of ZFC and FC magnetization at different magnetic fields between 100 and 1000 Oe. The open symbols indicate FC curves, whereas the solid symbols stand for ZFC curves. The inset shows the χ^{-1} for 1000 Oe.(b) M(H)curves. (c) T dependence of the ΔS_m. Inset shows the H variation of MC.

field-cooled (ZFC) magnetization M$_{ZFC}$ and field-cooled (FC) magnetization M$_{FC}$ measured at various H are shown in Fig. 7(a) for ETVO. In PM state, M$_{ZFC}$ and M$_{FC}$ increase monotonically with decreasing T, and do not split from each other.

On the other hand, the nature of the T dependence of M_{ZFC} and M_{FC} curves is quite different at low H and T, they bifurcate below the peak in the M_{ZFC} curve. This bifurcation is absent in case of ETO and ETNO. With the increase in H, the difference between M_{ZFC} and M_{FC} decreases and disappears at around 500 Oe. The appearance of a peak in the ZFC curve suggests a strong competition between FM and AFM interactions. In the inset of Fig. 7(a), the linear fit to the χ^{-1} of ETVO results the θ_{CW}=5.02 K and $P_{eff} = 8.08\mu_B/$Eu which are larger than the undoped one [21]. The M(H) for ETVO is drawn in Fig. 7(b) for few representative H. Similar to ETNO, in FM state, M increases rapidly with H and then tends to saturate. The nature of M(H) of ETVO is different from that in ETO. M(H) in ETVO mimics like a typical FM whereas in ETO, M(H) is almost linear at low magnetic field below 1.2 T, like an AFM material [21]. All the above features of M(H) and M(T) suggest that the superexchange interaction between the Eu^{2+} moments weakens with V doping at the Ti site in ETO. At 2 K and 7 T, the value of M is found to be 7.1 μ_B per formula unit which is $0.1\mu_B$ larger than the expected spin-only moment of Eu^{2+}, indicating an additional contribution from the 3d shell of the V ion [21]. Indeed, this excess $0.1\mu_B$ exactly coincides with the expected value of M when 10% Ti is replaced by isovalent V which confirms the 4+ valence state of the V ion. The ΔS_m of ETVO is drawn in Fig. 7(c). The inset of Fig. 7(c) shows that MC increases almost linearly with H and reaches as high as 577 J kg^{-1} for a field change of 7 T. This value of MC is larger than that observed in ETO (500 J kg^{-1}) and ETNO (556 J kg^{-1}). The values of ΔS_m for ETVO, ETNO and ETO are large and comparable, but MC for the ETVO is larger. The higher value fo MC makes the insulating ETVO a much more efficient low-temperature magnetic refrigerant and has an added advantage over both ETO and ETNO for

H_2 liquefaction [21].

The ΔS_m, calculated from the C_p data is comparable to that calculated from M(H). The value of ΔT_{ad} is found to be 17.4 K for 0-7 T field change. For practical purposes, apart from the above-mentioned parameters related to MCE, it is a useful guide to select the MCE materials on the basis of energy efficiency where electrical or mechanical work is done to achieve highly reversible caloric effects. We have estimated the electrical and mechanical energy efficiencies for ETVO and other reported high MCE materials to make a comparison among them and found that both electrical and mechanical energy efficiencies of ETVO are larger than that for several low-temperature magnetic refrigerants [21, 22].

References

[1] G. Khaliullin and S. Okamoto, Phys. Rev. Lett. **89**, 167201 (2002).

[2] C. Ulrich *et al.*, Phys. Rev. Lett. **89**, 167202 (2002).

[3] V. Scagnoli *et al.*, Phys. Rev. B **86**, 094432 (2012).

[4] T. Katsufuji and H. Takagi, Phys. Rev. B **64**, 054415 (2001).

[5] J. H. Lee *et al.*, Nature (London) **466**, 954 (2010).

[6] K. S. Takahashi *et al.*, Phys. Rev. Lett. **103**, 057204 (2009).

[7] T. Katsufuji and Y. Tokura, Phys. Rev. B **60**, R15021 (1999).

[8] A. Oleaga *et al.*, J. Phys.: Condens.Matter **17**, 6729 (2005).

[9] J. A. Souza *et al.*, Phys. Rev. B **81**, 172410 (2010).

[10] Y. Kususe *et al.*, Jpn. J. Appl. Phys. **53**, 05FJ07 (2014).

[11] L. Li *et al.*, APL Mater. **2**, 110701 (2014).

[12] L. Li *et al.*, Phys. Rev. B **92**, 024109 (2015).

[13] C. Kittel, Introduction to Solid State Physics (Wiley, New York, 2005).

[14] L. Klein *et al.*, Phys. Rev. Lett. **77**, 2774 (1996).

[15] F. Rivadulla *et al.*, Phys. Rev. B **67**, 165110 (2003).

[16] M. Nicklas *et al.*, Phys. Rev. Lett. **82**, 4268 (1999).

[17] K. Ueda and T. Moriya, J. Phys. Soc. Jpn. **39**, 605 (1975).

[18] S. N. Kaul, J. Phys.: Condens. Matter **17**, 5595 (2005).

[19] C. Krellner *et al.*, Phys. Rev. B **76**, 104418 (2007).

[20] N. Takeda and M. Ishikawa, J. Phys.: Condens.Matter **15**, L229 (2003).

[21] A. Midya *et al.*, Phys. Rev. B **93**, 094422 (2016).

[22] T. Samanta, I. Das, and S. Banerjee, Appl. Phys. Lett. **91**, 152506 (2007).

List of Figures

List of Tables

<div style="text-align: right; font-size: 4em; color: gray;">**1**</div>

Introduction

1.1 Perovskite oxides

Oxides are most abundant in earth. They are famous for their potential technological applications in various areas of modern life. In 1839, German mineralogist Gustav Rose discovered the mineral $CaTiO_3$ and named it as "Perovskite" after a Russian Military official, L. A. Perovsky [1]. Later on, the term "Perovskite" is applicable for compounds possessing similar crystal structure and stoichiometry with a general formula "ABO_3".

In ABO_3, A can be occupied by either alkaline-earth elements (Na^+, K^+, Sr^{2+}, Ba^{2+}, Ca^{2+}, etc.) or rare-earth elements (La^{3+}, Gd^{3+}, etc.) and B site can be any of Nb^{5+}, Ti^{4+}, Co^{3+}, Mn^{3+}, Fe^{3+}, etc. The simplest form of a perovskite structure is shown in Fig. 1.1 as a cubic unit cell at which the smaller ion B is situated at the center of the cube (i.e., at body-centered position), the larger ion A will occupy each corner of the cube and O^{2-} ions will be placed at the face-centered position of each surface of the cube. The stability of the perovskite crystal structure is
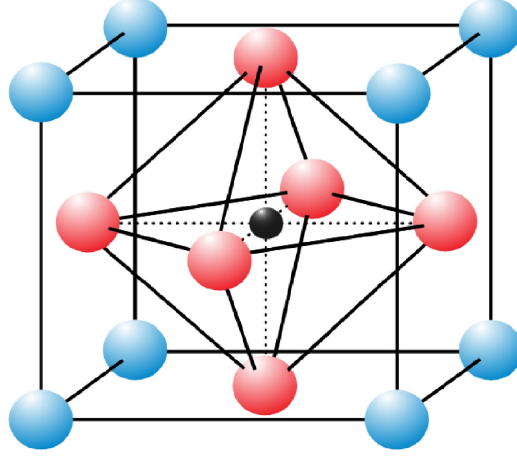
Figure 1.1: A schematic of crystal structure of perovskite oxide ABO_3. A site: blue cations, B site: black cation and O site: pink anions. Reproduced from Ref. [2].

defined by Goldschmidt's tolerance factor [3],

$$t = \frac{(r_A + r_O)}{\sqrt{2}(r_B + r_O)};\qquad(1.1)$$

where r_A, r_B and r_O are the radii of A cation, B cation and O anion, respectively. The structure is stable for $0.89 \leq t \leq 1.06$. Any foreign atom can be doped at A or B site but the degree of substitution is not liberal as the introduction of foreign atom may distort the crystal structure and this distortion is restricted by the above mentioned tolerance factor. Depending on the combinations of A and B site cations, perovskites exhibit different interesting properties such as superconductivity, colossal magnetoresistance, ferroelectric or piezoelectric properties, etc.

1.1.1 Rare-earth oxides

Rare-earth titanates are one of the most interesting topics because of their interplay between the electronic, structural and magnetic properties. They exhibit a variety of strongly correlated phenomena such as insulator to metal transition, magnetoresistance, magnetocaloric, magneto-structural effect, etc. [4, 5, 6]. In $RTiO_3$, R is rare-earth element (R: La, Pr, Gd, etc.). Both of R and Ti ions are in trivalent state except in $EuTiO_3$. In these compounds, Ti^{3+} has t_{2g}^1 configuration in which threefold degenerate t_{2g} orbitals are occupied by only one electron.

1.1.2 Crystal Field Theory (CFT)

It has been assumed in CFT that ligands are negative point charges and the interation between ligands and the metal ion is purely electrostatic in nature. In case of an isolated metal ion, all the five d orbitals are of same energy. But the situation is completely different when the metal ion is kept inside a crystal lattice, they are bounded by ligands and a repulsive force comes into play between the d-electrons and ligand electrons. Due to different symmetries of d orbitals and inductive effect of ligands on electrons, the orbital degeneracy can be removed and d orbitals split apart. This splitting depends on the nature of crystal field. In case of spherical symmetry of crystal field, the d orbitals remain as degenerate but due to repulsion between like charges, the energy of orbitals will raise. In real cases, if the orbital has lower symmetry instead of spherical symmetry, then the d orbitals will split and become non-degenerate. For octahedral symmetry, the metal ion is surrounded by six ligands. Now, we will see how the energies of d orbitals of a

transition metal ion will be affected by an octahedral arrangement of six negative point charges. Ligands are connected to metal ion along x, y, z axes. Therefore, the ligand electrons in d_{z^2} and $d_{x^2-y^2}$ orbitals (lie along x, y, z axes) feel stronger repulsion. It requires more energy to place an electron in these two d orbitals. On the other hand, the other three orbitals d_{xy}, d_{yz}, d_{zx}, oriented at $45°$ angle to x, y, z axes, will feel weaker repulsion. Thus, the difference in repulsive energies in octahedral structure yields two groups of energy levels t_{2g} : set of three orbitals d_{xy}, d_{yz}, d_{zx} with lower energy and e_g : set of two orbitals d_{z^2}, $d_{x^2-y^2}$ with higher energy. The angular dependence of $3d$ orbitals is shown in Fig. 1.2.
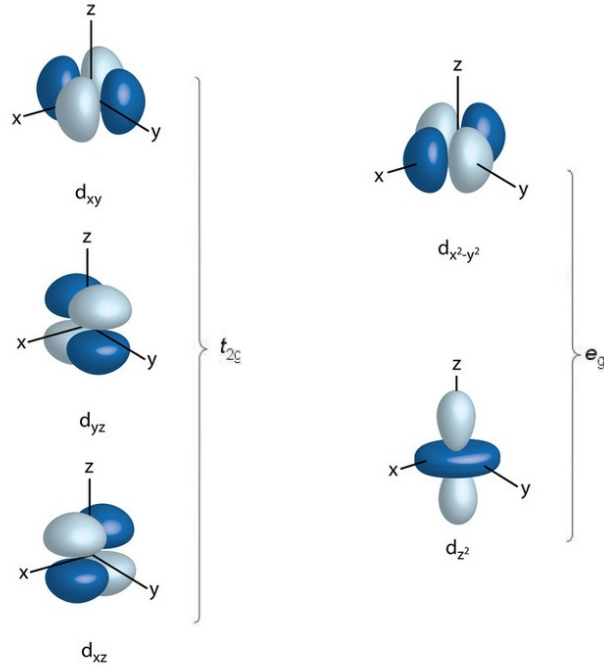
Figure 1.2: Orientation of $3d$ orbitals with respect to an octahedral array of charged ligands. Reproduced from Ref. [7].

This splitting in presence of ligands is called crystal field splitting. According to Hund's rule, each of first three electrons will occupy three of t_{2g} orbitals.

Then, the fourth electron will go either into one of the t_{2g} orbitals or e_g orbitals. It depends on the difference between spin-pairing energy (Δ_P) and crystal field splitting energy (Δ_{cf}). When $\Delta_{cf} > \Delta_P$, the fourth electron will occupy t_{2g} level which leads to a low-spin (LS) state. In contrast, if $\Delta_{cf} < \Delta_P$, the electron will go into e_g state which leads to high-spin (HS) state.

The crystal field effect in lanthanides is also discussed here [8]. Due to having strongly localized $4f$ orbitals, they are less likely to make bonds. Unlike d orbitals, f orbitals split into two triply degenerate states ($f_{x(z^2-y^2)}$, $f_{z(x^2-y^2)}$, and $f_{y(z^2-x^2)}$); (f_x^3, f_y^3, and f_z^3) and one non degenerate state (f_{xyz}) in octahedral environment. The difference with $3d$ orbitals is that the bonding energies and metal-ligand interactions are very weak. In case of $RTiO_3$, the $3d$ transition metal ion Ti^{3+} has one electron which occupies one of three t_{2g} orbitals. The crystal stabilization energy for one electron in Ti^{3+} is, $\Delta_{csf} = 2/5\ \Delta_O$, where Δ_O is the energy separation between e_g and t_{2g} levels [9]. In $EuTiO_3$, Ti is at 4+ state which contains no electron in d orbital and $4f^7$ orbital of Eu^{2+} is isotropic ($L=0$). Therefore, crystal field splitting is zero in ETO. However, there is an emerging evidence that this might not always be the case with reduced spin isotropy reported at low temperature in $Gd_3Ga_5O_{12}$ (GGG) [10].

1.1.3 Jahn-Teller effect (JT)

Jahn-Teller theorem says that an orbitally degenerate ground state of a non-linear molecule or ion undergoes a spontaneous geometrical distortion to achieve a lower energy configuration by removing the degeneracy [11]. To achieve the lower symmetry, the bonds along z axis get shortened (z-in distortion) or elongated (z-out

distortion). This elongation or compression depends on the overlap between metal ion and ligands. The more the overlap the greater is the strength of JT effect. One of the possible modes of JT effect is shown in Fig. 1.3.
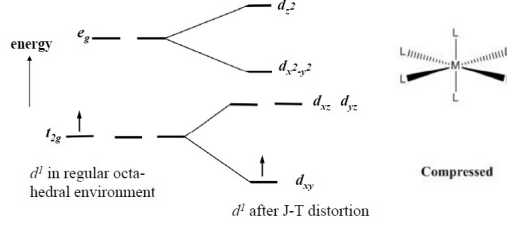
Figure 1.3: Jahn-Teller Distortion in d^1 Complexes. Reproduced from Ref [12].

In $3d^1$ configuration of Ti^{3+} in $RTiO_3$, it has an octahedral surrounding. This d^1 configuration is electronically degenerate. The electron can occupy any of three t_{2g} degenerate orbitals. The JT effect in d^1 configuration is less effective as there is less overlapping between t_{2g} orbitals and metal ion. In $EuTiO_3$, no Jahn-Teller distortion takes place as there is no electron in $3d$ orbital.

1.2   Magnetism: Exchange mechanisms

The basic characteristics of an electron is that it has a magnetic dipole moment. It behaves like a tiny magnet. This dipole moment is associated to the electronic spin. Due to the quantum mechanical nature of an electron, the spin can be up or down with the application of external magnetic field. Mainly, the spin participates in magnetism although orbital angular momentum of electron also contributes. The material with a partially filled orbital has a net magnetic moment. These unpaired

magnetic dipoles (simply the spins) tend to align in the same direction of the magnetic field, is called paramagnetism. On the other hand, if the dipoles tend to align spontaneously without any field, then the magnetism is called ferromagnetism. Oppositely aligned dipoles without any magnetic field cause antiferromagnetism. Ferromagnetism or antiferromagnetism involves an additional phenomenon.

According to classical electromagnetism, two nearby magnetic dipoles will tend to align themselves in opposite directions. However, this dipole-dipole interaction is weaker as the fields generated by individual spins are small in magnitude and also easily get destroyed due to thermal fluctuations. There is a kind of materials in which a much stronger interaction between spins exists by changing the direction of spins which leads to a change in electrostatic repulsion between neighboring electrons. This stronger interaction is caused by a quantum mechanical effect which is termed as exchange interaction. At short distances, the exchange interaction is much stronger than the dipole-dipole interaction. The exchange interaction is basically based on Pauli's exclusion principle, i.e., two electrons having the same spin cannot occupy the same position in space. Whether it is a ferromagnet or an antiferromagnet, this exchange interaction between magnetic ions will force to align the individual moments in parallel (ferro) or antiparallel (antiferro) with their neighbors. There exist three types of exchanges (i) direct exchange, (ii) indirect exchange and (iii) superexchange.

1.2.1 Dipole-dipole interaction

Two magnetic dipoles with moments $\boldsymbol{\mu_1}$ and $\boldsymbol{\mu_2}$ are separated by a distance $\mathbf{r}$. The interacting energy between these two dipoles is given by:

$$E = \frac{\mu_0}{4\pi r^3}\left[\boldsymbol{\mu_1}\cdot\boldsymbol{\mu_2} - \frac{3}{r^2}(\boldsymbol{\mu_1}\cdot\mathbf{r})(\boldsymbol{\mu_2}\cdot\mathbf{r})\right], \tag{1.2}$$

This only holds for short range. If $\mathbf{r}$ is large, the interaction between dipoles will die out. The long range contribution of dipole-dipole interaction is often neglected except in some materials where it is large, such as in lanthanides. In transition metals, as an example the exchange energy is about 1000 times stronger than the dipolar energy in iron (Fe) [13]. In contrast, in pyrochlores $Ln_2Ti_2O_7$ (Ln=Dy, Tb, Ho, etc.), the value of dipolar interaction is almost comparable to the exchange energy due to having highly localised $4f$ orbitals. As an example, the magnitudes of dipolar energy and exchange energy are respectively 2.35 K and 1.24 K in $Dy_2Ti_2O_7$ [14].

1.2.2 Direct exchange

This type of exchange is a short-range coupling. It acts between two closely spaced atoms which have an overlap between their corresponding wave functions. Let us consider, two atoms having one electron in each, are very close to each other. According to Bethe and Slater, in case of small interatomic distance between two neighboring atoms, the Coulomb interaction is minimal and, therefore, electrons spend most of their time in between the nuclei. As two electrons have to spend the same position at the same time, according to Pauli's exclusion principle, it is required to have opposite spin alignment. This gives an antiparallel arrangement

of spins which causes antiferromagnetism (negative exchange). Similarly, when two atoms are far away from each other they have very less time to spend at the same position at the same time. This gives a parallel arrangement of spins which causes ferromagnetism (positive exchange). A schematic of direct exchange interaction is displayed in Fig. 1.4.
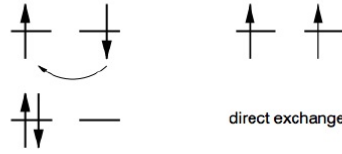
Figure 1.4: A schematic diagram of direct exchange interaction. Reproduced from Ref. [1].

The spin-dependent term in the effective Hamiltonian of a simple model of two electrons with spins $\mathbf{S}_1$ and $\mathbf{S}_2$ can be written as

$$H_{spin} = -2J \, \mathbf{S}_1 \cdot \mathbf{S}_2 \, , \tag{1.3}$$

where, J is called exchange constant or exchange integral. $J > 0$ gives the minimum of energy for the parallel spin alignment, i.e., triplet state with S_{total}=1, whereas, $J < 0$ gives the minimum of energy for the antiparallel spin alignment or singlet state with S_{total}=0.

The Bethe-Slater curve represents the magnitude of direct exchange as a function of interatomic distance [15]. Cobalt is located near the peak of this curve at the positive exchange side whereas manganese and chromium are on the negative exchange side of this curve. On the other hand, iron is situated just beside the

zero-crossing point. For example, in rare earths, the 4f electrons are strongly lo-calised and lie very close to the nucleus. So, it is very unlikely to overlap between atomic orbitals, hence direct exchange is rare in rare earths. For $3d$ transition metal elements (Fe, Co, Ni, etc.), the $3d$ orbitals extend away from the nucleus and one needs to go beyond direct exchange. However, in $A_2Cr_2O_4$ spinels with smaller ionic radii, for examples in $A=$ Zn, Mg, direct exchange has a significant contribution. But with increasing ionic radius of A ion, the direct exchange de-creases as the distance between Cr ions increases [16].

1.2.3 Indirect or Ruderman-Kittel-Kasuya-Yoshida (RKKY) exchange

Indirect exchange is the interaction between two atoms which are separated by a large distance. This interaction does not require a direct coupling between the moments. There will be no direct overlapping between their wave functions. It, therefore, acts between two largely placed atoms via an intermediatory atom. In metal, it is the dominant exchange interaction as there is tiny or no direct overlap between neighboring electrons. For metals, the intermediatory is the conduction electrons (itinerant electrons). This type of exchange is better known as the RKKY interaction named after Ruderman, Kittel, Kasuya and Yoshida. The RKKY ex-change coefficient J oscillates in a damping manner from positive to negative with the variation of the separation between ions. Therefore, their magnetic ordering can either be ferromagnetic or antiferromagnetic depending on the separation be-tween a pair of ions. A magnetic ion induces a spin polarization in the conduction electrons in its neighborhood. This spin polarization in the conduction electrons

is then felt by the moments of other magnetic ions within the range leading to an indirect coupling. In rare-earth metals, whose magnetic electrons in the $4f$ shell are shielded by the $5s$ and $5p$ electrons, indirect exchange via the conduction electrons gives rise to magnetic order in these materials.

1.2.4 Superexchange

It is a coupling between two atoms far apart from each other, via a non-magnetic intermediatory atom. Superexchange interacts between the electrons having come from the same donor atom and being coupled with the receiving ion's spins. If the two next-to-nearest neighbor positive ions are connected at $180°$ via the bridging non-magnetic anion, then the interaction is antiferromagnetic whereas for $90°$ alignment, it leads to the ferromagnetic coupling. Therefore in superexchange, a ferromagnetic or an antiferromagnetic alignment occurs between two atoms with the same valence. Thus, the sign and strength of this indirect exchange interaction depend on the orbital structure of the involved ions and occupancy of the orbitals of magnetic ion and their overlaps with the mediating ligand orbitals. As an example, the superexchange interaction has been discussed for antiferromagnetic $La^{3+}Mn^{3+}O_3^{2-}$ in Fig. 1.5. In LaMnO$_3$, three $2p_x$, $2p_y$, and $2p_z$ orbitals of O^{2-} are completely filled, whereas the five $3d$ orbitals of the Mn^{3+} ion are filled up with four electrons of which three electrons occupy the three t_{2g} orbitals and the fourth one is in one of the e_g orbitals. There is a direct overlap between the e_g orbitals of Mn^{3+} and the O-$2p$ orbitals. The virtual hopping of O-$2p$ electrons into the Mn-e_g orbitals leads to a virtual excited state which favors the decrease in the total energy of the system depending on the spin alignments. Here, the Pauli's exclusion

principle supports two electrons to be located in the same e_g orbital having opposite spin alignments, whereas, Hund's rule favors electrons having the same spin alignments will be in two different orbitals e_g and t_{2g}. Two types of superexchange interactions are illustrated on the basis of the Goodenough-Kanamori-Anderson (GKA) rule [17].
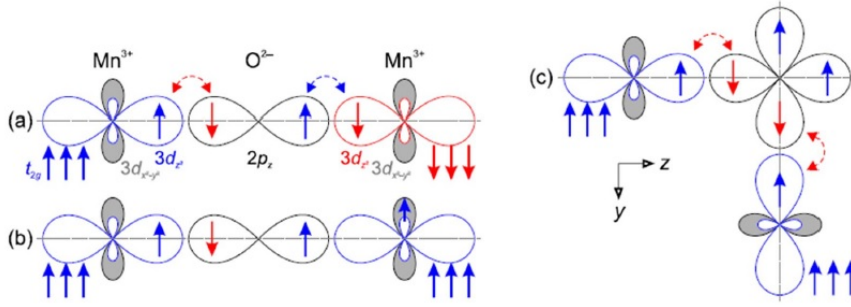
Figure 1.5: Superexchange interaction between the $3d_{z^2}$ orbital of two Mn^{3+} ions via the $2p_z$ orbital of an O^{2-} ion. The $3d_{x^2-y^2}$ orbital of Mn^{3+} is shaded in grey. The core spin of the three t_{2g} orbitals of Mn^{3+} is represented by triple arrows. Depending on the occupation of electrons, the resulting interaction can be (a) antiferromagnetic or (b), (c) ferromagnetic. Reproduced from Ref. [18].

(a) For two Mn^{3+} ions along the z direction with one electron each in their respective Mn-$3d_{z^2}$ orbitals, virtual hopping of the two O-$2p_z$ electrons will reduce the total energy of the system, if the Mn core spins are aligned antiparallel. This $180°$ exchange between two half-filled or two empty orbitals mediated by single ligand orbital is strong and antiferromagnetic.

(b) For two Mn^{3+} ions along the z direction where the first has one electron and the second has no electron in their respective Mn-$3d_{z^2}$ orbitals, virtual hopping of the two O-$2p_z$ electrons will reduce the total energy of the system, if the Mn core spins are aligned parallel. This $180°$ exchange between one half-filled and one

empty orbitals mediated by single ligand orbital is weak and ferromagnetic.

(c) For two Mn^{3+} ions with one electron in their corresponding Mn-$3d_{z^2}$ orbitals corner sharing the same O^{2-} ion, virtual hopping of one O-$2p_z$ and one O-$2p_y$ electron will reduce the total energy of the system if the Mn core spins are parallel. The reason behind this scenario is the Hund's coupling of the two remaining O-$2p$ spins at the O site. This 90° exchange between two half-filled orbitals mediated by two ligand orbitals is weak and ferromagnetic.

1.2.5   Double exchange

This is also another type of coupling between atoms at large distance. Unlike superexchange, this interaction acts between two ions with different oxidation states. In this exchange, a hopping process is involved in addition to Coulomb interaction. Suppose, we have one Mn^{3+} and one Mn^{4+}, bridged by an O^{2-} ion through an angle of 180° in which the Mn "e_g" orbitals are directly interacting with the O "$2p$" orbitals, and one of the Mn ions has more electrons than the other. The e_g electron in the $3d_{z^2}$ orbital of Mn^{3+} can hop via the O-$2p_z$ orbital to the $3d_{z^2}$ orbital of Mn^{4+} without the need to pay for the Coulomb repulsion energy. However, there is a strong on-site (Hund's rule) exchange interaction between the e_g electron and the localized core electrons in the t_{2g} level which keeps them all aligned. If the core spins of the respective Mn ions are aligned parallel, Hund's coupling energy J_H vanishes favoring electronic hopping transport across the oxygen ion. Vice-versa, an antiparallel orientation of the core spin would lead to $J_H > 0$ and, therefore, it is not energetically favorable for an e_g electron to hop to a neighboring ion in which the t_{2g} spins will be antiparallel to the e_g electron. Ferromagnetic alignment

of neighboring ions is, therefore, required to maintain the high-spin arrangement on both the donor and acceptor ions. Because the ability to hop gives a kinetic energy saving, the hopping process shown in Fig. 1.6. reduces the overall energy. Thus, the system ferromagnetically aligns to save energy.
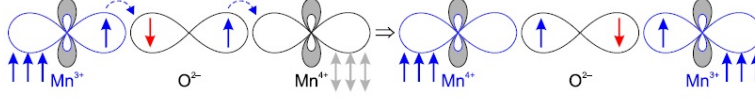
Figure 1.6: Double exchange interaction between the $3d_{z^2}$ orbital of a Mn^{3+} and a Mn^{4+} ion via the $2p_z$ orbital of an O^{2-} ion. The $3d_{x^2-y^2}$ orbital of Mn is shaded in grey. The core spin of the three (not-shown) t_{2g} orbitals of Mn is represented by triple arrows. The resulting interaction is ferromagnetic, mediated by the itinerant electron of Mn^{3+}. Reproduced from Ref. [18].

1.3   Elementary excitations in magnetic material

Exchange interaction not only plays an important role in describing magnetic ordering but is also responsible for collective excitations in spin systems. This collective excitations are low-energy excited states just above the ground state. The ground state is therefore important to define. The ground state of a ferromagnet is that all the spins are aligned along the same direction. In case of an antiferromagnet, spins are oppositely aligned. The simplest excited state can be imagined by those in which a single spin is deviated slightly. This slight deviation consequently reduces the magnetic moment. This deviation is not static but it propagates through all the ions in the crystal. Thus it will form a collective excitation. This type of collective excitation is called as spin waves.
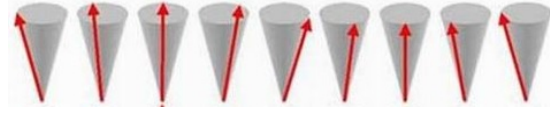
Figure 1.7: A pictorial representation of spin wave. Reproduced from Ref. [19].

Consider a ferromagnet which is perfectly ordered at $T = 0$ K. But as T increases, i.e., $T > 0$ K, its order gets interrupted by spin waves. The energy of spin wave is very low and it is quantized in units of $\hbar\omega(q)$ where $\omega(q)$ is the frequency of spin wave mode with wave vector q. The quanta of spin wave is magnon which is similar to the quanta of lattice waves, i.e., phonon. The low-energy spin wave has long wavelength. The Hamiltonian of a ferromagnetic system is

$$H = -2J\sum_{i,j} \boldsymbol{S}_i.\boldsymbol{S}_j, \tag{1.4}$$

where $\boldsymbol{S}_i$, $\boldsymbol{S}_j$ are the relative spin vectors of the ith and jth site respectively. $J=$ exchange integral. The sum is over all pairs of lattice ions. In case of one-dimensional chain, each spin has two neighbors and the above equation will be in the following form,

$$H = -2J\sum_{i,j} \boldsymbol{S}_i.\boldsymbol{S}_{i+1}, \tag{1.5}$$

We will now go for the classical derivation of magnon dispersion relation. Hamiltonian of the ith spin, by only considering the interactions between the nearest neighbors, is

$$H = -2J\boldsymbol{S}_i.(\boldsymbol{S_{i-1}} + \boldsymbol{S_{i+1}}), \tag{1.6}$$

where $\boldsymbol{S}_{i-1}$, $\boldsymbol{S}_i$, $\boldsymbol{S}_{i+1}$ are the spin vectors of the ith, $(i-1)$th, $(i+1)$th sites

respectively. The magnetic moment at the ith site is

$$\boldsymbol{\mu}_i = -g\mu_B \boldsymbol{S}_i, \tag{1.7}$$

Therefore, $\boldsymbol{S}_i = \frac{-\boldsymbol{\mu}_i}{g\mu_B}$.

$$H = -2J\frac{-\boldsymbol{\mu}_i}{g\mu_B}.(\boldsymbol{S_{i-1}} + \boldsymbol{S_{i+1}}) = -\boldsymbol{\mu}_i.\boldsymbol{B}_i, \tag{1.8}$$

$\boldsymbol{B}_i$ is the effective exchange field acting on the ith site.

$$\boldsymbol{B}_i = \frac{2J}{g\mu_B}.(\boldsymbol{S_{i-1}} + \boldsymbol{S_{i+1}}), \tag{1.9}$$

According to classical mechanics, the rate of change of angular momentum will give the torque acting on the ith site.

$$\frac{d}{dt}(\hbar\boldsymbol{S}_i) = \boldsymbol{\mu}_i \times \boldsymbol{B}_i, \tag{1.10}$$

By putting the value of $\boldsymbol{\mu}_i$ & $\boldsymbol{B}_i$ in terms of $\boldsymbol{S}_i$, we get

$$\frac{d\boldsymbol{S}_i}{dt} = -2J(\boldsymbol{S}_i \times \boldsymbol{S}_{i-1} + \boldsymbol{S}_i \times \boldsymbol{S}_{i+1}), \tag{1.11}$$

By assuming that the excitation is small, i.e., $(S_i^x, S_i^y \ll S)$ and $S_i^z = S$, the components of the above in X, Y, Z are

$$\frac{dS_i^x}{dt} = (\frac{2JS}{\hbar})[2S_i^y - S_{i-1}^y - S_{i+1}^y] \tag{1.12}$$

$$\frac{dS_i^y}{dt} = (\frac{2JS}{\hbar})[2S_i^x - S_{i-1}^x - S_{i+1}^x] \tag{1.13}$$

$$\frac{dS_i^z}{dt} = 0 \tag{1.14}$$

By considering the wave solutions as $S_i^x = Ae^{i(q_ia-\omega t)}$ and $S_i^y = Be^{i(q_ia-\omega t)}$, where $\boldsymbol{q}$ is the wave vector, we have obtained the dispersion relation for spin wave

$$\hbar\omega = 4JS(1 - \cos qa) \tag{1.15}$$

For small $\boldsymbol{q}$, q$\ll$1, $\omega \propto q^2$. The density of states in three-dimensional system is g(q)dq $\propto q^2 dq$. The number of excited magnons at temperature T is estimated by integrating the density of states of magnons multiplied by Bose distribution function $(e^{\hbar\omega/k_BT}$-1$)^{-1}$, over all frequencies. Therefore,

$$n_{magnon} = \int_0^\infty \frac{g(\omega)d\omega}{(e^{\hbar\omega/k_BT} - 1)}, \tag{1.16}$$

In 3D, $g(\omega) \propto \omega^{1/2}$, which gives $n_{magnon} \propto T^{3/2}$. Since each thermally excited magnon mode reduces the total magnetization by $S = 1$, therefore, at low temperature the reduction in spontaneous magnetization from the value at $T = 0$ K is given by

$$\frac{\Delta M}{M(0)} \propto T^{3/2}. \tag{1.17}$$

This is called Bloch's law [20].

1.4 Strongly correlated electronic systems

Conventional band theory successfully explains the distinction between metal and insulator. Electron-electron interaction is completely ignored in this theory. In non-interacting electron theory, the formation of a band structure is entirely due to the periodic lattice structure of atoms in solids. Although band theory explains

many materials but de Boer and Verwey reported in 1937 that there are few transition metal oxides which cannot be explained by conventional band theory [21]. This type of materials with partially filled d bands is not a metal but indeed an insulator. In this regard, Peierls (1937) pointed out the importance of electron-electron correlation, Coulomb repulsion between electrons could be the origin of insulating behavior [21]. Materials with strong electronic correlations are those in which the movement of one single electron will affect on the other electrons in the system. Materials with incompletely filled d or f orbitals are the strongly correlated materials.

1.4.1 Fermi-liquid theory

The physical properties of a metal such as heat capacity, magnetic susceptibility, etc. were well explained by Pauli and Sommerfeld with an assumption that a metal is a gas of non-interacting electrons. But the puzzle was why a non-interacting theory holds so well in the systems where interaction is an important issue. In 1956, L. Landau proposed a phenomenological theory for interacting system of fermions (S=1/2) which is known as "Landau's Fermi-liquid theory" [22]. The key idea of this theory is the application of adiabatic continuity and Pauli's exclusion principle. Starting with the ground state of a non-interacting fermionic system (Fermi gas), if we slowly turn on the interaction, finally we will get the ground state of a Fermi-liquid. He postulated that there will be an one-to-one correspondence of the low-lying excited state of Fermi gas to the ground state of a Fermi-liquid. He supposed that the good quantum numbers such as total number of particles, spin, momentum, etc. will remain conserved even after the interactions are applied. But the energy is not preserved as the Hamiltonian is changed. Now, the electrons

become "dressed" by its interaction with other electrons. The "dressed" electrons are named as "quasi-particles" whose wave function and energy are different from that of the corresponding electrons in non-interacting case. In Landau's theory, (i) he modified the inertial mass of the quasi-particle, i.e., $m = m^*$, (ii) The energy of a single quasi-particle also depends on the distribution of other quasi-particles via the function "F".

The basic properties become [22]

$$C_v = \frac{m^* P_F k_B^2 T}{3\hbar^3}, \tag{1.18}$$

$$\chi = \frac{m^* P_F \mu_B^2}{\pi^2 \hbar (1 + F)}, \tag{1.19}$$

Therefore, it is clear from the above mentioned equations that the expressions are similar to that of Fermi gas except the modified mass m^* and F in χ.

In Fermi liquid, the quasi-particles are the cloud of electron-hole pairs. These quasi-particles require an intrinsic decay time to disperse their energy throughout the electron-hole sea. Suppose, we have a Fermi surface in $\boldsymbol{K}$-space with a crystal momentum $\hbar K_F$. Now, if we excite one quasi-particle to an energy ϵ above the Fermi surface and would like to estimate the decay time for losing this energy. This losing of energy is caused due to the scattering with other quasi-particles. Let us say, ω amount of energy gets transferred into other quasi-particle by our test particle after scattering. Since, the test particle is above the Fermi surface, the energy of the scatterer ϕ must be ω below Fermi energy. Each value of ω gives $O(\omega)$ number of scattering processes. Since, $0 < \omega < \epsilon$ and $0 < \phi < \omega$, therefore, $O(\epsilon^2)$

is the number of possible decaying processes. The decay cross-section is proportional to the number of decays $\propto \epsilon^2$.

$\tau =$ lifetime of the quasi-particles $\simeq \frac{1}{decay cross-section} \propto \frac{1}{\epsilon^2}$.

If the temperature is less than the Fermi temperature T_F, the quasi-particles will be excited at an average energy $\epsilon = k_B T$ above Fermi surface, then, $\tau \propto \frac{1}{T^2}$. This gives electrical conductivity $\sigma \propto \frac{1}{T^2}$. Therefore the resistivity in Fermi-liquid is proportional to T^2 [23, 24].

Summary of Fermi-liquid: (i) Properties of Fermi liquid remain same as the non-interacting case but with modified parameters. (ii) The low excited eigenstates are the quasi-particles with scattering rate$\sim 1/\tau^2 \propto \epsilon^2$.

1.4.2 Non-Fermi-liquid theory

Among complex metals, such as, ruthenates, high-T_C cuprate superconductors, f-electron based alloys, many of these do not follow Landau's Fermi-liquid theory. The low-energy behavior of these materials does not fit with quasi-particle excitation. Non-Fermi-liquids (NFL) are the metals whose physical properties deviate from those of non-interacting system due to strong fluctuations near Fermi surface. Therefore, to describe the physics behind NFL, Landau's theory is replaced by interacting field theories. Understanding the origin of breakdown of Fermi theory is an outstanding challenge in strongly correlated system. The NFL behavior is characterized by weak power law or logarithmic divergence in temperature dependence of physical properties at low temperature which have the following form [25]:

$$\rho(T) \sim \rho_0[1 - a(\frac{T}{T_0})^n],\qquad(1.20)$$

$$\frac{C_v(T)}{T} \sim -(\frac{bR}{T_0}) \ln(\frac{b'T}{T_0}), \tag{1.21}$$

$$\chi(T) \simeq \chi_0 [1 - c(\frac{T}{T_0})^{1/2}], \tag{1.22}$$

where a, b, b', c are the constants. a can be positive or negative. n lies in the range of $1 \leqslant n \leqslant 1.6$.

1.4.3   Kondo effect

Electrical resistivity of a pure metal goes to zero at low temperature $T \longrightarrow 0$ K, when the lattice vibration is very less effective. However, a saturation in resistivity curve occurs at low T due to the static defects in material. This resistivity saturation changes to a minimum in resistivity curve when the impurity is a magnetic entity. Kondo effect mainly arises due to the interaction of conduction electrons with the magnetic impurity in a metal [26]. When a conduction electron passes through a metal, it gets scattered from the impurity and both exchange their spin alignments. The magnetic ion changes its spin direction opposite to the spin direction of the conduction electron by following Pauli's exclusion principle. In case of a single magnetic impurity inside a metal, Kondo effect takes place and at low temperature spin flipping of both the conduction electron and impurity atom leads to form a singlet state (antiferromagnetic coupling). A logarithmic increase in resistivity with decreasing temperature is an indication of Kondo effect. At high temperature, the impurity scatters the conduction electrons, whereas with lowering temperature, the effective interaction between them grows and eventually a singlet bound state is formed as an inert scatterer. The other electrons which

do not participate in the formation of singlet state, will feel a potential screening rather than spin scattering. It seems like the impurity spin is effectively screened from the system. The Kondo temperature T_K is given by $T_K \sim D_W e^{-1/(2J\eta)}$, where D_W is the conduction bandwidth, J is the exchange coupling and η is the density of states of the conduction sea [27].
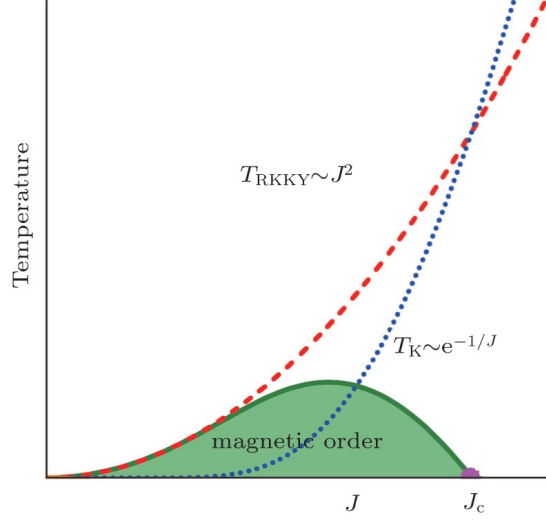
Figure 1.8: A schematic illustration of Doniach's phase diagram. Reproduced from Ref. [28].

When a system contains several localized impurity magnetic moments in a metal, there exist both magnetic ordering and Kondo non-magnetic state simultaneously. The localised spins order themselves in a ferromagnetic manner due to RKKY exchange interaction via intermediatory conduction electrons, $T_{RKKY} \propto J^2\eta$ [27]. At high temperature conduction electron and localized moments weakly interact but at low temperature RKKY interaction is larger than Kondo-singlet formation. The competition between the magnetic ordering and non-magnetic state was first considered by Doniach. Doniach's phase diagram is shown in Fig. 1.8. which has three regimes: Kondo-ferromagnetic region, non-magnetic Kondo state,

pure ferromagnetic state. This diagram shows the result of Kondo temperature in terms of J coupling constant. For small value of J, RKKY is dominant and the system is magnetically ordered. At the intermediate value of J, RKKY and Kondo are energetically comparable, magnetic order still occurs but with partially screened localized moments. With further increase of J, magnetic ordering is suppressed.

1.5 Electronic transport in a ferromagnetic metal

1.5.1 Boltzman transport equation

When an electron passes through a crystal then there exist several disturbances in addition to the periodic potential of atoms. If an electron gets accelerated by an external field then the steady state can be attained via different scattering mechanisms. A steady state means that a change in electron charge distribution caused by external field and/or temperature gradient is balanced with that of the scattering processes. The net change in electronic charge distribution function f is

$$\frac{df}{dt} = (\frac{df}{dt})_{diffusion} + (\frac{df}{dt})_{field} + (\frac{df}{dt})_{scattering}, \qquad (1.23)$$

In steady state, $\frac{df}{dt} = 0$. The different types of scattering mechanisms take place inside a metal [29]. The electrical resistivity is the sum of those contributions in resistivity which are mentioned in the following:

$$\rho = \rho_0 + \rho_{e-ph} + \rho_{e-m} + \rho_{e-e} \qquad (1.24)$$

1.5.2 Impurity scattering

There are static disturbances like impurity atoms, grain boundaries, vacancies, dislocations, etc. inside a crystal. The scattering of conduction electrons with these static defects contributes a temperature independent term ρ_0 in resistivity of a metal. This is sometimes called as residual resistivity.

1.5.3 Electron-phonon scattering

The interaction of the conduction electrons with lattice vibrations is called electron-phonon interaction. At T=0 K, this interaction is zero when lattice vibration ceases. As temperature increases, the lattice vibration enhances. The theoretical equation expressing the temperature variation of electrical resistivity to estimate the contribution from electron-phonon interaction ($\rho_{el-ph}(T)$) is known as Bloch Grüneisen law (BG function). The BG function is as follows,

$$\rho_{el-ph}(T) = \rho^{'} (\frac{T}{\theta_D})^5 \int_0^{\frac{\theta_D}{T}} \frac{x^5 e^x}{(e^x - 1)^2} dx, \tag{1.25}$$

where θ_D is the Debye temperature, $\rho^{'}$ is the coefficient for the electron-phonon contribution of resistivity. Eq. (1.25) gives T^5 dependence of resistivity at low temperature $T \ll \theta_D$ where θ_D is the Debye temperature. At high temperature BG function contributes a linear dependence of T in resistivity.

1.5.4 Electron-magnon scattering

At absolute zero temperature, a ferromagnetic material is perfectly ordered. At a finite temperature the magnetic moments start to deviate at a small angle. This ex-

citation is termed as spin-waves or magnons as discussed previously. Magnons get excited at finite temperature in addition to phonons. Therefore, in ferromagnetic region below T_C, resistivity can be explained by electron-magnon scattering and electron-phonon scattering. Electron magnon scattering gives a T^2 term (ρ_{e-m}) in resistivity of a ferromagnetic metal.

1.5.5 Spin-disorder scattering

In non-magnetic metals, the dominant scattering is the scattering of electrons with the lattice defects and phonon. But, in case of magnetic metals, an additional scattering takes place due to the scattering of electrons by spin-disorder. De Gennes and Freidel theoretically predicted that the change in slope of resistivity curve around the magnetic ordering temperature is occurred due to the spin-disorder scattering. At high temperature, in paramagnetic region, the magnetic spins are thermally fluctuating and randomly oriented. This fluctuation is very large across the transition temperature. Below ordering temperature at low temperature, the spins are aligned. This causes the reduction is resistivity below transition temperature.

1.5.6 Electron-electron scattering

As we have already discussed in the Fermi-liquid theory in the previous section, the electron-electron interaction at finite temperature provides a T^2 term (ρ_{e-e}) in the total resistivity of metal.

1.6 Magnetocaloric effect

Modern society depends very much on readily available cooling. Cooling technology based on magnetic refrigeration has several advantages over that of conventional gas compression [30, 31]. The cooling efficiency of magnetic refrigerator reaches upto 30-60% [32] whereas it is just 5-10% in case of conventional gas compression technology [33]. Moreover, magnetic refrigeration is environmentally friendly as it does not involve any kind of ozone-depleting gases, which mainly cause pollution and global warming [33, 34].

In 1917, Weiss and Piccard discovered the magnetocaloric effect (MCE) [35]. Debye in 1926 and Giaque in 1927 proposed to develop magnetic refrigeration cycles for achieving ultralow temperature by adiabatic demagnetization [36, 37]. In 1933, it was experimentally first demonstrated by Giaque and MacDougall in magnetic refrigerant $Gd(SO_4)_3$; $8H_2O$ by attaining the low temperature 250 mK [38]. Primarily, researches were mainly focused on the magnetic cooling near room temperature for the domestic and industrial purposes. Several rare earth metals and compounds based on Gd [39], $Gd_5Si_xGe_{1-x}$ [40] have been investigated as room temperature magnetic refrigerants. Eventually, for economic benefits some new materials other than rare earth containing compounds were discovered for the same purpose such as Mn based alloys and compounds, LaFeSi and Fe_2P type systems [31, 41, 42, 43, 44, 45, 46, 47]. Extensive researches are carried out to extend the temperature range from room temperature to ultralow temperature. Recently, the main concern is the storage and liquefaction of H_2 gas below 20 K. Garnet $Gd_3Ga_5O_{12}$ (GGG) is mostly used for cooling in the temperature range 1.5 K to

20 K [48, 49, 50, 51, 52, 53, 54]. In this regard, rare earth based perovskites and their doped compounds are chemically stable at cryogenic temperatures, and can be made easily. Whether in the vicinity of low temperature or room temperature, the main concern of refrigeration is to have large MCE. The two basic parameters of MCE are the isothermal magnetic entropy change (ΔS_m) and adiabatic temperature change (ΔT_{ad}). Besides them, magnetic cooling/heating capacity (MC) is an another parameter to determine the amount of heat transfer between hot and cold reservoirs in an ideal refrigeration cycle.

1.6.1   Introduction

MCE is an intrinsic property of a material. It is a magneto-thermodynamic phenomenon in which the temperature of a suitable material changes with varying magnetic field. In a MCE material, the degrees of freedom associated to lattice and spins are coupled with each other. Similar to Carnot's refrigeration cycle, the magnetic refrigeration also undergoes through four following steps as displayed in Fig. 1.9 :

Adiabatic magnetization

The MCE material is kept as isolated and then, a magnetic field is applied. The magnetic entropy reduces as the spins of magnetic material get aligned along the field direction. To conserve the total energy, thermal energy increases. As a result, the temperature of the material increases from T to $T+\Delta T_{ad}$.
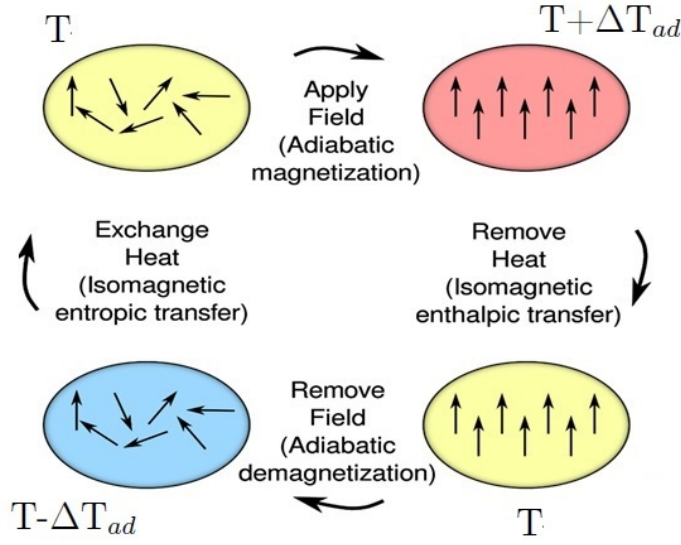
Figure 1.9: A schematic representation of a magnetic refrigeration cycle. The arrows indicate the direction of the magnetic moments.

Isomagnetic enthalpic transfer

This extra heat Q is removed by connecting this material with a liquid/gaseous He. In this step, the magnetic field is kept constant to avoid reheating of the material. After sufficient cooling, the material and the liquid/gaseous He are separated.

Adiabatic demagnetization

The sample is now at an another isolated environment. If we decrease the magnetic field slowly, spins get randomized, as a consequence, the spin entropy increases which reduces the lattice entropy. Therefore, the sample temperature decreases from T to T-ΔT_{ad}.

Isomagnetic entropic transfer

The material is now cooled. It is thermally connected to the environment to be refrigerated. Magnetic field is kept constant to avoid reabsorbing the heat. An amount of heat transfers from the refrigerated environment to material.

Thus, the decrease in temperature of the magnetic material helps to cool the refrigerator.

1.6.2   Thermodynamics of MCE effect

Since magnetic entropy is a state function, the change in entropy can be written as

$$dS = (\frac{dS}{dT})_{p,H}dT + (\frac{dS}{dp})_{T,H}dp + (\frac{dS}{dH})_{p,T}dH \qquad (1.26)$$

where S is the entropy, p is the pressure and H is the applied magnetic field. If the material is placed under isobaric (p=constant) and isothermal (T=constant) conditions, then the change in magnetic entropy only depends on the applied magnetic field. According to Maxwell's relation,

$$(\frac{dS}{dH})_T = (\frac{dM}{dT})_H \qquad (1.27)$$

M is the magnetic moment of the sample. By integrating the above equation, we can get the isothermal magnetic entropy change as

$$\Delta S_m(T,H) = S_M(T,H) - S_M(T,0) = \int_0^H (\frac{dM}{dT})_H dH \qquad (1.28)$$

This equation tells us that the change in magnetic entropy is dependent on the temperature derivative of magnetic moment of the material and also the field change. The parameter MC can be estimated from the following equation

$$MC = \int_{T_1}^{T_2} \Delta S_m dT \qquad (1.29)$$

where T_1, T_2 are the temperatures of cold and hot reservoirs respectively.

From the second law of thermodynamics, the change in entropy is given by

$$dS = \frac{dQ}{T} \qquad (1.30)$$

where, dQ is the amount of heat required to increase the temperature of the material.

Heat capacity of the sample at constant pressure can be written as

$$C_p = (\frac{dQ}{dT})_p \qquad (1.31)$$

Therefore, eq. (1.27) can be written as

$$dS = (\frac{C_p}{T})dT + (\frac{dM}{dT})dH \qquad (1.32)$$

In the adiabatic condition, $dQ=0 \implies dS=0$. Therefore, the change in temperature of the sample is given by

$$\Delta T_{ad} = -\int_0^H (\frac{T}{C_p})(\frac{dM}{dT})_H dH \qquad (1.33)$$

The adiabatic temperature change (ΔT_{ad}) of the material is proportional to the absolute temperature, the temperature derivative of magnetic moment and the magnetic field change; and inversely proportional to the sample heat capacity. ΔT_{ad} can be obtained from the field-dependent magnetization and zero-field heat capacity data. The total entropy $S(0, T)$ at zero magnetic field is given by $S(0, T) = \int_0^T C_p(0, T)/T \, dT$ and then $S(H, T)$ may be evaluated by subtracting the corresponding $\Delta S_m(H, T)$ determined using eq.(1.28) from this estimated value of $S(0, T)$. The isentropic temperature difference between the entropy curves $S(0, T)$ and $S(H, T)$ gives the value of ΔT_{ad}.

ΔS_m also can be determined solely from the field dependent heat capacity data. The total entropy $S(T, H)$ is calculated from the heat capacity data at a fixed magnetic field by using the following equation

$$S(T, H) = S(T_0, H) + \int_{T_0}^T \frac{C_p(H, T)}{T} \, dT. \tag{1.34}$$

The magnetic entropy for a ferromagnet above Curie temperature is given by

$$S_m(T, H) = Nk_B[ln(2J + 1) - \frac{1}{2} \frac{CH^2}{(T - T_C)^2}] \tag{1.35}$$

where C is the Curie constant, J is the total angular momentum of an atom and $R \ (= Nk_B)$ is the gas constant. In the limit of $T \longrightarrow \infty$ and $H \longrightarrow 0$, the magnetic entropy attains its maximum value in the disordered state. Therefore, the maximum magnetic entropy value per mole of magnetic atoms is

$$S_m(T, H) = Nk_B ln(2J + 1) = Rln(2J + 1) \tag{1.36}$$

1.7 Critical behavior associated to magnetic phase transition

The phenomenon associated with a continuous phase transition is called critical phenomenon. The singular behavior in the vicinity of the critical point is characterised by a set of parameters, called as critical exponents. Different physical properties such as spontaneous magnetization (M_S), initial susceptibility (χ_0), correlation length (ξ), isothermal magnetization ($M(H)$) and heat capacity (C_p) obey some power laws of the reduced temperature $t = |T - T_C|/T_C$ corresponding to the critical exponents β, γ, ν , δ and α. In case of a continuous phase transition, the critical exponents should be independent of the microscopic details of a homogeneous magnetic system due to the divergence of correlation length near the transition point. The exponents are universal, i.e., they are same for a wide range of materials. Hence, these critical exponents define a universality class which are mentioned in the Table 1.1. The theoretical models based on critical exponents are: mean-field model, 3D-Heisenberg model, 3D-Ising model, etc.

Table 1.1: Theoretical values of critical exponents of three models.

Technique	Models	α	β	γ	δ
Theory	Mean-field	0	0.5	1.0	3.0
	3D-Ising	0.11	0.325	1.241	4.82
	3D-Heisenberg	-0.11	0.365	1.386	4.80

Recently Y. Su. *et al.* [55] have reported the critical behavior of most of the family members of RTiO$_3$ (for R= Dy, Ho, Er, Tm, Yb) by using the magnetocaloric and conventional heat capacity data. The critical exponents of RTiO$_3$ single crystals belong to the 3D-Heisenberg universality class.

1.8   EuTiO$_3$

1.8.1   Magnetism in EuTiO$_3$

In ETO, the magnetic contribution comes only from Eu^{2+} ion. Eu^{2+} is highly localised due to having a stable electronic configuration $4f^7$ with high spin ($S = 7/2$). Eu^{2+} ions order themselves in an antiferromagnetic arrangement with Néel temperature T$_N$=5.5 K. In G-type antiferromagnet (AFM), Eu^{2+} has 6 nearest neighbor antiparallel Eu^{2+} spins and 12 next-to-nearest neighbor parallel Eu^{2+} spins [56, 57]. There are four types of possible exchange mechanisms in ETO: (i) a direct exchange between Eu-$4f$ states which is very weak as there is very less overlapping between Eu-$4f$ orbitals, (ii) a superexchange interaction between Eu^{2+} spins via the intermediatory non-magnetic ion (Ti^{4+}), (iii) a 90° superexchange via O-$2p$ states and (iv) an indirect exchange via Eu-$5d$ states. The superexchange via Ti-$3d$ states is more favorable for the AFM ordering of Eu^{2+} spins. Whereas, the next-to-nearest neighbor ferromagnetic ordering is due to the indirect exchange via Eu 5d states [58]. Although ETO is an AFM, it has positive Curie-Weiss temperature (θ_{CW}). This positive value of θ_{CW} can be reproduced by assuming that the absolute value of nearest-neighbor AFM interaction (J_1) is slightly smaller than the next-to-nearest neighbor exchange interaction (J_2) [59]. From the mean-field approximation, the calculated values of J_1=- 0.021 k$_B$ K and J_2=+ 0.040 k$_B$ K. The value of the dipolar interaction ($\sim g^2 \mu_B^2 S^2 / r^3$) between Eu^{2+} spins is 0.37 cm^{-1} = 0.52 k$_B$ K; r is the distance between Eu^{2+} spins [60].

1.8.2 Crystal structure

At room temperature, ETO is a cubic perovskite with lattice parameter $a=3.905$ Å (space group $Pm3m$) [61]. Wyckoff positions of atoms in ETO are: Ti on $1a$ $(0, 0, 0)$, Eu on $1b$ $(1/2, 1/2, 1/2)$ and O on $3d$ $(1/2, 0, 0)$ [62]. ETO undergoes a structural phase transition from cubic to tetragonal phase at $T_S=282$ K. In tetragonal phase, Wyckoff positions of atoms are Ti at $4c$ $(0, 0, 0)$, Eu at $4b$ $(0, 1/2, 1/4)$, O1 at $4a$ $(0, 0, 1/4)$ and O2 at $8h$ $(x, x+1/2, 0)$ [for $x\sim1/4$] with space group $I4/mcm$ [62]. At high temperature, the tilting of corner-linked TiO_6 octahedral unit causes the structural transition [63].

1.8.3 Electronic structure

While the other rare-earth titanates are Mott insulators, ETO is a band insulator. The band structure of ETO has been studied in Akamatsu *et al.* [58] and first principle calculation with DFT has been performed by Birol and Fennie [64]. In band structure of ETO, Ti-$3d$ states are completely unfilled and O-$2p$ states are occupied. Here, O-$2p$ states and Ti-$3d$ states form the valence band and conduction band respectively. The half-filled Eu-$4f$ states are highly localised. So, they form a narrow band below Fermi level in this gap between conduction band and valence band. The hopping between Eu-$4f$ orbital and neighboring cations is very less as the radius of $4f$ orbital is very smaller than that of $5s$ and $5p$ orbitals.

1.8.4 Magneto-dielectric coupling

ETO is not a typical ferroelectric material. It exhibits quantum paraelectricity below T_N. The onset of ferroelectric ordering cannot take place because of low temperature quantum fluctuations. Katsufuji et $al.$ [59] have discussed the influence of magnetic field on the dielectric constant (ε) of ETO. The dielectric constant shows a huge drop just below T_N. With the application of magnetic field, the low temperature ε increases and the cusp at T_N vanishes gradually. A huge magneto-dielectric effect has been observed in ETO which yields 7% change in ε due to the application of magnetic field 1.2 T at 2 K. To get the coupling between magnetic and dielectric properties of a material, their energy scales must be comparable. If any material has a specific infrared allowed optical phonon mode with low frequency which is called soft phonon mode, the energy related for dielectric constant is of the order of 10 meV which is comparable to magnetic interaction. The dielectric constant of ETO is responsive to magnetic field because of the coupling of a soft phonon mode $T_{1\mu}$ and the pair correlation of localised Eu^{2+} spins. The dielectric constant $\varepsilon(T)$ is related to the pair correlation of Eu spins by the following relation

$$\varepsilon(T, H) = \varepsilon_0(T)(1 + \alpha < S_i.S_j) >) \tag{1.37}$$

where $\varepsilon_0(T)$ is the dielectric constant which is independent of spin pair correlation. α is the coupling between spin correlation and dielectric constant. The hybridization of Eu-$4f$ orbital and O-$2p$ orbital varies depending on the configuration of Eu spins which modifies the frequency of the soft phonon mode. This frequency variation of soft phonon mode is associated to Eu-O stretching motion.

1.8.5 Antiferrodistortive phase transition

As the radius of Sr^{2+} and Eu^{2+} is same, therefore, it would be expected to undergo an antiferrodistortive transition at the cubic-tetragonal structural transition temperature T_S=282 K similar to $SrTiO_3$ (STO). Bussman-Holder *et al.* [63] suggested that a structural phase transition of ETO at 282 K is analogous to that in STO at 106 K. This anomaly is quite closer to 298 K where a theoretical phase transition is expected due to the tilting of oxygen octahedral. This prediction is confirmed from the specific heat anomaly at 282 K as similar as STO. Allieta *et al.* [62] provided this evidence from their high resolution synchrotron x-ray diffraction data. Later on, Reuvenkamp *et al.* [65] have found a distinct anomaly at 282 K in thermal expansion co-efficient of ETO and claimed that this as a first order transition in nature. Spalek *et al.* [66] have found the transition at 284 K for ETO single crystal from resonant ultrasound spectroscopy. Therefore, it can be concluded that the structural transition temperature varies may be due to its dependency on oxygen stoichiometry or density of sample or defects in sample. Guguchia *et al.* [67] have shown that the structural transition is also reflected in the magnetic moment versus temperature curve and with increasing field strength the transition temperature shifts towards higher temperature.

1.8.6 Magnetostriction

Reuvekampp *et al.* [68] first performed the magnetostriction experiment across the AFM phase transition temperature T_N= 5.5 K. The temperature dependence of the change in the sample length has been observed with varying the magnetic

field from 0 to 6 T. At zero field, $\frac{\Delta L}{L}$ is negative and near 5.5 K it drastically drops. With increasing magnetic field strength, the anomaly near T_N shifts towards lower temperature. Above 0.625 T, the negative magnetostriction becomes positive. As the field exceeds the spin-flop transition field 1 T, the magnetostriction is positive and small in magnitude. This behavior has a resemblance to the magneto-dielectric behavior. The abrupt drop in ε at T_N has caused due to the hardening of a optical mode and with increasing field strength it gets softened. Similarly, the magnetostriction data above 1 T supports the mode softening. Also, the thermal co-efficient $\alpha = \frac{l}{L}(\frac{dL}{dT})$ versus temperature plot at zero field exhibits a sharp peak near 5.5 K which behaves same as $\frac{\Delta L}{L}$ with increasing field. Above 1 T, this anomaly completely disappears and α changes its sign from positive to negative.

2

Experimental details

In this chapter, the experimental procedures and techniques adopted throughout the thesis work, to prepare and characterize the undoped and doped $EuTiO_3$ samples, are described in details. The polycrystalline form of all three compounds $EuTiO_3$, $EuTi_{1-x}Nb_xO_3$ ($x=$ 0.10, 0.15, 0.20) (ETNO) and $EuTi_{0.9}V_{0.1}O_3$ (ETVO) were made by the conventional solid state reaction method. Then, the two compounds ETO and ETNO were used to prepare single crystals by the travelling solvent float zone method. X-ray diffraction technique was used to check the phase purity and structure of all the samples. To investigate the magnetic, electrical and thermal properties, a superconducting quantum interference device-vibrating sample magnetometer (SQUID-VSM)(Quantum Design), a cryogen free measurement system (Cryogenic Ltd.), and a physical property measurement system (PPMS)(Quantum Design) were used.

2.1 Sample preparation and Characterization

2.1.1 Polycrystalline sample preparation : Solid state reaction method

The solid state reaction is the most convenient and direct method to prepare a polycrystalline material at which the raw oxides or carbonates in their solid phases start to react at high temperature in air or a controlled atmosphere (i.e., H_2/Ar mixture or O_2, etc.). This process involves the following steps: weighing of raw materials, intermediate grindings and heatings, final preparation of a pellet or cylindrical rods by hydraulic press and sintering.

To prepare the polycrystalline ETO powder samples, a stoichiometric mixture of Eu_2O_3 (pre-heated) and TiO_2 were heated at $1000-1100°C$ for few days followed by intermediate grindings. The obtained powder was pressed into two cylindrical rods which were finally sintered at $1100°C$ in the same environment. For ETNO ($x= 0.10, 0.15, 0.20$) or ETVO, in addition to Eu_2O_3 (pre-heated) and TiO_2, Nb_2O_5 or V_2O_5 was used respectively. All the above heat treatments were done in the reduced atmosphere containing 5% H_2 and 95% argon to get Eu^{2+} instead of Eu^{3+}
.

2.1.2 Single crystal growth : Travelling solvent float zone method

The travelling solvent float zone method is one of the most powerful tools to prepare a high quality single crystal. The advantage of this method over the other techniques is that it avoids contamination from crucible and also it can produce
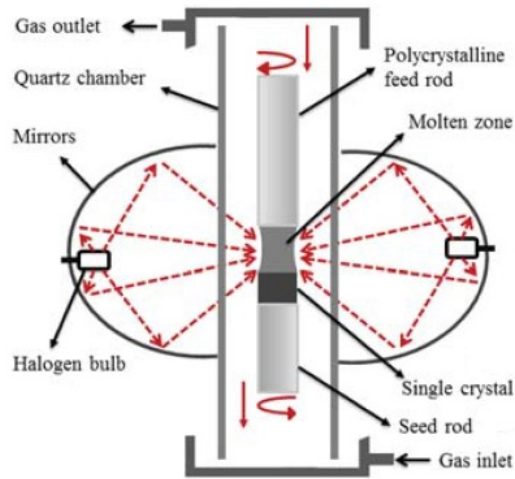
Figure 2.1: Schematic diagram of floating zone technique illustrating the key features of a floating zone image furnace.

large single crystal in length, etc. Here, we used a four-mirror optical floating zone furnace FZ-T-10000-H-VPM (Crystal System Co.) [shown in Fig. 2.1] which consists of four ellipsoidal mirrors made of Pyrex glass coated with highly reflective aluminum. The maximum operating temperature is 2200°C in atmosphere (air, nitrogen, oxygen, argon, etc) and the pressure ranges from 5×10^{-5} to 10 bars. Crystals can be obtained up to 150 mm in length and 10 mm in diameter, with a growing rate of 0.05-27 mm/h and a 5-60 rpm rotating rate. This method needs two polycrystalline rods (one is feed rod and another is seed rod). The feed rod is suspended from a platinum hook and the seed rod is put onto a seed holder. The infrared radiation coming from four halogen lamps is reflected by the four mirrors and focused on to the sample rod. A suitable percentage of the total lamp power is applied to melt a small portion in junction ends of these feed and seed rods. After a while, when the molten portions of feed and seed rods take a round

shape, they are touched in liquid state. The molten zone is floated in between seed and feed rods due to the competition between gravitational force and surface tension. There are two shafts (upper and lower) which can move independently or in synchronized mode. The motion of upper shaft controls the feed speed whereas that in the lower shaft controls the seed speed. With a suitable feed and seed speed in synchronized or non-synchronized mode, the molten (floating) zone is translated downward along the length of the feed rod. The end of the molten zone gets solidified as it goes far away from the heating zone and the single crystal is grown. During the entire time of crystal growth, the feed and seed rods are rotated in opposite directions to get a homogeneous microstructural texture. The crystal growth takes place inside a quartz tube. The parameters such as the pressure of the gas which is supplied as the atmosphere of crystal growth, feed or seed speed and lamp power are tuned in a controlled manner during the crystal growth.

2.1.3 Powder x-ray diffraction
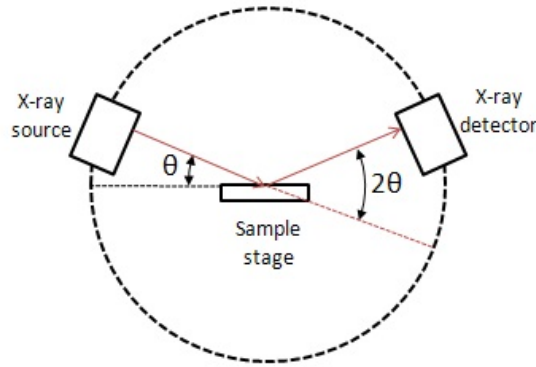
Figure 2.2: Schematic diagram of a powder diffractometer in Bragg-Brentano geometry.

Powder x-ray diffraction (XRD) method is an easier and most widely used characterization tool to check the phase purity of a material. Max von Laue discovered in 1912 that any crystal acts as a three-dimensional diffraction grating if the wavelength of x-ray matches with the spacing between planes in that crystal lattice. As each material has its own unique diffraction pattern, the composition of a material can be identified from this powder diffraction technique. Also, it provides information about the crystal structure as well as the atomic spacing. The term powder means that the crystalline domains are randomly oriented in the sample. An x-ray diffractometer consists of three basic elements: an x-ray tube, a sample holder, and an x-ray detector. X-rays generated from a cathode ray tube, filtered to get a monochromatic x-ray, collimated to concentrate and then directed towards the sample. In powder XRD method, incident monochromatic x-rays are projected to very fine powder sample where different grains remain randomly oriented with respect to incident beam and get scattered by the different atomic planes of the crystalline substance and a diffraction pattern is formed by the interference of scattered rays. The diffracted rays which are in same phase will give a constructive interference pattern. A schematic of a powder diffractometer in Bragg-Brentano geometry [common in modern diffractometers] is displayed in Fig. 2.2. In diffraction experiment, the scattered x-rays are collected by the x-ray detector as they carry the information about the electron distribution in the materials. Here, elastic scattering is considered in which the wavelength of the scattered rays does not change from the incident one. Although the individual atom scatters radiation in all directions, there are only a few directions in which the scattered waves interfere constructively and sharp interference maxima (peaks) with the same symmetry are observed in substances. The peaks in an XRD pattern

are directly related to the atomic distances. Let us consider an incident x-ray beam interacting with the atoms arranged in a periodic manner. The atoms can be viewed as forming different sets of lattice planes which are represented by the Miller indices (hkl). For a given set of (hkl) planes, the constructive interference pattern occurs only when it satisfies the condition

$$2d\sin\theta = n\lambda, \tag{2.1}$$

This is known as Bragg's law of diffraction [20]. Here $d =$ interatomic spacing between two parallel lattice planes, $n=$ order of diffraction, $\theta =$ angle between the incident ray and the lattice plane and λ is the wavelength of x-ray. The diffracted x-rays are collected by solid state detector and a diffraction pattern is produced when scan is performed through a certain range of angle. Rigaku diffractometer (TTRAX III) is used to perform powder XRD of samples. It is operated at 9 kW with Cu K$_\alpha$ radiation. Samples were scanned from 10° to 90° at a step of 0.02°. Profile fitting of diffraction pattern was done by Rietveld method [69] using the FULLPROF program [70]. Rietveld method is an algorithm for fitting the experimental diffraction pattern which minimizes the mismatch between theoretical and observed diffraction patterns. This theoretical data are based on the profile information, atomic positions, crystal parameters. The background is fitted with either a polynomial or by specifying a series of interpolated points. The difference between the observed and calculated profiles is minimized based on a least-squares regression.

2.2 Magnetic and physical property measurement systems

2.2.1 Magnetic measurements

MPMS SQUID-VSM and PPMS VSM were used to investigate the temperature and magnetic field dependence of the magnetization of the studied single crystals and polycrystalline materials. In most of the cases, the effect of demagnetizing field is very less. On the other hand, if the demagnetizing field has a larger value then it reduces the measured inverse susceptibility (χ^{-1}), but does not change the value of Curie constant as well as the effective paramagnetic moment. Whereas, the value of Curie-Weiss constant θ_{CW} changes. To minimize the demagnetizing factor, for the magnetic measurements, we have used approximately parallelepiped shaped pieces with lengths much larger than the other two dimensions and the magnetic field is applied along the length of the samples. We have not been able to cut the single crystals along any particular crystallographic axis due to the lack of Laue diffraction facility.

DC magnetization: SQUID-VSM

MPMS 3 SQUID-VSM has the properties: (i) the operating temperature ranges from 1.8 K to 400 K with a maximum temperature sweep rate of 50 K/min, (ii) the field ranges from - 7 to +7 T with a maximum field sweep rate of 700 Oe/sec, and (iii) the magnetization sensitivity is of 5×10^{-8} emu. The magnetometer has three main sections (a) dewar and probe with VSM motor (b) superconducting magnet and SQUID-VSM detection system and (c) the electronic control system.

The dewar consists of an inner liquid helium reservoir and outer liquid nitrogen jacket. The liquid helium is used both for maintaining the superconducting state of the magnet and detector as well as for cooling the sample space.
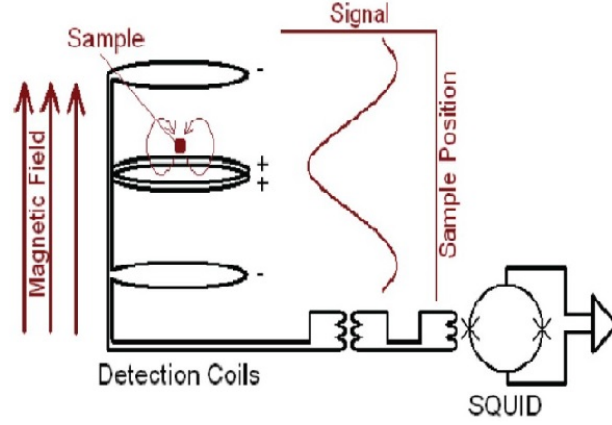
Figure 2.3: A simplified schematic diagram of SQUID-VSM detection system. Ref.[71]

Figure 2.3 illustrates a schematic of the SQUID-VSM detection system [71]. The superconducting detection coils are framed as a second order gradiometer, with counterwound outer loops which make the set of coils non-responsive to uniform magnetic fields and linear magnetic field gradients. Only local magnetic field produces a current in detection coil. It is assumed that the sample dimension is negligible compared to coils dimension. As the sample moves through the coils, the magnetic flux associated with the coils changes. Since the detection coil, the connecting wires and the SQUID input coil form a close superconducting loop, any change in magnetic flux causes a change in the persistent current in the detection circuit. Such a change in persistent current is proportional to the change in magnetic flux. Since the SQUID acts as a highly linear current-to-voltage converter, the variation in the current in the detection coil produces corresponding variation

in output voltage of the SQUID, which is proportional to the magnetic moment of the sample. The SQUID function is based on the two phenomena: flux quantization in a superconducting ring and Josephson effect. The Josephson effect refers to the phenomenon of current flow across two weakly coupled superconductors, separated by a very thin insulating barrier. The SQUID feedback cancels the current in the detection coils, therefore, no current actually flows in them, and the feedback current yields the actual SQUID voltage that gives the sample magnetization value. The SQUID voltage is amplified and digitized by the instrument electronics.

The VSM linear motor system of the SQUID-VSM vibrates the sample at frequency ω about the center of the detection coils, where the signal peaks as a function of sample position, z. This produces a SQUID signal (V) as a function of time (t):

$$V(t) = AB^2 \sin^2(\omega t), \tag{2.2}$$

as in case of small vibration amplitudes, $V(z) = Az^2$ and $z(t) = B \sin(\omega t)$. Here, A is a scale factor associated to the magnetic moment of the sample. B is the amplitude of sample vibration. Since $\sin^2(\omega t) = \frac{1}{2}(1- \cos(2\omega t))$ (by identity), the technique of a lock-in amplifier is applied to isolate and quantify the signal occurring at frequency 2ω, which should be caused exclusively by the sample if the vibration frequency is chosen properly. Briefly, this is achieved by multiplying the measured signal with a phase-corrected reference signal at 2ω and then extracting the dc component of the result. This dc component is proportional to the 2ω component of the measured signal. This technique quickly and precisely isolates the sample signal from other noise sources, including drifting SQUID signal and mechanical noise sources synchronized to the sample vibration. The lock-in am-

plification of the SQUID signal is executed by digital electronics in the SQUID control module.

Vibrating sample magnetometer: PPMS
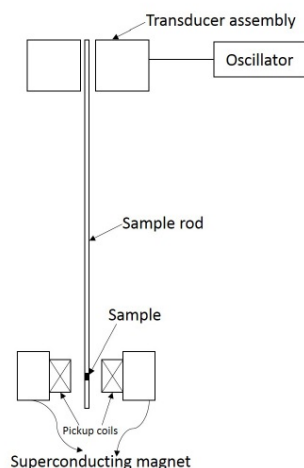
Figure 2.4: Schematic diagram of vibrating sample magnetometer [72].

The magnetization measurements were also done with the help of PPMS VSM option. It has the specifications: (i) the operating temperature ranges from 1.8 K to 400 K, (ii) the field ranges from - 9 to +9 T with a maximum field sweep rate of 180 Oe/sec. A schematic diagram of vibrating sample magnetometer is shown in Fig. 2.4. The VSM option for the PPMS consists of a linear motor transport (head) for vibrating the sample, a coil set puck for detection purpose, electronics for driving the linear motor transport and detecting the response from the pickup coils [73]. The linear motor transport has an oscillator and a transducer assembly. The oscillator creates a sinusoidal signal and the transducer assembly translates it into vertical vibration. The sample vibrates with a known frequency and amplitude. In a typical magnetic measurement, sample is kept inside a uniform magnetic

field to magnetize the sample and then the sample is mechanically vibrated near the detection or pickup coil. As sample is vibrating, magnetic flux is changing with time. So, according to Faraday's Law of induction, a voltage is induced in detection coil. The induced voltage in the pickup coil, which is proportional to magnetic moment of the sample, is then measured by using a lock-in amplifier. By using a compact gradiometer pickup coil configuration, relatively large oscillation amplitude of $1-3$ mm peak-to-peak and a frequency of 40 Hz, the VSM is able to resolve the change in magnetization of magnitude less than 10^{-6} emu.

2.2.2   Resistivity

The dc or ac electrical resistivity of the samples was measured by standard four-probe technique [74, 75]. Four thin copper or gold wires were connected to the rectangular-shaped sample using silver paint or silver epoxy contacts. These four wires act as four probes, in which current is allowed to flow between two outer probes and voltage is measured between two inner probes. The four contact regions are coated by silver paint. At first, the painted samples were heated at 100-150°C for 15 minutes to achieve good ohmic contacts and then the contacts were made at room temperature. The dc resistivity was measured as a functions of temperature down to 1.5 K, and of applied magnetic field up to 9 T in a variable temperature insert (VTI) of a cryogen free measurement system (Cryogenic Ltd.).

To measure the dc resistivity, a constant dc current of appropriate level was sent through the sample from a Keithley 224 current source and the voltage across the voltage leads was measured by using a Keithley 2182A nanovoltmeter with current flowing in the forward and reverse directions to eliminate the contribu-

tions of thermoelectric effect and offset voltage of the nanovoltmeter. The sample temperature was controlled by using a Lake Shore temperature controller (Model 340) and measured by a calibrated Cernox (ceramic-oxynitride) sensor. The signals from the voltage probes, temperature sensor, and magnet power supply of VTI were recorded by a Labview software program on the computer to get the temperature and magnetic field dependence of the resistance (R) of the samples.

The ac resistivity was measured using the ac transport measurement option in PPMS when the voltage signal in dc mode is small. A constant sinusoidal current of appropriate amplitude and of frequency 13.7 Hz was allowed to flow through the current leads and the ac voltage across the sample voltage leads was measured and amplified by a lock-in amplifier. The resistance of the samples was recorded as functions of temperature and magnetic field.

The resistivity of a sample is given by

$$\rho = R\frac{A}{l},\tag{2.3}$$

where R = the resistance of the sample, l = distance between two inner voltage leads and A = the cross sectional area. However, it may include some error due to the inappropriate determination of cross sectional area, as the value will depend on the precise path of the current through the sample. It has been assumed that the current flows uniformly throughout the width of the sample.

2.2.3 Specific heat

Specific heat measurements of the studied samples were done in PPMS using a two-tau relaxation method [76] which measures the heat capacity at constant pressure

$$C_p = \left(\frac{dQ}{dT} \right)_p.$$ (2.4)

In heat capacity option, a certain amount of heat (Q) is applied to the sample for a certain time with a constant heater power. Then heat is removed during a cooling period. Duration of heating and cooling periods remain same here. The heat capacity at a particular temperature is measured by recording the differences in temperature between the sample, sample platform, and puck during heating and cooling periods. The schematic diagram of heat capacity probe of Quantum Design PPMS is shown in Fig. 2.5. A heater and a thermometer are connected to the bottom side of the sample platform. Electrical and thermal connections to the platform heater and platform thermometer are done with the help of small wires. Sample platform remains suspended by these wires. The sample is attached to the platform using Apiezon H or N grease to ensure good thermal contact. The heat capacity puck is then inserted into the PPMS, which is equipped with a 9 T magnet and capable of a temperature range of 1.9 to 400 K. During the measurement, high vacuum condition is maintained to assure the thermal conductance between platform and thermal bath only via wires. A single measurement cycle consists of a heating period followed by a cooling period.

The two-tau model is normally used when poor thermal contact between the sample and the platform exists or when a large sample results in a temperature difference between the sample and the platform [77]. This is then compared to a
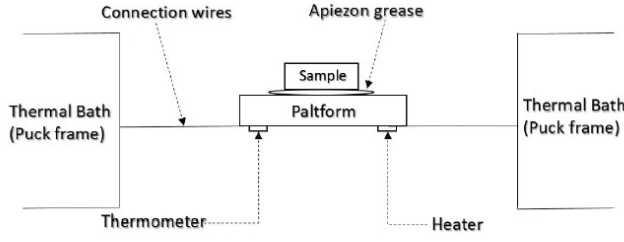
Figure 2.5: Schematic diagram of a PPMS heat capacity puck showing the thermal connections to sample and sample platform.

model involving perfect thermal contact between the sample and platform to give the relaxation model. An addenda measurement of the heat capacity of the sample platform and the grease is subtracted from the measured signal to determine the sample heat capacity [77, 78]. By considering the heat flow between the sample and sample platform as well as that between the sample platform and the puck, the thermal diffusion equation can be expressed as below [77]:

$$C_P \frac{dT_P(T)}{dt} = P(t) - K_w(T_P(t) - T_b) + K_g(T_S(t) - T_P(t)), \qquad (2.5)$$

$$C_S \frac{dT_S(T)}{dt} = -K_g(T_S(t) - T_P(t)), \qquad (2.6)$$

where C_S (C_P) is the heat capacity of the sample (sample platform plus the grease), $T_S(t)$ ($T_P(t)$) is the temperature of the sample (sample platform), K_w is the thermal conductance of the wire, K_g is the thermal conductance between the sample and sample platform, T_b is the temperature of the thermal bath (puck), and $P(t)$ is the power supplied by the heater. The heater power $P(t)$ is a step function, which is fixed at P_0 during the heating stage and is removed during the cooling period. In case of a good thermal contact, when there is no temperature difference between the sample and the platform, the two-tau model is reduced to the simple

model containing just one time constant τ_1.

2.2.4 Thermal expansion and Magnetostriction

The thermal expansion and magnetostriction measurements were performed by capacitive method using a miniature tilted-plates dilatometer. In 1998, M. Rotter developed a small capacitive sensor to measure thermal expansion and magnetostriction of small irregular shaped samples [79]. The capacitance method is one of the most sensitive methods which is able to detect small length changes of solids. Here, tilted plate construction has been followed to design the capacitive cell so that the high plate area and low volume give the good sensitivity along with a very small sensor. The data of thermal expansion and magnetostriction were analyzed with the help of packaged python program.

Tilted Dilatometer
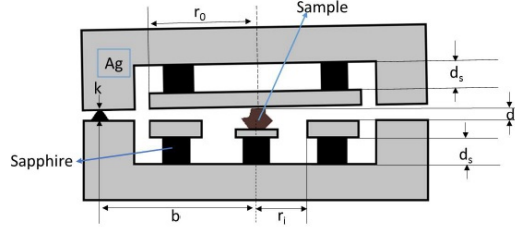
Figure 2.6: Schematic diagram of tilted-plates dilatometer.

Dilatometer is capable to measure over wide range of temperature from 2-300 K. Figure 2.6 shows a schematic picture of a tilted dilatometer. Dilatometer consists of two main parts: lower and upper dilatometer plates. Both the upper and lower

dilatometer plates consist of silver capacitor plates and plate holders. The sample is kept in between two capacitor plates. Two plates are separated from each other by two brass needle bearings and the sample. Two needle bearings also define an exact pivot point (k) to avoid any transverse shift between the upper and lower plate holders. Both capacitor plates and the sample support are insulated from the holders by sapphire washers. The change in capacitance measured by dilatometer has four types of contributions which are mentioned in the following:

1. length change of the sample ; 2. change in the radii of two capacitor plates; 3. length change of the silver plate holders; 4. partial compensation by the change of thickness of the capacitor plates and the sapphire washers.

Here, r_o is the radius of outer capacitor plate, r_i is the inner plate radius, b is the separation between center of capacitor and pivot and d_s is the thickness of the sapphire washers. By considering all four types of contributions, the gap $d(T)$ at certain temperature T has been determined from the measured capacitance with the help of some complicated formula [79]. The relative length change of the sample has been estimated using the obtained gap by the following relation [79],

$$\frac{\Delta l_{Sample}}{l}(T) = \frac{\Delta d_{Sample}}{l_{Sample}}(T) - \frac{\Delta d_{Ag-Sample}}{l_{Ag-Sample}}(T) + \frac{\Delta l_{Ag-Lit}}{l}(T) \qquad (2.7)$$

where Δd_{Sample} is the change in gap due to sample, $\Delta d_{Ag-Sample}$ is the gap change due to the silver calibration sample and $\frac{\Delta l_{Ag-Lit}}{l}$ is the relative length change.

Analysis of critical behavior associated with the antiferromagnetic transition of single crystalline EuTiO$_3$

3.1   Introduction

In spite of several measurements on the low temperature AFM-PM transition as well as the high temperature structural phase transition, there is no report on the critical analysis of ETO. Critical analysis of a phase transition is one of the valuable studies to understand the nature of interaction between spins in the system. However, due to inhomogeneity, polycrystalline materials exhibit a rounded peak around the transition temperature which will include an erroneous determination of critical exponents. The value of exponent is also affected by the grain size. To get an exact value of critical exponent, the average grain size must be larger than the correlation length in the critical region. Therefore, it is expected to have high

quality single crystalline material to determine the intrinsic values of exponents. Here, we are interested to study the critical behavior of single crystalline ETO based on the thermal measurements.

3.2   Experimental details

Single crystals of EuTiO$_3$ were grown by travelling solvent floating zone technique using a four-mirror image furnace. The sample preparation part is described in details in chapter 2. Phase purity was checked by powder XRD method in a Rigaku diffractometer (TTRAX III). No trace of impurity phases were detected within the resolution of XRD. The magnetization measurements were done using a SQUID-VSM. The specific heat (C_p) was measured using a PPMS. The thermal expansion of the sample length (L) was measured with field (H) parallel to sample length ($H \parallel L$) by capacitive method using miniature tilted plates dilatometer.

3.3   Results and Discussions

To investigate the effect of magnetic field on the nature of magnetic ground state of ETO, magnetization (M) is plotted in Fig. 3.1(a) as a function of H for few representative temperatures across the magnetic ordering temperature T_N. Below T_N, M increases almost linearly with increasing H but above a critical field $H_C=$ 1.2 T, it starts to saturate. The value of saturated magnetic moment (M_S) is 7 μ_B/Eu at 2 K and 7 T which is in good agreement with the theoretically estimated value of $M_S=g\mu_B S=7$ μ_B. This suggests that Eu^{2+} spins are fully polarised at 7 T and Heisenberg in nature which will be discussed later on. At high temperatures, well above T_N, $M(H)$ becomes almost linear [80].

Magnetostriction, i.e., lattice deformation associated to the change in the mag-
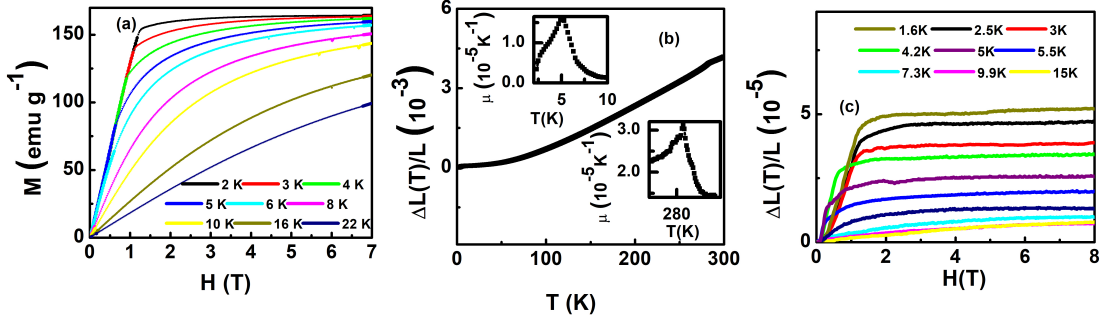
Figure 3.1: For ETO single crystal, (a) $M(H)$ in the vicinity of T_N, (b) T variation of $\Delta L/L$ at zero magnetic field. The upper and lower insets show of $\mu(T)$ at T_N and T_S respectively, and (c) H variation of $\Delta L/L$ across T_N.

netic field strength, is a tool to explore the spin-lattice coupling in the system. Here, we have studied the linear expansion of sample length [$\Delta L/L$] as functions of both T and H. In the absence of magnetic field, temperature dependence of thermal expansion $\Delta L/L_{1.5K}$=[$L(T)$-$L_{1.5K}$]/$L_{1.5K}$, where $L_{1.5K}$ is the length of the sample at T=1.5 K, is displayed in Fig. 3.1(b). Three temperature regions are distinctly manifested in this plot. With decreasing temperature, $\Delta L(T)/L$ decreases approximately linearly with T from 300 K to ~285 K and then starts to deviate in downward direction from the linear behavior and exhibits a weak anomaly at around the structural phase transition temperature 282 K. With further decrease in T, $\Delta L(T)/L$ decreases continuously and exhibits an anomaly at T_N which is similar to that observed at T_S but stronger in nature. Just below T_N, $\Delta L(T)/L$ decreases very rapidly with decreasing temperature. It is clear from the figure that $\Delta L(T)/L$ exhibits an upward curvature over a wide range of temperature below the structural transition, suggesting a superlinear T dependence of $\Delta L(T)/L$. In the AFM state, $\Delta L(T)/L$ exhibits the T dependence which is very similar to that

of magnetization of a FM system, i.e., the sublattice/staggered magnetization. The upper and lower insets of Fig. 3.1(b) show T dependence of the coefficient of thermal expansion $\mu = \frac{d(\Delta L/L_{1.5K})}{dT}$ which also reflects λ-like peaks at T_N and T_S. We have observed the field variation of $\Delta L/L_{1.5K}$ and found that magnetic field has profound influence on the T_N. On the other hand, the effect of magnetic field on $\Delta L/L$ at T_S is weak which suggests that the spin-lattice coupling is negligible at high temperature in ETO.

The field dependence of thermal expansion, i.e., the magnetostriction $\Delta L(H)/L_0$ $=[L(H)-L_0]/L_0$, where L_0 is the length of the sample in absence of field, is investigated below and above the T_N in Fig. 3.1(c). It has been observed that the magnetostriction is quite large below T_N but its value decreases rapidly with increasing temperature. However, the nature of field dependence of magnetostriction is very sensitive to the temperature and applied field. The effect is large at low temperatures. At 1.8 K, $\Delta L(H)/L_0$ reaches as high as 5.2×10^{-5}. Two very distinct regimes are found. At temperatures below T_N, $\Delta L/L_0$ is very small and negative for the applied field below 0.2 T. Above 0.2 T, $\Delta L/L_0$ initially increases slowly and then rapidly up to a critical value of applied field (H_C). Above H_C, $\Delta L/L_0$ increases very slowly and a saturation like behavior appears in the high field region. One can see a striking similarity between the nature of $M(H)$ and $\Delta L(H)/L_0$.

Thermal variation of specific heat (C_p) at constant pressure is plotted in Fig. 3.2(a). C_p at zero field decreases down to 10 K with decreasing temperature and then increases rapidly and exhibits a very sharp λ-like peak close to $T_N = 5.75$

K. The structural transition in ETO is visible as an anomaly also in the $C_p(T)$ at $T_S = 281$ K, the expanded view of which is displayed in the inset of Fig. 3.2(a). To determine the lattice contribution of the specific heat of the system, the zero-field C_p was fitted well with the combined Debye plus Einstein model in the temperature range 20-200 K. It is clearly visible from the figure that with the application of field, above 2 T, the magnetic transition region broadens and the peak shifts progressively towards higher temperature [80, 81]. Whereas, the field dependence of the anomaly at T_S in C_p is hardly detectable.
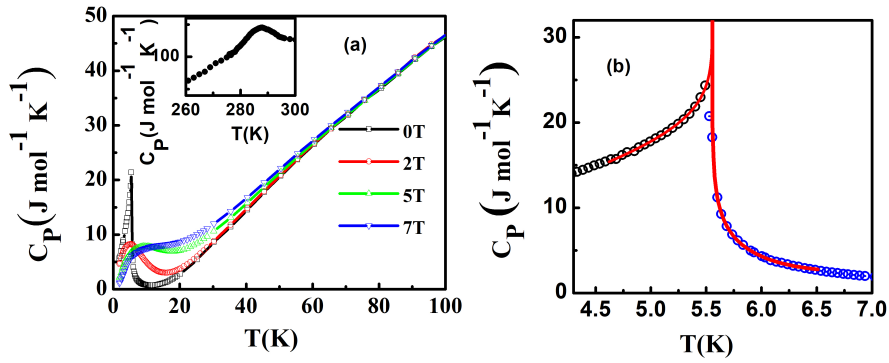
Figure 3.2: (a) H variation of C_p(T) at different magnetic fields. The inset shows the broad view of anomaly at T_S. (b) Critical analysis of the magnetic phase transition at T_N from $C_p(T)$. The solid line is the fitting of eq.(3.1) to C_p.

In contrast to the sharp peak at T_N of the heat capacity data, the low temperature thermal expansion data are broad. Also, as heat capacity measurement is much more sensitive at low temperature, therefore, it has been considered for critical study. In order to investigate the critical behavior of ETO single crystal in detail, the experimentally observed C_p curve in the vicinity of T_N has been fitted

to the well known eq. (3.1) which is shown in Fig. 3.2(b) [82, 83].

$$C_p^* = (A_\pm)|T - T_N|^{-\alpha} + B_\pm + D(T - T_N) \tag{3.1}$$

where the subscripts + and - stand for $T > T_N$ and $T < T_N$ respectively. Here, $t = (T - T_N)$, and α, A, B and D are adjustable parameters. The linear term represents the background contribution to the specific heat. The experimental data have been simultaneously fitted for the region $T > T_N$ and $T < T_N$ with a nonlinear least square routine using a Levenberg-Marquardt method [83]. We have selected a fitting range by keeping T_N as constant. We have done a first adjustment with the set of parameters without correcting the scaling term. To minimize the error, we have tried to enhance the data points by changing t_{min} and t_{max}. Then it has been followed by the correction of scaling term to get better fitting. Finally, we have made T_N as a free parameter to confirm the fitting. During the overall process, our main focus was on the root mean square value (R) as well as the deviation of the fitted curve from the actually measured one. The fitted result is shown in Fig. 3.2(b) as a smooth red colored curve. The fitting shows that the value of R is very close to 1. The deduced values of the critical exponent (α) and amplitude ratio (A_+/A_-) are -0.081 and 1.56, respectively, which are found to be close to that predicted by 3D-Heisenberg model as mentioned earlier in Table 1.1. ETO is spherically symmetric as Eu^{2+} has L=0, J=S= 7/2. Therefore, due to having isotropic g factor, one expects antiferromagnetic ETO as a classical 3D-Heisenberg system.

3.4   Conclusions

The critical analysis has been done for the low temperature magnetic transition temperature of EuTiO$_3$ by high-resolution heat capacity measurement. At low temperature transition region, the value of the critical exponent α is -0.081 and the value of A_+/A_- is 1.56. These values indicate that the material belongs to a 3D-Heisenberg system.

4

Unconventional transport properties of the itinerant ferromagnets EuTi$_{1-x}$Nb$_x$O$_3$ (x=0.10−0.20)

4.1 Introduction

The interplay between magnetism and charge conduction in strongly correlated systems results in several intriguing physical phenomena such as large negative magnetoresistance (MR), anomalous Hall effect, quantum phase transition, non-Fermi-liquid (NFL) behavior, Kondo effect, etc. [84, 85, 86, 87, 88, 89]. Hence, it is immediately in an urge of exploring new correlated itinerant ferromagnet as well as its magnetic and transport properties. Metallic ferromagnets can be divided into two broad categories depending on transport properties: i) good metallic ferromagnets such as iron, nickel, and cobalt, which can be well explained by Landau's Fermi-liquid theory [90] and ii) 'bad metallic' ferromagnets such as heavy fermion com-

pounds, rare-earth transition metal oxides, etc. [84, 91, 92, 93, 94, 95, 96, 97, 98]. In case of the so-called bad metals, often the Fermi liquid theory fails due to strong electronic correlation. The well known itinerant ferromagnets $SrRuO_3$ and $ZrZn_2$ neither can be classified as good metallic ferromagnet nor can be compared with $3d$ transition metal oxides like manganites [84, 99, 100].

As mentioned earlier, the next-to-nearest neighbor FM interaction is slightly larger than the nearest-neighbor AFM interaction between Eu^{2+} ions in ETO. Therefore, the ground state of ETO is an unstable AFM which can be easily transformed to the other by chemical doping on A or B site. There are a number of studies on the Eu^{2+} site substitution of ETO. The introduction of electron into the Ti $3d$ orbital via the substitution of R^{3+} ion at the Eu^{2+} site transforms ETO into a FM metal [59, 101]. The temperature dependence of resistivity (ρ) for $Eu_{1-x}La_xTiO_3$ (ELTO) with $x=0.10$ resembles that of 10% La-doped $SrTiO_3$, except at low temperature [101, 102]. For $Sr_{0.9}La_{0.1}TiO_3$ (SLTO), ρ decreases smoothly down to very low temperature without displaying any anomaly while a sharp drop in ρ is observed just below the FM transition (T_C) in ELTO. Most importantly, ELTO exhibits a weak upturn in ρ below $\sim$30 K [101, 102]. Another important candidate is obtained by doping Nb^{4+} ($4d^1$) ion on the Ti^{4+} ($3d^0$) site in ETO without interrupting the magnetic chains of Eu^{2+} moments. A remarkable increase in electrical conductivity is observed in $EuTi_{1-x}Nb_xO_3$ (ETNO) with increasing the Nb concentration (x) [103, 104, 105, 106]. Unlike ELTO, the substitution is done at B-site for ETNO and it becomes metallic and FM over a much wider range of Nb doping ($0.05 < x \leq 1$) [105, 106]. In ABO_3-type perovskite materials, the insulator to metal transition through B site substitution is infrequent.

Usually, B-site substitution causes disorder which enhances carrier localization. Despite some minor differences, the nature of magnetic and transport properties in ELTO and ETNO are almost similar. Remarkably, a weak rise in ρ is also observed in ETNO below 30 K [105]. Though ρ decreases with decreasing temperature for both ELTO and ETNO, it is quite unexpected that the charge conduction mechanism in these two systems will be same as that in SLTO. Due to the presence of large localized moments, there may have strong correlation between the $4d^1$ itinerant charge carrier and the spin ($S=7/2$) of Eu^{2+}.

In order to understand the mechanism of charge conduction in ETNO, a comprehensive study of transport properties is performed on high quality single-crystalline samples with $x=0.10$, 0.15 and 0.20. The temperature and magnetic field dependence of resistivity is analyzed in details. The observed results are then compared with different classes of FM metals mentioned above. Indeed, our detailed analysis of resistivity reveals the presence of several scattering mechanisms. With the increase in temperature, charge conduction mechanism crosses over from electron-magnon to spin-disordering to Kondo to electron-electron scattering to an unusual $T^{3/2}$ dependence of resistivity due to non-Fermi liquid behavior.

4.2 Sample preparation and experimental details

Polycrystalline ETNO ($x=0.10-0.20$) powder samples were prepared by the standard solid-state reaction method. Stoichiometric mixtures of Eu_2O_3 (pre-heated), Nb_2O_5 and TiO_2 were heated at $1000-1100\,^0C$ for two days in a reduced atmosphere containing 5% H_2 and 95% argon followed by intermediate grindings. The

obtained powder was pressed into two cylindrical rods which were finally sintered at $1100\,^0$C in the same environment. The single crystals of ETNO (x=0.10−0.20) were grown by floating-zone technique in reduced atmosphere (5% H$_2$ and 95%) using four-mirror optical floating zone furnace. The phase purity of ETNO (x=0.10−0.20) was checked by powder XRD method using a high-resolution Rigaku diffractometer (TTRAX III). The absence of any impurity peak in the XRD patterns of the powdered-crystals, which are shown in Fig. 4.1, confirms the single phase nature of the compounds. The structural analysis was done by the Rietveld refinement method using FULLPROF.
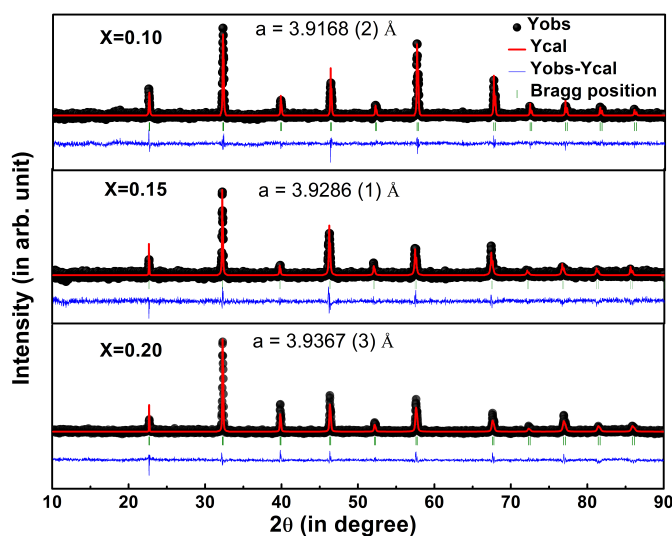
Figure 4.1: X-ray powder diffraction patterns for ETNO crystals at room temperature. The solid red lines indicate the Rietveld refinements of the diffraction patterns.

The reflections in XRD patterns were indexed using the cubic $Pm3m$ space group and Fig. 4.1 shows that the lattice parameters increases linearly with increasing Nb concentration x. The estimated lattice parameters are a= 3.9168(2) Å, 3.9286(1) Å, and 3.9367(3) Å respectively for x= 0.10, 0.15, and 0.20, which are

found to be comparable with that reported earlier [105]. The valency of Nb can be either 4+ or 5+. Here, as the samples were grown under the reduced atmosphere, Nb is likely to be in 4+ state. In this context, it is to be mentioned that in $EuTiO_3$, Ti can be replaced by Nb up to 100 %. In both of the end members of this series, i.e., $EuTiO_3$ and $EuNbO_3$, Eu is divalent which implies that Nb is in tetravalent state. The experimentally estimated value of carrier density $\sim 2 \times 10^{21}$ cm^{-3} from Hall measurements at 3 K further supports the 4+ state of Nb ion. The temperature and field dependence of the dc magnetization and heat capacity measurements were performed in a PPMS. Resistivity was measured by a standard four-probe technique where the electrical contacts were made using highly conducting silver paint.

4.3   Results and discussions

The thermal variation of dc magnetic susceptibility ($\chi = M/H$) and specific heat for the studied ETNO (x=0.10$-$0.20) single crystals are shown respectively in Figs. 4.2(a) and (b). The temperature dependence of the zero-field-cooled (ZFC) magnetization and the λ-like heat capacity anomalies show that these samples undergo a continuous phase transition from paramagnetic to ferromagnetic state at Curie temperatures T_C= 8, 9.5 and 6 K for x=0.10, 0.15 and 0.20 respectively. No anomaly other than that at T_C is observed either in magnetization or in heat capacity. It says that unlike polycrystalline samples [105], the studied crystals are chemically homogeneous, AFM and FM phases do not coexist in the studied compositions. T_C increases rapidly with increasing Nb concentration x, becomes maximum around 0.15 and then decreases with further increasing x, as can be seen

in Fig. 4.2(c). This variation of T_C with doping concentration x is qualitatively similar to ELTO, although the maximum T_C is 1.5 K higher in ETNO [102].
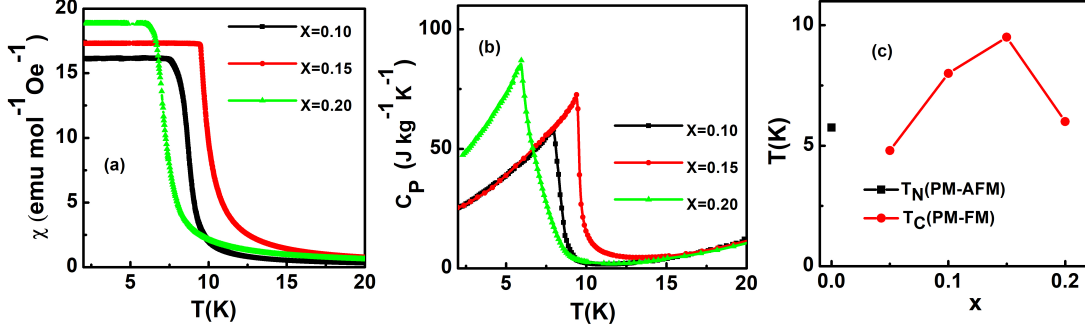
Figure 4.2: For ETNO single crystals, (a) $\chi(T)$ at 50 Oe, (b) temperature variation of C_p at low T, and (c) dependence of T_N and T_C on Nb doping concentration x.

For understanding the correlation between magnetism and transport, the magnetic excitation spectrum has been investigated below T_C. For this, we have estimated the spontaneous magnetization (M_S) from the Arrott plots with field up to 7 T. The T dependence of M_S is displayed in Fig. 4.3(a) for the $x=0.15$ sample as a representative. Well below T_C, where the critical fluctuation is absent, the temperature variation of M_S can be described by the Bloch's $T^{3/2}$ law [20], which is discussed earlier in section 1.3,

$$[M_S(0) - M_S(T)]/M_S(0) = \Delta M_S/M_S(0) = DT^{3/2}, \tag{4.1}$$

where D is the spin-wave parameter. For simple cubic lattice, the coefficient D can be calculated from the relation $D=(0.0587/S)(k_B/2JS)^{1.5}$, where J is the exchange coupling between two neighboring Eu^{2+} spins. $M_S(T)$ obeys the Bloch's $T^{3/2}$ law at low temperature $T<4$ K which is clearly visible in Fig. 4.3(b). From the
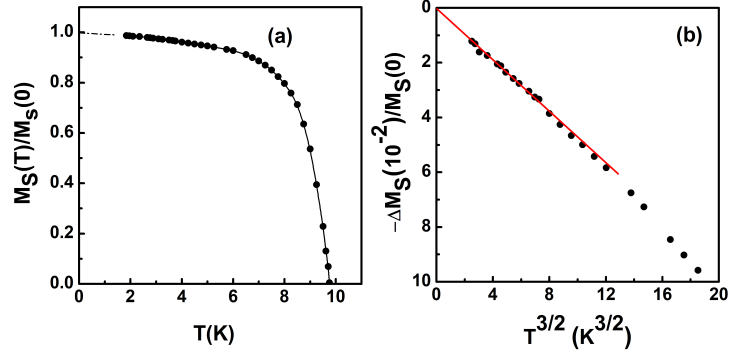
Figure 4.3: For $x = 0.15$ crystal, (a) $M_S(T)$ normalized at T=0 K, (b) $T^{3/2}$ dependence of ΔM_S below T_C. Solid line is the fit to Bloch's law.

slope of the linear fit to the data, we get D=50(1)$\times10^{-3}$ K$^{-3/2}$ and the value of exchange interaction is evaluated to be 0.320(4) k_B K. In this context, we would like to mention that the above value of J estimated from the Bloch's $T^{3/2}$ law is comparable to that predicted by the molecular field theory [20], J=$3k_BT_C/2ZS(S+1)$=0.15 k_B K, where Z is the number of nearest neighbor spins. The value of Z is taken as 6 for a simple cubic perovskite structure.

Figure 4.4(a) illustrates the temperature dependence of resistivity for three ETNO single crystals. For all three compounds, in the whole temperature range, ρ exhibits metallic behavior (dρ/dT>0), except in a narrow region just above T_C, where a weak upturn in ρ is observed with decreasing T. Paramagnetic to ferromagnetic transition is also reflected in $\rho(T)$ curves. As a result of suppression of spin-disorder scattering, ρ abruptly drops just below T_C. With decreasing T, ρ decreases at a much faster rate in FM state as compared to that in PM state. Though the qualitative nature of $\rho(T)$ curve is similar to that reported earlier on polycrystalline samples, for a particular value of Nb content, the absolute value of ρ is smaller and the residual resistivity ratio $\rho(300 \text{ K})/\rho(2 \text{ K})$ is much larger

in case of single crystals. For example, the values of $\rho(2$ K$)$ and $\rho(300$ K$)/\rho(2$ K$)$ are 150 $\mu\Omega$ cm and 1.5 respectively for polycrystalline sample [105] while the corresponding values are 12 $\mu\Omega$ cm and 8 for the single crystal, with x=0.20. The reason behind the larger value of ρ at low T in polycrystalline samples is the strong grain boundary scattering.
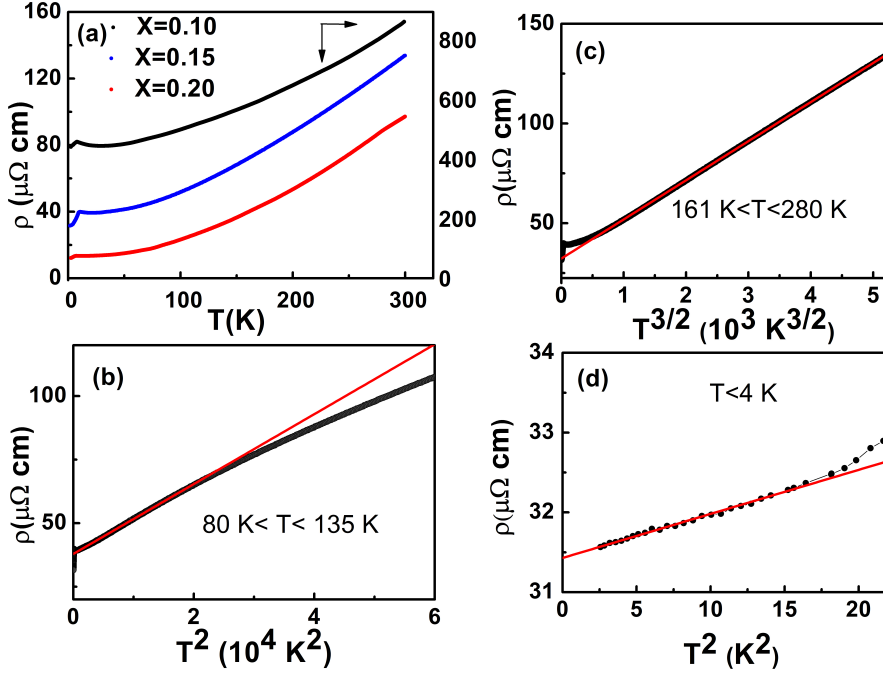
Figure 4.4: (a) $\rho(T)$ for all the three ETNO crystals. For x=0.15 crystal, (b) T^2 dependence of ρ in the PM region, (c) $T^{3/2}$ variation of ρ in the PM region, and (d) T^2 fitting to ρ in the FM region.

It is evident that $\rho(T)$ curve cannot be fitted with a single power-law expression over the entire temperature range in the PM state, because before ρ starts to increase, just above T_C, a strong upward curvature develops. To understand the complicated nature of $\rho(T)$ curve, the role of different scattering mechanisms on charge conduction has been analyzed thoroughly. In the PM state, ρ shows a

quadratic T behavior, $\rho = \rho_{a0} + aT^2$, in a narrow range above the minimum which crosses to $\rho = \rho_{b0} + bT^{3/2}$ dependence over a wider range and up to temperature as high as 280 K. The observed dependence of ρ is shown in Figs. 4.4(b) and (c) for $x=0.15$ as a representative. We have also analyzed the temperature dependence of ρ for $x=0.10$ and 0.20 compounds, as shown in Fig. 4.5 and Fig. 4.6 respectively. Similar to $EuTi_{0.85}Nb_{0.15}O_3$, the resistivity for both of the compounds obeys different power law of temperature for different temperature regimes. They also exhibit T^2 and $T^{3/2}$ behaviors in the PM region above T_C.
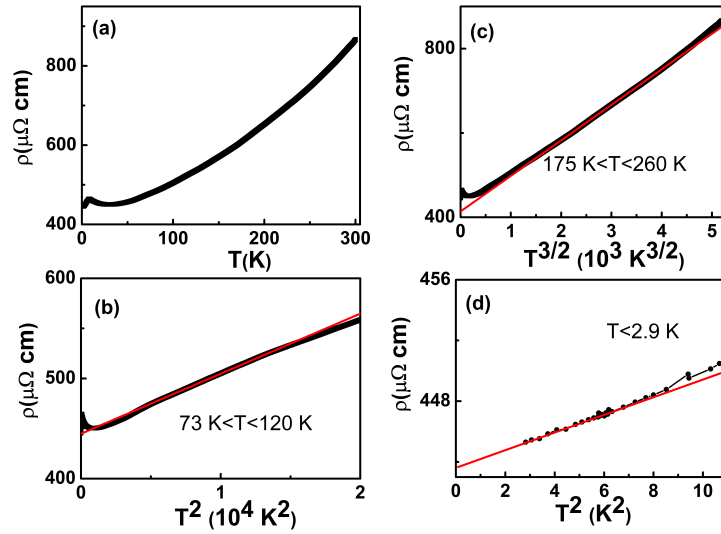
Figure 4.5: For $x=0.10$ crystal, (a) T dependence of the resistivity over the whole temperature range, (b) T^2 dependence of resistivity in the PM region in the temperature range between 73 K to 120 K, (c) $T^{3/2}$ variation of resistivity in the temperature range of 175 K $< T <$ 260 K above T_C, and (d) T^2 fitting into the resistivity at very low temperature in the FM region below 2.9 K.

The deduced values of a and b in the PM state are listed in Table 4.1 for all three compounds. The T^2 behavior of ρ is a sign of electronic correlation which is consistent with the formation of Fermi-liquid. a is a measure of the quasiparticle-quasiparticle scattering rate which decreases rapidly with increasing the doping
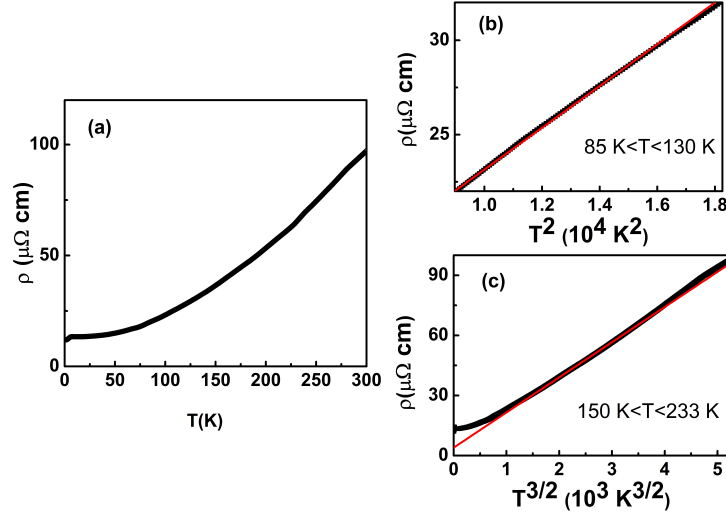
Figure 4.6: For x=0.20 crystal, (a) T dependence of the resistivity over the whole temperature range, (b) T^2 dependence of resistivity in the temperature range of 85 K $< T <$ 130 K above T_C, and (c) $T^{3/2}$ variation of resistivity in the temperature range of 150 K $< T <$ 233 K above T_C.

concentration. Often, metallic oxides are called 'bad metals' due to their strong electron-electron interaction. The deduced value of a for x=0.20 is about an order of magnitude smaller than that for the well known itinerant FM SrRuO$_3$ but two orders of magnitude larger than that for the elemental FMs such as Fe, Co, Ni [98].

It is noteworthy that ρ in several FM perovskites shows T^2 dependence well below T_C. Similarly, in present compound ETNO, ρ also exhibits T^2 dependence well below T_C as displayed in Fig. 4.4(d) for x=0.15. In contrast to the observed T^2 behavior in the PM state, T^2 behavior of ρ in the FM state yields unusually large value of a, approximately more than one order of magnitude larger than that in PM state. Such a huge difference between the values of the co-efficient a in PM and FM states suggests that the T^2 dependence of ρ in the FM state causes due to the dominant magnetic scattering over the electron-electron scattering.

Table 4.1: Estimated values of the resistivity coefficient a in units of $\mu\Omega$ cm/K^2 in the FM ($T < T_C$) and PM ($T > T_C$) states and the resistivity coefficient b in units of $\mu\Omega$ cm/K$^{3/2}$ in the PM state ($T > T_C$) for ETNO single crystals with x=0.10, 0.15, and 0.20. For x=0.20, the accurate determination of the parameter a below T_C is not possible due to its low transition temperature.

x	a ($T < T_C$)	Range of T	a ($T > T_C$)	Range of T	b ($T > T_C$)	Range of T
0.10	$26.9(1) \times 10^{-2}$	T<2.9 K	$6.0(1) \times 10^{-3}$	73< T <120 K	$8.4(1) \times 10^{-2}$	175< T <260 K
0.15	$5.5(5) \times 10^{-2}$	T <4 K	$1.4(1) \times 10^{-3}$	80< T <135 K	$2.0(1) \times 10^{-2}$	161< T <280 K
0.20			$1.1(1) \times 10^{-3}$	85< T <130 K	$1.7(1) \times 10^{-2}$	150< T <233 K

Similar T^2 dependence of resistivity is also observed in Fig. 4.5(d) for x=0.10 compound, but we cannot fit the resistivity of the $x = 0.20$ compound with T^2 over a reasonable interval of T below T_C for an exact determination of a due to having lower T_C. Normally in ferromagnets, ρ shows T^2 behavior because of the electron-magnon scattering. As both electron-electron and electron-magnon scattering occur at low temperature, therefore, it is very difficult to separate their relative contributions in resistivity for the FM materials with high T_C. Even in elemental ferromagnets, where the electronic correlation is believed to be very weak, the origin of T^2 behavior of ρ at low temperature is not yet settled [107]. Due to the much lower T_C of the studied system, we have been able to detect both the scatterings in two different temperature regions.

Usually, resistivity of a metal exhibits linear T dependence at high temperatures due to the electron-phonon scattering. It is quite unusual to observe a crossover of $\rho(T)$ from T^2 to $T^{3/2}$ at high temperatures. To check that, a very sluggish crossover from T^2 to T dependence does not result in $T^{3/2}$ dependence of ρ, a theoretical fit to the observed $\rho(T)$ can be performed using BG expression mentioned in eq.(1.25) and the residual resistivity term ρ_0. Several attempts have been made to fit the

resistivity above the minima and found that neither the BG expression with ρ_0 nor the addition of an extra term aT^n to eq.(1.25) reproduces the experimental data. However, a better fit to the $\rho(T)$ curve is obtained at high temperatures for $n=3/2$ as can be seen in Fig. 4.7 for $x=0.20$. Figure 4.7 also shows that the contribution of $T^{3/2}$ is more significant than that of the BG expression which indicates that $T^{3/2}$ dependence dominates the charge conduction mechanism in the present system over the electron-phonon scattering. This is also clearly visible from Figs. 4.5(c) and 4.6(c) in which a weak upward deviation from $T^{3/2}$ dependence is observed at high temperatures.
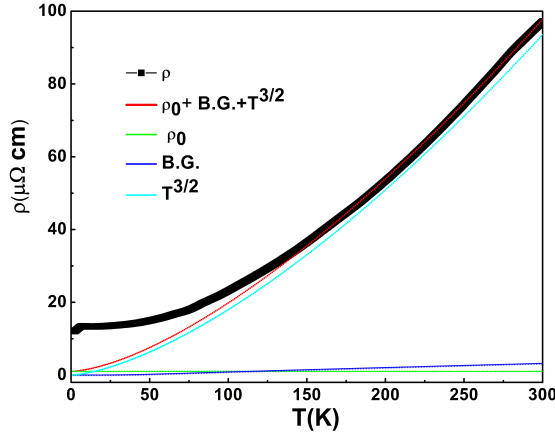
Figure 4.7: For an $x=0.20$ crystal, a theoretical fit to the observed $\rho(T)$ using the Bloch-Grüneisen expression [eq. (1.25)] with ρ_0 and $bT^{3/2}$ in the PM region (red line).

In itinerant systems, usually the departure from T^2 dependence of the resistivity at low temperature is one of the hallmarks of NFL behavior. There exist ample experimental evidences of NFL behavior in heavy fermions such as unusual temperature dependence of the resistivity, heat capacity, magnetic susceptibility, etc. [108]. These behaviors have been observed in the vicinity of quantum critical point where the quantum critical dynamics plays an important role. However, generic

NFL behavior of the resistivity has been found in some itinerant magnets with ferromagnetic, helical, or skymionic order both near and away from the magnetic transition and very recently its origin has been investigated theoretically that rules out the possible influence of quantum critical behavior [109]. Therefore, contrary to the heavy-fermion systems, in many oxides [98, 110, 111] such as $SrRuO_3$ and the present system, no such hallmarks of the NFL behavior have been detected in the specific heat and magnetic susceptibility. This generic NFL behavior is still very challenging to explain. In this regard, below we draw a comparison of our results with the observed $T^{3/2}$ or $T^{5/3}$ dependence of the resistivity away from the magnetic transitions, reported in some oxides and intermetallic itinerant systems.

It has been assumed that resistivity in a weakly and nearly FM metal exhibits T^2 behavior at $T \ll T_C$ and $T^{5/3}$ dependence in the vicinity of T_C [112, 113]. This behavior is noticed in weak itinerant ferromagnets $Ni_{75\pm x}Al_{25\pm x}$ [114]. $T^{3/2}$ dependence of ρ in a three-dimensional AFM system, is observed near the AFM transition due to the spin fluctuations. The $T^{3/2}$ dependence of ρ well below the transition temperature is found in Pd-based dilute alloys such as PdFe, PdMn (with few % of Fe or Mn) due to the incoherent part of electron-magnon scattering [115]. Hence, in our present system ETNO, the $T^{3/2}$ behavior of ρ far away from the FM transition, cannot be explained in terms of incoherent electron-magnon scattering.

Currently, the transport properties of another strongly correlated system with single valance Ni^{3+}, $R NiO_3$ are of great interest [92, 93, 116]. In single crystals of $PrNiO_3$ under high pressure, ρ shows T^n (n=1.33 and 1.6) dependence whereas ρ

is extremely sensitive to lattice strain in ultrathin epitaxial film of $NdNiO_3$ and for highly compressive strained-films, ρ follows $T^{5/3}$ behavior at high temperatures [92, 93]. In itinerant ferromagnet Ni_xPd_{1-x}, $\rho(T)$ exhibits $T^{5/3}$ dependence up to temperature as high as 150 K [108]. However, ρ in Nd-doped $LaNiO_3$ follows $T^{3/2}$ behavior [116]. At high pressure, $T^{3/2}$ dependence of ρ has also been found in well known skyrmion lattice MnSi [95, 96]. The departure from T^2 dependence of ρ in these systems has been described as the non-Fermi liquid state. The $T^{3/2}$ behavior of ρ is also observed in single crystal and thin films of itinerant ferromagnet $SrRuO_3$ [98, 111]. In $SrRuO_3$, ρ exhibits T^2 dependence far below T_C ($\sim$160 K) and it passes through $T^{3/2}$ dependence with increasing temperature. Like ETNO, $T^{3/2}$ behavior is observed at high temperature over a wide range. In $SrRuO_3$, this crossover from T^2 to $T^{3/2}$ dependence of ρ is interpreted as the NFL transition [111]. The values of the coefficient b determined from the slope of ρ vs $T^{3/2}$ plot are comparable to that reported for the $SrRuO_3$ [111]. The exponent n is found to be sensitive to the underlying phenomena giving rise to the critical fluctuations associated with NFL behavior. The widely observed critical exponent 3/2 indicates finite wavevector fluctuations [92].

It has been already mentioned that $\rho(T)$ curve for all the three ETNO compounds exhibits a broad minimum at $T_{\min}$ in the PM state [Fig. 4.4(a)]. In the temperature window $T_C < T < T_{min}$, $\rho(T)$ follows $\log(T)$ dependence as shown in Figs. 4.8(a) and (b). The influence of magnetic field on the $\log(T)$ dependence of ρ is also observed in Figs. 4.8(a) and (b) for x=0.10 and 0.15, respectively. For x=0.20, the increase of ρ below T_{min} is very less and hence, the fit is insensitive. Figures 4.8(a) and (b) show that ρ decreases rapidly with increasing the magnetic
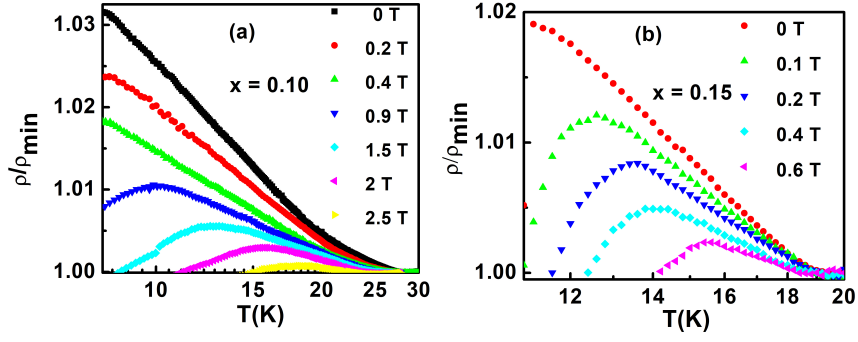
Figure 4.8: The $log(T)$ dependence of ρ in the range $T_C<T<T_{min}$ at different magnetic fields for the (b) $x=0.10$ and (c) $x=0.15$ crystals.

field strength, the resistivity minimum shifts toward lower temperature and also the range of $\log(T)$ dependence shrinks progressively. This clearly suggests that the upturn in ρ below T_{min} is attributed to the Kondo scattering of the itinerant electrons by the localized Eu^{2+} spins.

It has been suggested that the ferromagnetism occurs in ELTO and ETNO due to the RKKY interaction between the localized $4f$ spins of Eu^{2+}, mediated by the itinerant d electrons of Ti or Nb [101, 102, 105]. Thus, the competition between the intersite RKKY interaction, $E_{RKKY}=J^2\eta$, where η is the density of states of the conduction sea, and the Kondo temperature, $T_K{\sim}D_W e^{-1/(2J\eta)}$, where D_W is the bandwidth, leads to the formation of either the usual magnetic ordering state with large moments viz., in rare-earth elements or the non-magnetic Kondo state with suppressed moments as discussed before in section 1.4.3 [117, 118]. For small $J\eta$, $E_{RKKY}{\gg}T_K$, the RKKY-type FM exchange dominates over the Kondo state which stabilizes the usual magnetic ordering with full moment of Eu^{2+} below T_C in ETNO and ELTO. The sign and strength of RKKY exchange interaction ($J_{RKKY}{\sim}\cos(2k_F r)/r^3$) are the functions of the spatial separation (r) of the local-

ized moments (Eu^{2+}) and the Fermi wave vector k_F. As k_F and r depend on the Nb concentration, the two energy scales are varying with increasing x. The deduced lattice parameter a for different doping level x mentioned in Fig. 4.1 shows that the spatial separation between the Eu^{2+} moments increases almost linearly with the increase in x. In Fig. 4.2 (c), the transition temperatures (T_N or T_C) vary with the doping concentration x like an oscillatory function, i.e., the exchange interaction changes its sign with increasing x and thereby consistent with the RKKY picture. The suppression of Kondo scattering by FM RKKY exchange is largest at around x=0.15 and that's why T_C peaks at x=0.15. Similar behavior has also been found in La- and Gd-doped $EuTiO_3$ crystals which is described as RKKY oscillation [101]. The low temperature and high field favor the FM phase and forbid the Kondo singlets formation, thereby the temperature range of $\log(T)$ dependence shrinks as the FM phase intrudes into the high-T phase with increasing the applied field. Therefore, $\rho(T)$ of the present ETNO system behaves like a FM Kondo lattice which is relatively less numerous and shows rather complicated physical pictures [117, 118, 119]. Generally, Kondo effect is strongly suppressed in systems with large local moments. Several rare-earth based AFM systems with RKKY interaction show a minimum in $\rho(T)$ which cannot be described by the Kondo scattering but attributed to the formation of liquid-like spin state [120, 121, 122, 123]. In this context, we would like to mention that few Eu- and Sm-based compounds also exhibit Kondo effect but they are antiferromagnetically ordered [124, 125, 126].

In order to investigate the effect of the FM ordering of Eu^{2+} moments on charge scattering, we have measured the temperature dependence of the resistivity for different applied magnetic fields H up to 9 T across the T_C as shown in Fig.
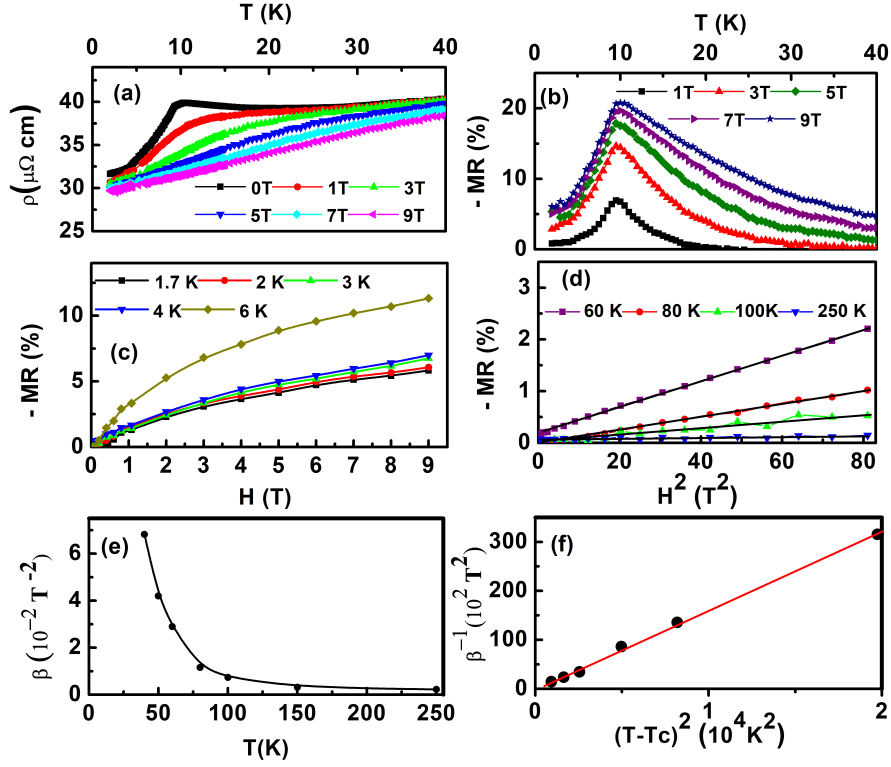
Figure 4.9: For the $EuTi_{0.85}Nb_{0.15}O_3$ crystal, (a) $\rho(T)$ for different magnetic fields, (b) MR versus H below T_C, (c) H^2 dependence of the MR well above T_C. Solid black lines correspond to a linear fit, (e) β versus T plot, and (f) linear fitting of β^{-1} versus $(T - T_C)^2$ in the paramagnetic region well above T_C.

4.9(a) for the x=0.15 compound as a representative. The sharp anomaly at T_C in $\rho(T)$ curve weakens with increasing the magnetic field and disappears above a critical field and ρ exhibits metallic behavior over the entire temperature range. This indicates that the conduction of itinerant electrons is strongly coupled with localized Eu^{2+} spins and can be controlled by aligning the localized spins with magnetic field, and such a process gives rise to large negative magnetoresistance (MR)= $\Delta\rho/\rho$=[$(\rho(H) - \rho(0))/\rho(0)$] where $\rho(H)$ is the resistivity at a field H. Figure 4.9(b) shows the temperature dependence of MR. Except in the vicinity of T_C, $\Delta\rho/\rho$ is small and decreases rapidly on the both sides of the peak. The

maximum value of $\Delta\rho/\rho$ at 9 T is estimated to be about 21 %. Both the field and temperature dependence of MR of ETNO and its value are same as that reported for ELTO [101]. We have also calculated $\Delta\rho/\rho$ in both electron-magnon and electron-electron scattering dominated regions. Well below T_C, where the contribution of electron-magnon scattering in ρ is significantly larger, $\Delta\rho(H)/\rho$ increases rapidly with field and then tends to saturate at high field as displayed in Fig. 4.9(c) for some representative temperatures. The qualitative nature of $\Delta\rho(H)/\rho$ is similar to the $M(H)$ curve and to that estimated theoretically for spin-wave scattering [113]. Also, $\Delta\rho/\rho$ approximately scales with the magnetization offset $\Delta M_{\mathrm{S}}/M_{\mathrm{S}}(0)$ at low temperature where ρ starts to saturate with field. These findings support spin wave scattering. In contrast, well above T_C, the nature of $\Delta\rho(H)/\rho$ curves in Fig. 4.9(d) is very different. $\Delta\rho/\rho$ is quite small and shows H^2 dependence. The origin of MR in the PM state well above the T_{C} can be understood from the relation of MR with the isothermal magnetization $M(H)$ as observed in several perovskite FMs, i.e.,

$$MR = -C[M(H)/M_{max}]^2, \tag{4.2}$$

where C is a constant and M_{max} is the magnetization at the lowest temperature in presence of magnetic field H [21]. Therefore, $MR \propto M^2$. This relation comes into play as the carriers get scattered by the thermally fluctuating spins. From eq. (4.2) and $M=\chi H$ relation, it can be shown that $MR=-\beta H^2$. According to the Curie-Weiss law of paramagnetism, χ is proportional to $1/(T-T_{\mathrm{C}})$ in the PM region well above T_{C}. Therefore, $\beta \propto 1/(T-T_{\mathrm{C}})^2$. Here, the H^2 dependence of negative MR holds only at low fields as can be seen in Fig. 4.9(d). β versus T and β^{-1} versus $(T-T_{\mathrm{C}})^2$ are plotted in Figs. 4.9(e) and (f), respectively. The linear

fitting of β^{-1} indicates that MR originates from the local spin fluctuations.

When Eu^{2+} is substituted by La^{3+} or Gd^{3+}, electrons are entered in $3d$ t_{2g} orbitals of Ti which lead to mixed valence Ti^{3+} and Ti^{4+} and the metallic conductivity appears because of the hopping of electrons from $3d^1$ to $3d^0$. Usually, in ABO_3 perovskites, doping at A site by some heterovalent element transfers either hole or electron from A to transition metal B and the system transforms to a metal above a critical doping level. Whereas, insulator to metal transition through B-site substitution is rare as the doping at this site creates disordering which supports localization effect. Thus, insulator to metal transition with a small amount of Nb ($\sim$5%) doping at Ti site indicates that charge conduction is not due to the percolation through Nb ions. The unpaired $4d^1$ electron of Nb hops to the empty $3d^0$ orbital of Ti and as a result, $4d$ state of Nb^{4+} strongly hybridizes with $3d$ of Ti^{4+}. At higher doping level of x nearly 1, Nb is surrounded by other Nb ions, and in such case conductivity is dominated by the hopping of electrons between isovalent Nb ions and makes $EuNbO_3$ system metallic. Unlike $EuNbO_3$, the end members of $EuTiO_3$ are Mott insulators when substitution is done at Eu site with other rare earth ion.

The charge conduction mechanism in strongly correlated transition metal oxides is quite different from that in good elemental metals, and heavy fermions. Several non-magnetic metallic oxides such as $La_{1-x}Sr_xTiO_3$ (LSTO), $LaNiO_3$ (LNO), $SrVO_3$ (SVO), $CaVO_3$ (CVO), $SrTi_{1-x}Nb_xO_3$ (STNO), etc. with perovskite structure similar to ETNO show T^2 behavior of ρ due to electron-electron scattering [84, 93, 127]. T^2 dependence of ρ in these systems is strong and extends over a

wide range. For example, ρ shows T^2 dependence up to as high as 300 K for LSTO, CVO and SVO [84]. In $Nd_{2-x}Ce_xCuO_4$, ρ shows T^2 behavior up to about 700 K and then crosses over to T dependence [128]. This indicates that electron-phonon scattering in these systems is very weak as compared to electron-electron scattering. In ETNO also, the electron-phonon scattering is very weak and appears at high temperatures. Moreover, the value of the coefficient a for the above mentioned compounds is found to be very close to that for ETNO ($\sim 10^{-3}$ $\mu\Omega$ cm K^{-2}) in PM state at their equivalent carrier density ($\sim 2 \times 10^{21}$ cm^{-3}) [84, 129]. It is worth comparing the behavior of T dependence of ρ of ETNO with STNO because in both the cases charge carrier is doped by substituting Nb at Ti sites. a is observed to scale with carrier density over a wide range for doped $SrTiO_3$ and its value is about 10^{-3} $\mu\Omega$ cm K^{-2} at the corresponding carrier density of ETNO [84, 127]. On the other hand, the observed values of a for ETNO below 4 K do not fall on the scaling plot. This allows us to conclude that the value of the coefficient a below 4 K is too large to be electron-electron scattering for such a high carrier density. However, in these non-magnetic transition metal oxides, ρ does not exhibit any crossover from T^2 to $T^{3/2}$ dependence with increasing temperature. Thus, it can be said that the non-Fermi liquid behavior in ETNO is of magnetic origin like $SrRuO_3$.

4.4 Conclusions

We report a detailed study of the transport properties of single-crystalline $EuTi_{1-x}Nb_xO_3$ itinerant ferromagnets. The observed T^2 dependence of the resistivity in the FM state is due to the dominant electron-magnon scattering whereas that observed

in the PM state is mainly because of the electron-electron scattering. Also, the observed crossover from a T^2 to $T^{3/2}$ dependence of the resistivity in the PM state is attributed to a non-Fermi liquid behavior. Furthermore, the scattering of the itinerant electrons by the large localized moments of the Eu^{2+} ions causes a Kondo-like upturn in the resistivity above T_C. The presence of several charge scattering mechanisms and the non-Fermi liquid behavior make the present system ETNO a unique ferromagnetic metal.

5

Giant low-field magnetocaloric effect in single-crystalline $EuTi_{0.85}Nb_{0.15}O_3$

5.1 Introduction

It has been shown in Chapter 4 that 15% Nb doping at Ti site in ETO transforms the system into FM metallic one. Here, we have studied the field and temperature dependence of magnetization and heat capacity of $EuTi_{0.85}Nb_{0.15}O_3$ single crystal and calculated several magnetocaloric parameters in order to check whether this material is suitable for low-temperature magnetic refrigeration.

5.2 Sample preparation, characterization, and experimental details

Single crystals of $EuTi_{0.85}Nb_{0.15}O_3$ were grown by travelling solvent floating zone technique using a four-mirror image furnace. The details of sample preparation and characterization have been described in chapter 4. The temperature and field dependence of the dc magnetization and heat capacity measurements were carried out in a PPMS.

5.3 Results and Discussions

The high temperature linear fit to the inverse susceptibility (χ^{-1}) of ETNO (x=0.15) in Fig. 5.1(a) yields the value of θ_{CW}=8 K which is more than two times larger than that in ETO. The effective paramagnetic moment P_{eff} of ETNO is 7.9 μ_B/Eu which exactly matches to the expected value $g\sqrt{J(J+1)}\mu_B = g\sqrt{S(S+1)}\mu_B$ for $S = J = 7/2$; $g = 2$. The estimated value of P_{eff} is closed to the undoped one [80].

We have measured the variation of magnetization with magnetic field for ETNO (x=0.15) at some selective temperatures from 2 to 60 K, up to 9 T. Some representative plots of $M(H)$ are displayed in Fig. 5.1(b). Below T_C, the magnetization increases abruptly in the low-field region and tends to saturate above 0.5 T. On the contrary, $M(H)$ curve for ETO is almost linear at low-magnetic field, below 1.2 T. Also, the value of threshold field to achieve saturation is higher in ETO than that in ETNO. At 2 K and 9 T, the value of M is found to be 7.3 μ_B per formula unit in ETNO. This value of the saturation moment is slightly larger than the expected
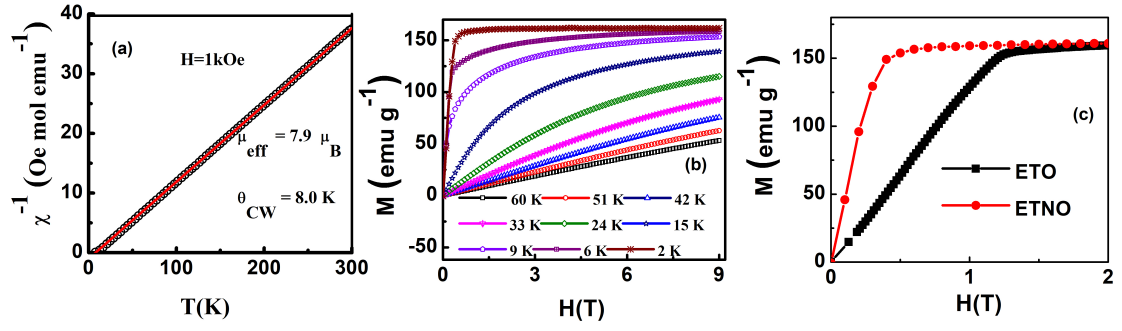
Figure 5.1: For ETNO (x=0.15) single crystal, (a) $\chi^{-1}(T)$ plot at 1 kOe. The solid line is the Curie-Weiss fit, (b) $M(H)$ curves. (c) Comparison of the nature of $M(H)$ curves of ETO and ETNO at T=2 K.

spin only moment of Eu^{2+}, indicating an extra contribution from the $4d^1$ electron of Nb^{4+}. In Fig. 5.1(c), we have shown $M(H)$ curves at low-temperature 2 K, for both ETO and ETNO, to demonstrate the difference in their nature. This plot shows significant difference in the nature of $M(H)$ curves in two systems. In the low-field regime, the slope of $M(H)$ curve (i.e., dM/dH) for ETNO is larger than that for ETO.
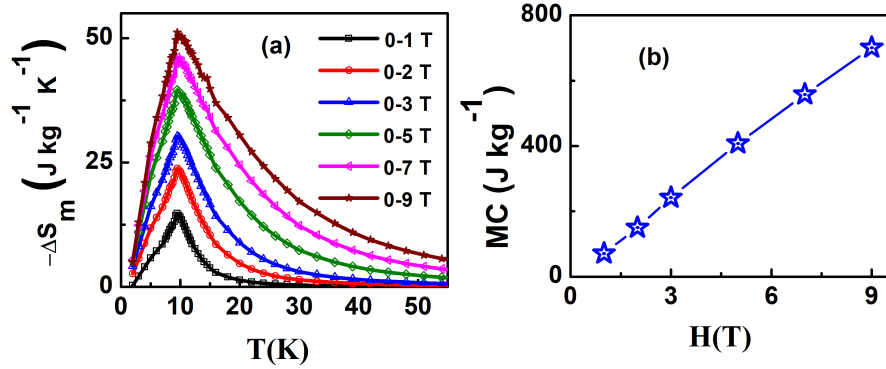
Figure 5.2: For ETNO (x=0.15) single crystal, (a) T dependence of the $-\Delta S_m$, (b) H variation of MC.

The strong variation of M with H and T suggests that ETNO (x=0.15) may

exhibit large entropy change with the application of magnetic field. The magnetic entropy change (ΔS_{m}) is calculated from the Gibb's free energy by using the eq. (1.28). The T dependence of ΔS_{m} is plotted in Fig. 5.2(a) for some selected magnetic fields from 1 to 9 T as representative. The nature of $\Delta S_{\mathrm{m}}(T)$ curve is similar to a FM system. For a given field change, ΔS_{m} decreases rapidly on both sides of T_{C}. ΔS_{m} is negative over the whole temperature range and its value increases monotonically with the increase in H. The maximum value of ΔS_{m} is as high as 51.3 J kg^{-1} K^{-1} for a field change of 9 T. The peak position is almost the same for all the $\Delta S_{\mathrm{m}}(T)$ curves corresponding to different magnetic fields. The magnetic heating/cooling capacity (MC) is calculated from eq. (1.29). Figure 5.2(b) shows the H variation of the MC. MC increases almost linearly with increasing field and attains 700 J kg^{-1} for a field change of 9 T. The observed maximum values of ΔS_{m} for the present ETNO system are 39.6 J kg^{-1} K^{-1} and 23.8 J kg^{-1} K^{-1} respectively for the magnetic field changes of 5 T and 2 T. These values are comparable with that for the antiferromagnetic ETO ($\Delta S_{\mathrm{m}}^{m}$=42.4 J kg^{-1} K^{-1} for 5 T and 23 J kg^{-1} K^{-1} for 2 T field changes), Eu$_{1-x}$Ba$_x$TiO$_3$ systems (for $x = 0.1$, $\Delta S_{\mathrm{m}}^{m}$=40 J kg^{-1} K^{-1} for 5 T and 21.9 J kg^{-1} K^{-1} for 2 T field changes), and EuSe ($\Delta S_{\mathrm{m}}^{m}$=37.5 J kg^{-1} K^{-1} for 5 T and 23.5 J kg^{-1} K^{-1} for 2 T field changes) [80, 130, 131]. In these systems also, the position of maximum in $\Delta S_{\mathrm{m}}(T)$ curve is insensitive to field change and it occurs at T_{N}. However, the value of ΔS_{m} for ETNO (x=0.15) is significantly larger than that reported for the most typical low temperature magnetic refrigerant Gd$_3$Ga$_5$O$_{12}$ (GGG) ($\Delta S_{\mathrm{m}}^{m}$=16.6 J kg^{-1} K^{-1} for 5 T); several other rare-earth titanates such as Eu$_{1-x}$Cr$_x$TiO$_3$ systems (for x=0.1, $\Delta S_{\mathrm{m}}^{m}$=30 J kg^{-1} K^{-1} for 5 T and 16.8 J kg^{-1} K^{-1} for 2 T field changes); DyTiO$_3$ ($\Delta S_{\mathrm{m}}^{m}$=15.8 J kg^{-1} K^{-1} for 5 T and 10 J kg^{-1} K^{-1} for 2 T field changes);

HoTiO$_3$ (ΔS_m^m=11 J kg^{-1} K^{-1} for 5 T and 6 J kg^{-1} K^{-1} for 2 T field changes); ErTiO$_3$ (ΔS_m^m=9.8 J kg^{-1} K^{-1} for 5 T and 5 J kg^{-1} K^{-1} for 2 T field changes); TmTiO$_3$ (ΔS_m^m=13 J kg^{-1} K^{-1} for 5 T and 7 J kg^{-1} K^{-1} for 2 T field change); YbTiO$_3$ (ΔS_m^m=5.3 J kg^{-1} K^{-1} for 5 T and 3 J kg^{-1} K^{-1} for 2 T field changes) [132, 133, 55]; and Eu-based compounds such as Eu$_3$O$_4$ (ΔS_m^m=12.7 J kg^{-1} K^{-1} for 5 T and 7.1 J kg^{-1} K^{-1} for 2 T field changes); EuO (ΔS_m^m=17.5 J kg^{-1} K^{-1} for 5 T and 8.5 J kg^{-1} K^{-1} for 2 T field changes); EuHo$_2$O$_4$ (ΔS_m^m=22.5 J kg^{-1} K^{-1} for 5 T and 8.2 J kg^{-1} K^{-1} for 2 T field changes); and EuDy$_2$O$_4$ (ΔS_m^m=19 J kg^{-1} K^{-1} for 5 T and 7.5 J kg^{-1} K^{-1} for 2 T field changes) [134, 135, 136]. We would also like to mention that this value of magnetic entropy change in the present system is larger than that reported for several multiferroic compounds like HoMnO$_3$ (ΔS_m^m=9.6 J kg^{-1} K^{-1} for 5 T and 2.7 J kg^{-1} K^{-1} for 2 T field changes); Dy$_{1-x}$Ho$_x$MnO$_3$ (for x=0.1, ΔS_m^m=7 J kg^{-1} K^{-1} for 7 T field change); DyFe$_{0.5}$Cr$_{0.5}$O$_3$ (ΔS_m^m=11.3 J kg^{-1} K^{-1} for 5 T and 5 J kg^{-1} K^{-1} for 2 T field changes); and HoMn$_2$O$_5$ (ΔS_m^m=10 J kg^{-1} K^{-1} for 5 T and 3 J kg^{-1} K^{-1} for 2 T field changes) [137, 138, 139, 140, 141].

The influence of magnetic field on the heat capacity has also been investigated. The temperature dependence of the C_p for different applied fields is plotted in Fig. 5.3(a). The zero-field heat capacity decreases with decrease in temperature down to 12 K and then increases sharply and exhibits a λ-like peak at T_C. The sharp λ-like peak at T_C suggests that the phase transition is continuous in nature. It can be understood from the plots that the nature of the C_p curve is strongly affected by the magnetic field. The peak gets broadened with increasing field strength. Similar to ETO, the zero-field $C_\mathrm{p}(T)$ curve was fitted using a combined Debye and Einstein model in the temperature range of $30-220$ K in order to estimate the lattice part of heat capacity. The obtained lattice contribution was then subtracted
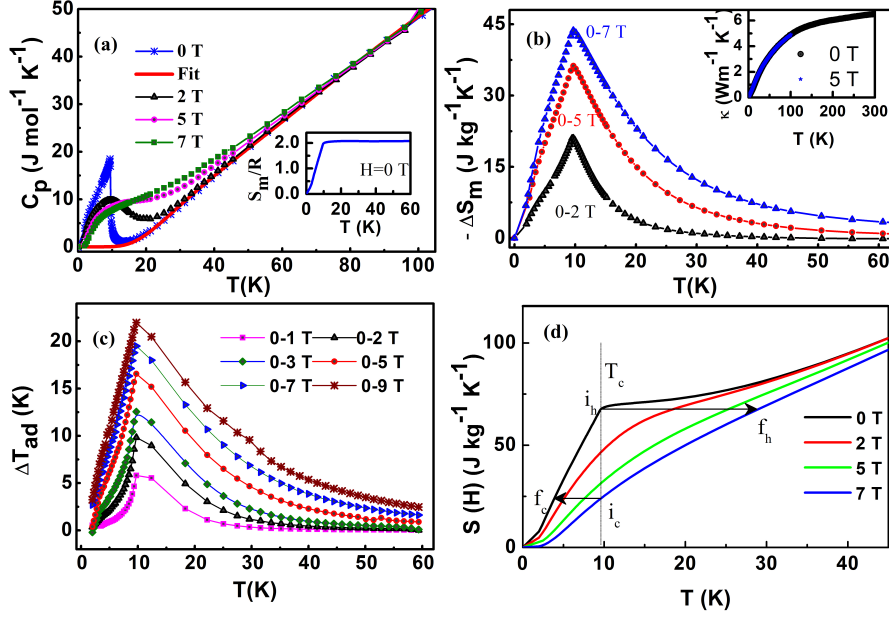
Figure 5.3: For ETNO (x=0.15) single crystal, (a) T dependence of C_p at different H and the combined Debye plus Einstein fit to the zero-field C_p data (solid line). Inset: T variation of zero-field magnetic entropy (S_m), (b) T dependence of $-\Delta S_\mathrm{m}$ from C_p measurement and the inset shows the T dependence of thermal conductivity at 0 and 5 T magnetic fields, (c) ΔT_ad calculated from the zero-field heat capacity and magnetization data, and (d) T dependence of total entropy, $S(H,T)$, at different magnetic fields obtained from heat capacity data. $\mathrm{i}_c \rightarrow \mathrm{f}_c$ and $\mathrm{i}_h \rightarrow \mathrm{f}_h$ represent adiabatic cooling and heating effects at the transition temperature T_C, respectively.

from the total heat capacity to determine the magnetic heat capacity C_{m} and hence the entropy (S_{m}) associated to the FM ordering at 9.5 K. S_{m} is calculated by integrating $(C_{\mathrm{m}}/T)dT$. The estimated saturation value of S_{m} at zero field is 17.3 J mol^{-1} K^{-1} which is almost similar to that theoretically expected from eq.(1.36) for the Eu^{2+} (S=7/2), i.e., $Rln8$=17.28 J mol^{-1} K^{-1}. It can also be mentioned that more than 95% of the magnetic entropy is released just below the FM transition. This indicates that a major fraction of $4f$ spins is participating in the magnetic ordering. However, with increasing field, the magnetic entropy shifts rapidly towards the higher temperature region. To check the consistency in our results on the estimated magnetic entropy change from the $M(H)$ data with that from the heat capacity data, the magnetic entropy change has also been calculated from the field dependence of the heat capacity for different applied fields as described in section 1.6.2 and is shown in Fig. 5.3(b) as a function of T. It is clear from the plot that ΔS_{m} calculated from magnetization and heat capacity data are close to each other. For the present compound, the temperature dependence of thermal conductivity for 0 and 5 T is shown in the inset of Fig. 5.3(b). In magnetic refrigeration, besides the larger value of isothermal magnetic entropy change, the cycle frequency is also an important factor [142]. The later involves a fast heat exchange, i.e., it is required for a material to possess a high thermal diffusivity, which is the ratio of thermal conductivity to the thermal capacity per unit volume. From the zero-field specific heat and thermal conductivity data for the present sample and using the density [104] of 6.8×10^3 kg m^{-3}, we deduced the thermal diffusivity in the range of 3×10^{-5} to 8×10^{-6} m^2 s^{-1} below the transition temperature which is significantly larger than that observed for several perovskites [143].

The adiabatic temperature change ΔT_{ad} is calculated by using the zero-field heat capacity and the $M(H)$ data as mentioned in the introduction part and plotted for different magnetic fields in Fig. 5.3(c). The nature of the $\Delta T_{\mathrm{ad}}(T)$ curves is quite similar to that of $\Delta S_{\mathrm{m}}(T)$. ΔT_{ad} is also large, increases monotonically with increasing field and reaches a value as high as 22 K at 9.5 K for a field change of 9 T. However, there is a large asymmetry between the heating effect (ΔT_{ad} heating) when applying a field adiabatically and the cooling effect when removing the field adiabatically (ΔT_{ad} cooling) at this low temperature, where the entropy increases very rapidly in zero-field and much slower in an applied magnetic field. So to interpret the results of adiabatic temperature change from a realistic point of view, we have shown the actual adiabatic cooling ($\mathrm{i}_c{\rightarrow}\mathrm{f}_c$) and heating ($\mathrm{i}_h{\rightarrow}\mathrm{f}_h$) effects at 9.5 K in a typical magnetic refrigeration cycle in Fig. 5.3(d). These two processes exhibit the difference between adiabatic cooling and adiabatic heating. Similar to ΔS_{m}, ΔT_{ad} can also be obtained solely from the heat capacity data. We have tabulated the maximum values of both ΔS_{m} and ΔT_{ad} estimated from the field dependence of M and C_{p} for three different fields. Table 5.1 shows that these parameters determined from eqs. (1.28) and (1.34) using two different techniques are comparable. It is clear from the above figures that the magnetocaloric parameters are also quite large for a small magnetic field change. Although the magnetocaloric entropy change has been estimated for pure and Ba-doped $\mathrm{EuTiO_3}$ using magnetization data, there is no report on the parameter ΔT_{ad} for these materials. We would also like to mention that there is one important difference between the above mentioned and present compounds. As the peak in the $\Delta S_{\mathrm{m}}(T)$ curve appears at higher temperature in ETNO (x=0.15), it has an advantage over $\mathrm{EuTiO_3}$ and $\mathrm{Eu_{1-x}Ba_xTiO_3}$ as a low-temperature refrigerant for

Table 5.1: Comparison of magnetocaloric parameters of $EuTi_{0.85}Nb_{1.5}O_3$ obtained from magnetization and heat capacity measurements.

Magnetic field change	0−2 T	0−5 T	0−7 T
$-\Delta S_m(M)$ [J kg^{-1} K^{-1}]	23.8	39.6	46.2
$-\Delta S_m(C_P)$ [J kg^{-1} K^{-1}]	21.0	36.3	43.7
$\Delta T_{ad}(M)$ [K]	9.8	16.5	19.5
$\Delta T_{ad}(C_P)$ [K]	8.6	15.5	19.2

the liquefaction of hydrogen in fuel industry. Moreover, the values of ΔT_{ad} are 16.5 K for 5 T and 9.8 K for 2 T field changes which are larger than that of the previously mentioned compounds such as Eu_3O_4 (ΔT_{ad}=7 K for 5 T and 3.8 K for 2 T); EuO (ΔT_{ad}=6.8 K for 5 T and 3.2 K for 2 T); $EuHo_2O_4$ (ΔT_{ad}=3 K for 2 T); $EuDy_2O_4$ (ΔT_{ad}=5 K for 2 T); and $HoMnO_3$ (ΔT_{ad}=4 K for 5 T), etc. [134, 135, 136, 137, 138].

5.4   Conclusion

We doped 15% Nb at the Ti site in $EuTiO_3$ and investigated the magnetic properties in details. Also, we have calculated the magnetocaloric parameters from both of magnetization and heat capacity measurements. The deduced values of the entropy change and adiabatic temperature change for a field variation of 9 T are 51.3 J kg^{-1} K^{-1} and 22 K, respectively near the Curie temperature $T_C = 9.5$ K. This compound also exhibits giant magnetocaloric parameters at a moderate field of 2 T. This indicates that $EuTi_{0.85}Nb_{0.15}O_3$ could be a potential material for low-temperature and low-field magnetic refrigeration.

6

Large low-field magnetic refrigeration in ferromagnetic insulator $EuTi_{0.9}V_{0.1}O_3$

6.1 Introduction

In the previous chapter, we have mentioned that large MCE is observed in both the compound, ETO and ETNO (x=0.15), at low temperature [103, 80]. Though ΔS_{m} is reduced slightly due to Nb doping, but the magnetic cooling/heating capacity (MC) parameter enhances due to the broadening of the $\Delta S_{\mathrm{m}}(T)$ curve [103]. However, the main drawback of ETNO is its metallic property. Due to high electrical conductivity, the cooling efficiency may suppress remarkably as a result of eddy current loss. To avoid this undesirable loss, our aim is to obtain high MC without changing the insulating nature of the ground state. As vanadium is in the same group of Nb in the Periodic Table and the ionic size of V is almost equal to Ti, it is expected that Ti can be replaced by V. Keeping this in mind, V is doped at the Ti site in ETO. Unlike ETNO, $EuTi_{0.9}V_{0.1}O_3$ (ETVO) is a ferromagnetic

insulator. In the present work, we have investigated the temperature and field dependence of magnetization and heat capacity for ETVO and calculated several magnetocaloric parameters in order to test whether this material is appropriate for low-temperature magnetic cooling.

6.2   Experimental details

Polycrystalline ETVO sample was prepared by the standard solid-state reaction method. Stoichiometric mixtures of Eu_2O_3 (pre-heated), V_2O_5, and TiO_2 were heated in a reduced atmosphere (5% hydrogen and 95% argon) at 1000-1050 °C for two days with intermediate grindings. The obtained powder was then pressed into pellets and sintered at 1100 °C in the same atmosphere. Phase purity of the material was checked by the powder XRD method with CuK_α radiation in a high resolution Rigaku diffractometer (TTRAX III). Figure 6.1 shows the XRD pattern of the ETVO sample at room temperature. No trace of impurity phase has been detected within the resolution of XRD. All the peaks in XRD were assigned to cubic structure of space group $Pm3m$ using the Reitveld method. The observed lattice parameters $a=b=c=3.9090(1)$ Å are close to that for ETO (3.905 Å) [59, 144].

The temperature and field dependence of the dc magnetization measurements were carried out in a SQUID-VSM. The specific heat measurement was performed in a PPMS. Similar to niobium, the valence state of vanadium in ETVO is important. V can either be in 4+ or in 5+ state. The ionic radius of V^{4+} (0.58 Å) is slightly smaller than Ti^{4+} (0.605 Å) whereas that of V^{5+} (0.54 Å) is quite smaller than Ti^{4+}. As V doping at the Ti site changes the lattice parameters slightly with respect to the undoped one, V is more likely to be in the 4+ valence state. Magne-
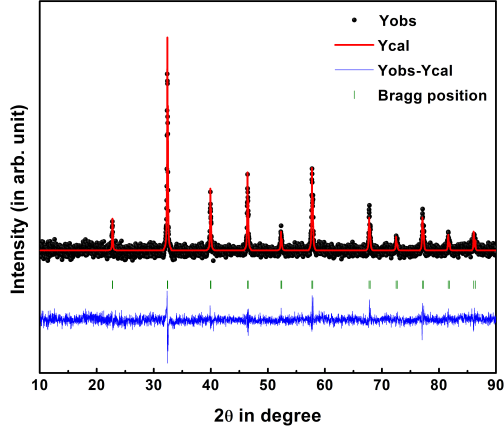
Figure 6.1: X-ray powder diffraction pattern for ETVO at room temperature. The red solid line corresponds to the Rietveld refinements of diffraction pattern.

tization measurements, to be discussed later on, also support the 4+ state of V ion.

6.3   Results and Discussions

The temperature variation of zero-field-cooled (ZFC) magnetization M_{ZFC} and field-cooled (FC) magnetization M_{FC} of ETVO, measured at different magnetic fields are shown in Fig. 6.2(a). For clarity, a few representative plots are displayed. Under ZFC condition, the sample was cooled from 300 to 2 K in absence of magnetic field and the magnetization data were recorded during the heating cycle in the presence of a magnetic field. Under FC condition, the sample was cooled down to 2 K in a magnetic field and the data have been taken simultaneously during cooling. In the PM state, M_{FC} and M_{ZFC} increase monotonically with the decrease in temperature, and they do not split from each other. However, the na-

ture of temperature dependence of M_{ZFC} and M_{FC} curves are very different at low fields and low temperatures; M_{FC} continues to increase very slowly with decreasing T like a Brillouin function which is a signature of ferromagnetism, while M_{ZFC} decreases gradually with decreasing temperature, i.e., M_{FC} and M_{ZFC} bifurcate below the peak in M_{ZFC} curve. This type of bifurcation between M_{ZFC} and M_{FC} curves is found in several transition metal based oxide ferromagnets. In such a case, the zero-field-cooled sample reaches at a random domain distribution state while the field-cooled sample goes to the remanent magnetization state. We specify the peak position in M_{ZFC} curve as the Curie temperature $T_C \sim 4.84$ K. However, T_C can be estimated more accurately from the heat capacity data. With increasing the field strength, the separation between ZFC and FC magnetization decreases and disappears at around 500 Oe. The presence of a peak in the ZFC curve suggests a strong competition between FM and AFM interactions. This behavior of the $M(T)$ curve is quite common in ferromagnetic rare-earth cobaltites [145, 146]. To understand the magnetic ground state in a better way, inverse susceptibility (χ^{-1}) versus temperature is plotted in the inset of Fig. 6.2(a). The linear behavior of $\chi^{-1}(T)$ curve over a wide range in the PM state suggests that susceptibility follows the Curie-Weiss law. The linear fit to experimental data gives $\theta_{CW}=5.02$ K and the effective magnetic moment $P_{eff}= 8.08$ μ_B/f.u. For ETO, the reported values of P_{eff} and θ_{CW} are 7.9 μ_B/f.u and 3.2 K respectively [103, 80]. Therefore, the values of P_{eff} and θ_{CW} for ETVO are slightly larger than that for the undoped one.

To investigate the effect of magnetic field on the magnetic ground state of ETVO, we have measured the field dependence of magnetization at different T from 2 to 60 K. Some representative plots of $M(H)$ are shown in Fig. 6.2(b) for
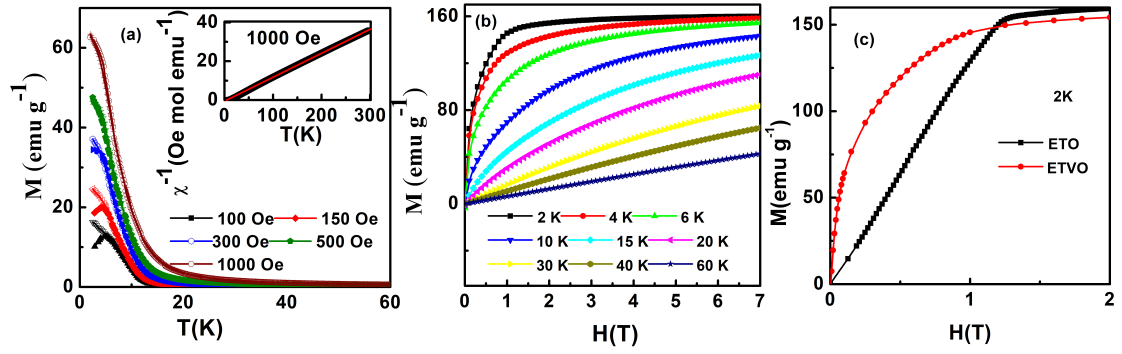
Figure 6.2: For ETVO, (a) T dependence of ZFC and FC magnetization at different magnetic fields between 100 and 1000 Oe. The open symbols indicate FC curves, whereas the solid symbols stand for ZFC curves. The inset shows the χ^{-1} for 1000 Oe, (b) $M(H)$ curves. (c) Comparison between the nature of $M(H)$ curves of ETO and ETVO.

magnetic fields up to 7 T. Remarkably, $M(H)$ is nonlinear even at temperatures as high as 30 K, which is well above the T_C. At low temperature, magnetization increases rapidly with field and then tends to saturate. At 2 K and 7 T, the value of M is found to be 7.1 μ_B per formula unit. The deduced value of magnetic moment is 0.1 μ_B larger than the expected spin only moment of Eu^{2+}, indicating an additional contribution from $3d$ shell of V ion [80]. Indeed, this excess 0.1 μ_B exactly coincides with the expected value of moment when 10% Ti is replaced by isovalent V. This confirms the 4+ valence state of V ion. Similar to ETNO, we have compared the nature of $M(H)$ curve for ETVO with that for ETO in particular, at low temperature which is drawn in Fig. 6.2(c). In ETVO, $M(H)$ exhibits a downward curvature in the low-field region below ~2 T and no clear anomaly or signature is observed due to the field-induced transition. The nature of the $M(H)$ curve of ETVO is very similar to a typical FM system. In this context, we compare the nature of low-field $M(T)$ curves in Fig. 6.2(a) with that for ETO. For the undoped ETO compound, the PM to AFM transition is very sharp and

the FC and ZFC magnetization curves do not bifurcate below T_N [80]. Also, due to the vanadium doping at the Ti site, magnetization increases with respect to the undoped system and θ_{CW} increases from 3.2 to 5 K. All the above features of $M(H)$ and $M(T)$ curves suggest that the AFM superexchange interaction between the Eu^{2+} moments weakens with V doping at the Ti site in ETO.
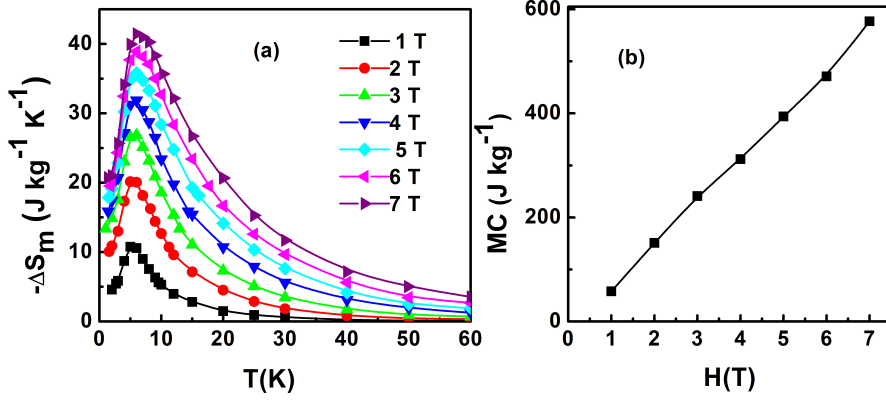
Figure 6.3: For ETVO, (a) T dependence of the $-\Delta S_m$, (b) H variation of MC.

In order to know whether ETVO is a suitable candidate for magnetic refrigeration at low temperature, we should have an idea about the magnetic entropy change (ΔS_m). The entropy change is calculated from eq. (1.28). Some representative plots of temperature dependence of ΔS_m for magnetic fields between 1 and 7 T are shown in Fig. 6.3(a). ΔS_m is negative over the whole temperature range and its value increases monotonically with increasing field. The maximum value of ΔS_m (ΔS_m^m) is 41.4 J kg^{-1} K^{-1} for a field change of 7 T. At low fields, ΔS_m below the transition temperature does not decrease as fast as in the case of ETO. For an example, ΔS_m in ETO decreases rapidly below T_N and becomes extremely small ($\sim$0) at 4 K, for field change $\Delta H = 0 \rightarrow 1$ T. At the lowest measured temperature 2

Table 6.1: Comparison of electrical and mechanical energy efficiencies of ETVO and different magnetocaloric materials. ($T_0=$ 5 K, operating temperature; $\Delta H_0=$ change in applied magnetic field; Q= released heat of magnetic material; W= Work; Q/W = efficiency). The values inside the bracket corresponds to 5 T magnetic field.

Material	$\mu_0 \Delta H_0$(T)	Q(J cm^{-3})	Electrical Work(J cm^{-3})	Electrical Efficiency (%)	Mechanical Work (J cm^{-3})	Mechanical Efficiency(%)	Reference
ETVO	2(5)	0.69(1.21)	2.11(10.82)	32(11)	1.55(4.53)	44(26.6)	This work
ETO	2(5)	0.50(1.11)	2.40(11.84)	21(9.4)	1.37(4.54)	36.6(24.5)	[80]
HoMnO$_3$	2(5)	0.11(0.38)	1.76(11.11)	6(3.4)	0.34(1.97)	30.9(19.2)	[138]
EuDy$_2$O$_4$	2(5)	0.31(0.83)	2.83(14.88)	10(5)	1.10(4.10)	30(20)	[136]
EuHo$_2$O$_4$	2(5)	0.36(1.00)	2.52(11.63)	14.15(8.5)	1.13(4.40)	31.4(22.7)	[136]
ErRu$_2$Si$_2$	2(5)	0.48(0.78)	2.31(10.83)	20.7(7.17)	1.15(3.69)	41.7(21)	[147]
GdVO$_4$	2(5)	0.25(1.06)	2.13(12.40)	11(8)	0.56(2.60)	44(40)	[148]
HoMn$_2$O$_5$	2(5)	0.05(0.134)	1.18(11)	3(1.2)	0.36(1.8)	15(7.4)	[141]

K and for the same field variation, -ΔS_{m} for ETVO is found to be 4.5 J kg^{-1}K^{-1}, which is almost 50% of ΔS_{m}^m. As ETVO is a FM system, a small applied field can easily align the spins and hence, large MCE occurs. On the other hand, ETO undergoes a transition from a spin-flopped AFM phase to a field-induced FM phase or PM phase above 1.2 T and as a result, -ΔS_{m} is very small at low-temperature and low-fields. As external magnetic field creates disorder in sublattice magnetization, -ΔS_{m} can also be negative for an AFM system below a critical field for $T \ll T_N$.

The parameter MC is estimated from eq. (1.29) and Fig. 6.3(b) shows that MC increases almost linearly with H and reaches as high as 577 J kg^{-1} for a field change of 7 T. This value of MC is larger than that observed in ETO (500 J kg^{-1}) and ETNO (x=0.15) (556 J kg^{-1}).

The important findings in the present work are the large values of magnetocaloric parameters in ETVO. First, the value of maximum entropy change (ΔS_{m}^m) is 35.6 J kg^{-1} K^{-1} for a field change of 5 T whereas for 2 T it is 20 J kg^{-1} K^{-1}. These

values are much larger than that reported for several well known low-temperature MCE materials such as ErRu$_2$Si$_2$ [147](ΔS_{m}^m = 17.6 J kg^{-1} K^{-1} for 5 T and ΔS_{m}^m = 11.7 J kg^{-1} K^{-1} for 2 T); and TmCuAl [149] (ΔS_{m}^m = 24.3 J kg^{-1} K^{-1} for 5 T and ΔS_{m}^m = 19.6 J kg^{-1} K^{-1} for 2 T), etc. The magnetocaloric parameters for ETVO are also significantly larger than that observed in several Eu-based compounds having magnetic ordering temperature near 5 K and show large MCE such as EuHo$_2$O$_4$ [136](ΔS_{m}^m = 23 J kg^{-1} K^{-1} for 5 T and ΔS_{m}^m = 8.2 J kg^{-1} K^{-1} for 2 T); EuDy$_2$O$_4$ [136](ΔS_{m}^m = 19 J kg^{-1} K^{-1} for 5 T and ΔS_{m}^m = 7 J kg^{-1} K^{-1} for 2 T); and Eu$_3$O$_4$ [134](ΔS_{m}^m = 12.7 J kg^{-1} K^{-1} for 5 T and ΔS_{m}^m = 7.1 J kg^{-1} K^{-1} for 2 T), etc. In magnetic refrigeration, ΔS_{m} per unit volume is important. As the density of the studied material (6.9 g cm^{-3}) is high, the value of ΔS_{m} per unit volume is also quite large. We have also calculated entropy change per mole and found that molar entropy is quite large for ETVO. Secondly, compared to the above mentioned magnetic materials, ETVO has a much larger MC which is 394 and 151 J kg^{-1} for the field changes of 5 and 2 T, respectively. In general, Eu^{2+} (and Gd^{3+}) based compounds are favorable as magnetic refrigerant in comparison to the other rare-earth based compounds. As Eu^{2+} (and Gd^{3+}) ion has no orbital angular momentum (L=0), the crystal field effect, which is responsible for magnetocrystalline anisotropy, is negligible in Eu^{2+} (and Gd^{3+}) based compounds. For this reason, magnetization is expected to be almost isotropic and large.

The values of ΔS_{m} for both ETVO and ETO are large and comparable but MC for the former is larger. This is because ΔS_{m} for ETVO is also large in the PM state well above the T_{C}, which can be explained quantitatively by mean field theory. Well above the T_{C}, the mean field approximation of the entropy change is

[150]:

$$\Delta S_m(T, H) = -\frac{1}{2}\frac{CH^2}{(T - T_{\rm C})^2} \tag{6.1}$$

while for an antiferromagnet, the same approximation gives:

$$\Delta S_m(T, H) = -\frac{1}{2}\frac{CH^2}{(T + T_{\rm N})^2}. \tag{6.2}$$

As C is almost same for both the compounds, it is clear from the above expressions that $\Delta S_{\rm m}$ is larger for ETVO in the PM state. The higher cooling efficiency makes the insulating ETVO a much more efficient low-temperature magnetic refrigerant and has an added advantage over both ETO and ETNO (x=0.15) for H$_2$ liquefaction.
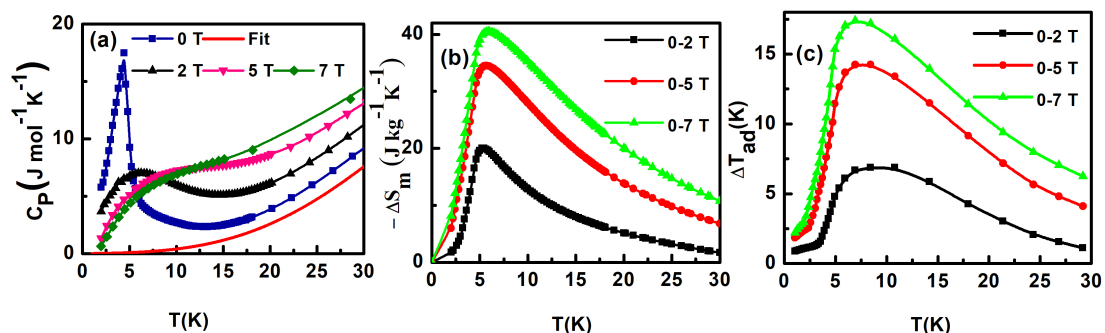
Figure 6.4: For ETVO, (a) T dependence of the total specific heat (C_p) at different magnetic fields and the combined Debye plus Einstein fit to the zero-field specific heat data (solid line), (b) T dependence of -$\Delta S_{\rm m}$ from heat capacity measurement, and (c) ΔT_{ad} calculated from the zero field heat capacity and magnetization data.

The temperature dependence of specific heat capacity (C_p) for ETVO at different applied magnetic fields has been studied and is shown in Fig. 6.4(a). With

decreasing temperature, the zero-field heat capacity decreases in a same way of ETNO and the magnetic ordering has been reflected as a sharp λ-like peak at $T_\mathrm{C}=$ 4.54 K, which is a signature of continuous phase transition. Unlike magnetization, T_C can be determined accurately from the $C_p(T)$ curve due to the sharp nature of the peak. The influence of magnetic field on C_p is clearly reflected. One important difference in the nature of $C_p(T)$ curve of ETVO and ETO is the evolution of the peak with magnetic field. For ETVO, the heat capacity shows a round anomaly at low field, typical for a FM system. In an AFM system, however, the peak remains sharp until the applied field exceeds the critical value required for spin-flop-PM transition as observed in ETO system [80]. The magnetic heat capacity C_m is calculated from the total heat capacity. We have deduced the magnetocaloric parameters from the heat capacity data. The magnetic entropy can be calculated using eq. (1.34) but for the studied compound, we cannot use the above formula to estimate magnetic entropy at low field as the extrapolation of S at $T_0=0$ K will include some error due to the presence of a strong peak in $C_p(T)$ curve slightly above 4 K and the appreciable value of C_p at 2 K. For the accurate determination of magnetic entropy, we have used the methods adopted for systems which exhibit similar strong anomaly in $C_p(T)$ curve at low temperature [151]. At first, we have considered the $C_m(T)$ curve at 7 T magnetic field to estimate S_m for which C_m at low temperature is very small and the extrapolation of $C_m(T)$ curve to $T=0$ is unambiguous. Then the entropy difference between 5 and 7 T fields at high temperature, which is quite small and has been reliably determined from the magnetization data, is used to estimate the absolute value of entropy at 5 T. Similarly, S_m has been determined for other two fields 0 and 2 T. The obtained saturation value of the zero-field magnetic entropy is 17.24 J mol^{-1} K^{-1} which is very close

to that expected for the Eu^{2+} ($S=7/2$). The magnetic entropy change ΔS_{m} has been calculated by using the relation $\Delta S_{\mathrm{m}} = S_m(T, H)$ - $S_m(T, 0)$ as shown in Fig. 6.4(b). It is clear from the plot that the values of ΔS_{m} calculated from magnetization and heat capacity data are comparable.

The adiabatic temperature change ΔT_{ad} is estimated from the magnetization data and zero-field heat capacity. ΔT_{ad} for different magnetic field change is shown in Fig. 6.4(c). ΔT_{ad} is also calculated independently using the heat capacity data. The nature of the $\Delta T_{\mathrm{ad}}(T)$ curve is quite similar to the $\Delta S_{\mathrm{m}}(T)$ curve. Both show a broad peak slightly above T_{C}. ΔT_{ad} attains maximum value of 17.4 K for the field change of 7 T, which is very large. ΔT_{ad} is also quite large for a small field change.

For practical purposes, apart from the above mentioned parameters related to MCE, it is a useful guide to select the magnetocaloric materials on the basis of energy efficiency where electrical or mechanical work is done to achieve highly reversible caloric effects. We have calculated the amount of electrical and mechanical work done using the formula described by Moya *et al.* [152] and compared with other high MCE materials. The heat produced by applied magnetic field (whether generated by electrically or mechanically) is given by $Q=T_0\Delta S_m$; T_0 is the operating temperature. As the studied material shows a peak in $\Delta S_m(T)$ near 5 K, we have chosen T_0 as 5 K. We have estimated the electrical and mechanical energy efficiencies for ETVO and other reported high MCE materials to make a comparison among them. Table 6.1 shows that both electrical and mechanical energy efficiencies of ETVO are larger than that for several low-temperature magnetic refrigerants.

6.4 Conclusion

We have doped 10% V at the Ti site in $EuTiO_3$ and studied the magnetic as well as magnetocaloric properties of this compound through magnetization and heat-capacity measurements. A large adiabatic temperature change of 17.4 K, isothermal entropy change of 41.4 J kg^{-1} K^{-1}, and a magnetic cooling/heating capacity of 577 J kg^{-1} for a field change of 7 T were found around the transition temperature. This compound also shows a remarkable magnetocaloric effect even in low magnetic fields below 2 T. These excellent magnetocaloric properties of $EuTi_{0.9}V_{0.15}O_3$ makes this system a potential material for low temperature and low field magnetic refrigeration.

7

Summary

In this chapter, we summarize the works presented in the previous chapters of the thesis. The main motivation of the present thesis is to investigate the magnetic, thermal, structural and electrical properties of undoped $EuTiO_3$, doped $EuTi_{1-x}M_xO_3$ ($M=Nb$, V).

In **Chapter 1**, we first introduced the perovskite oxides in a general manner as well as some fundamental mechanisms behind magnetic ordering are discussed thoroughly. Also, the basic characteristics of a strongly correlated material and the electronic properties of a ferromagnetic material are presented here. The basic principles of magnetocaloric phenomenon are described. Besides, a general overview of the theory of phase transition and critical phenomena have been addressed. A literature survey on $EuTiO_3$ has been presented here.

In **Chapter 2**, an overview of single crystal growth using traveling solvent float zone method is presented. The basic principle of operation of the characterization tools such as powder x-ray diffraction is demonstrated. Different magnetic and

physical property measurement techniques are described in this chapter.

In **Chapter 3**, we have presented the critical analysis of the magnetic phase transition of the antiferromagnetic undoped $EuTiO_3$ single crystal. The magnetization, specific heat, linear thermal expansion and magnetostriction of ETO single crystal have been investigated. We have performed the critical study from the high resolution thermal measurement data instead of using magnetic isotherms. As heat capacity measurement is very sensitive at low temperature, therefore, we have used these data to estimate the critical exponent of heat capacity (α). The estimated value of the exponent for low temperature transition establishes that this compound belongs to the 3D-Heisenberg universality class.

In **Chapter 4**, we have presented the detailed analysis of transport properties of single crystalline $EuTi_{1-x}Nb_xO_3$ (x=0.10, 0.15, 0.20) (ETNO). Bulk dc magnetization and heat capacity measurements were carried out for the basic characterizations. The observed results of the temperature and magnetic field dependence of resistivity of ETNO are compared and contrasted with the different classes of FM metals. Our detailed analysis of resistivity reveals the presence of different charge conduction mechanisms which make ETNO a unique FM metallic system. With increasing T, the charge scattering mechanism crosses over from electron-magnon to spin-disordering to Kondo to electron-electron scattering to an unusual $T^{3/2}$ dependence of resistivity due to non-Fermi-liquid behavior.

In **Chapter 5**, we have presented the temperature and field dependence of dc magnetization of $EuTi_{0.85}Nb_{0.15}O_3$ single crystal. The magnetocaloric effect in

ferromagnetic single crystal $EuTi_{0.85}Nb_{0.15}O_3$ has been investigated using magnetization and heat capacity measurements. The low-field giant magnetocaloric effect, together with the absence of thermal and field hysteresis makes $EuTi_{0.85}Nb_{0.15}O_3$ a very promising candidate for low temperature magnetic refrigeration.

In **Chapter 6**, the detailed magnetic properties as well as magnetocaloric effect have been studied for the ferromagnetic insulator $EuTi_{0.9}V_{0.1}O_3$. This compound also shows a remarkable magnetocaloric effect even in low magnetic fields. These excellent magnetocaloric properties of $EuTi_{0.9}V_{0.1}O_3$ suggest its suitability as a potential material for low-temperature and low-field magnetic refrigeration.

Bibliography

[1] J. P. Attfield, P. Lightfoot, and R. E. Morris, Dalton Trans. **44**, 10541 (2015).

[2] https://en.wikipedia.org/wiki/Lead titanate.

[3] V. M. Goldschmidt, Die Naturwissenschaften **21**, 477 (1926).

[4] E. Dagotto, *Nanoscale Phase Separation and Colossal Magnetoresistance*, Springer, New York, 2002.

[5] E. Dagotto, Rev. Mod. Phys. **66**, 763 (1994).

[6] E. Dagotto, T. Hotta, and A. Moreo, Phys. Rep. **344**, 1 (2001).

[7] https://stock.adobe.com/images/3d-orbital-orientation/68191499.

[8] K. Mousseau, *F Orbitals and Metal-Ligand Bonding in Octahedral Complexes.*

[9] https://en.wikibooks.org/wiki/Introduction to Inorganic Chemistry/Coordination Chemistry and Crystal Field Theory.

[10] A.P. Ramirez, Annual Review of Material Science **24**, 453-480 (1994).

[11] H. A. Jahn and E. Teller, *Stability of Polyatomic Molecules in Degenerate Electronic States. I. Orbital Degeneracy.* (1937).

[12] http://home.iitk.ac.in/ madhavr/CHM102/Physical/Lec4.pdf.

[13] https://en.wikipedia.org/wiki/Ferromagnetism.

[14] B. C. den Hertog and M. J. P. Gingras, Phys. Rev. Lett. **84**, 3430 (2000).

[15] D. C. Jiles, *Introduction to Magnetism and Magnetic Materials*, CRC Press, USA, (1998).

[16] A. L. Wysocki and T. Birol, Phys. Rev. B **93**, 134425 (2016).

[17] J. B. Goodenough, *Magnetism and Chemical Bond*, Interscience Publishers, New York, (1963).

[18] M. J. Opel, Phys. D: Appl. Phys. **45**, 033001 (2012).

[19] https://www.uni-muenster.de/Physik.AP/Demokritov/en/Forschen/Forschungsschwerpunkte/

[20] C. Kittel, *Introduction to Solid State Physics*, Wiley, New York, (2005).

[21] M. Imada, A. Fujimori, Y. Tokura, Rev. Mod. Phys. **70**, 4 (1998).

[22] A. J. Schofield, Contemporary Physics, **40**, 95-115 (1999).

[23] P. Nozieres, D. Pines. *Theory Of Quantum Liquids*. Westview Press, (1999).

[24] F. Cipcigan, *Electrical Transport in Fermi Liquids*.

[25] M. B. Maple *et al.*, J Low Temp Phys **161**, 4-54 (2010).

[26] J. Kondo, Prog. Theor. Phys **32**, 37 (1964).

[27] J. Kroha, Series "Modeling and Simulation" **7**, 12.1-12.27 (2017).

[28] J. C. Y. Teo, L. Fu, and C. L. Kane, Chin. Phys. B **25**, 077401 (2016).

[29] J. S. Dugdale, *The Electrical Properties of Metals and Alloys* (1979).

[30] O. Gutfleisch *et al.*, Adv. Mater. **23**, 821 (2011).

[31] B. G. Shen *et al.*, Adv. Mater. **21**, 4545 (2009).

[32] C. Zimm *et al.*, Adv. Cryog. Eng.**43**, 1759 (1998).

[33] B. F. Yu, Q. Gao, X. Z. Meng, and Z. Chen, Int. J. Refrig. **26**, 622 (2003).

[34] S. M. Benford and G. V. Brown, J. Appl. Phys. **52**, 2110 (1981).

[35] A. Smith, Eur. Phys. J. H **38**, 507 (2013).

[36] P. Debye, Ann. Phys. (Leipzig) **386**, 1154 (1926).

[37] W. F. Giauque, J. Am. Chem. Soc. **49**, 1864 (1927).

[38] W. F. Giauque and D. P. MacDougall, Phys. Rev. **43**, 768 (1933).

[39] G. V. Brown, Journal of Applied Physics **47**, 3673 (1976).

[40] K. A. Gschneidner Jr, V. Pecharsky, A. Tsokol, Rep. Prog. Phys. **68**, 1479 (2005).

[41] L. Li, K. Nishimura, W. D. Hutchison, Z. Qian, D. Huo, and T. Namiki, Appl. Phys. Lett. **100**, 152403 (2012).

[42] A. Rostamnejadi, M. Venkatesan, P. Kameli, H. Salamati, and J. M. D. Coey, J. Magn. Magn. Mater. **323**, 2214 (2011).

[43] M. Baazaoui, M. Boudard, and S. Zemni, Mater. Lett. **65**, 2093 (2011).

[44] R. Mondal, R. Nirmala, J. A. Chelvane, and A. K. Nigam, J. Appl. Phys. **113**, 17A930 (2013).

[45] E. Bruck, O. Tegus, D. T. C. Thanh, and K. H. J. Buschow, J. Magn. Magn. Mater. **310**, 2793 (2007).

[46] H. Wada and Y. Tanabe, Appl. Phys. lett. **79**, 3302 (2001).

[47] E. Bruck, M. Ilyn, A. M. Tishin, and O. Tegus, J. Magn. Magn. Mater. **290**, 8 (2005).

[48] J.A. Barclay, S.R. Jaeger, F.C. Prenger, Advances in Cryogenic Engineering **35B**, 1097 (1990) .

[49] K. Matsumoto, T. Okano, A. Matsuzaki, K. Kamiya, T. Numazawa, Physica B **329-333**, 1261-1262 (2003).

[50] F.C. Prenger, D.D. Hill, I. Trueblood, T. Servais, J. Ladsch, J.A. Barclay, Advances in Cryogenic Engineering **35B**, 1105 (1990).

[51] V. Provenzano, J. Li, T. King, E. Canavan, P. Shirron, M. DiPirro, R.D. Shull, Journal of Magnetism and Magnetic Materials **266**, 185 (2003).

[52] McMichael, J.J. Ritter, R.D. Shull, Journal of Applied Physics **73**, 6946 (1993).

[53] R.D. McMichael, R.D. Shull, L.J. Swartzendruber, L.H. Bennett, R.E. Watson, Journal of Magnetism and Magnetic Materials **111**, 29 (1992).

[54] T. Numazawa, T. Hashimoto, H. Nakagome, N. Tanji, O. Horigami, Advances in Cryogenic Engineering **29**, 589 (1984) .

[55] Y. Su *et al.*, Phys. Rev. B **87**, 195102 (2013).

[56] V. Scagnoli *et al.*, Phys. Rev. B **86**, 094432 (2012).

[57] T. R. McGuire *et al.*, J. Appl. Phys. **37**, 981 (1966).

[58] H. Akamatsu *et al.*, Phys. Rev. B **83**, 214421 (2011).

[59] T. Katsufuji and H. Takagi, Phys. Rev. B **64**, 054415 (2001).

[60] V. V. Laguta *et al.* J. Phys.: Condens. Matter **29**, 105401 (2017).

[61] J. Brous, I. Fankuchen, and E. Banks, Acta Crystallogr. **6**, 67 (1953).

[62] M. Allieta *et al.*, Phys. Rev. B **85**, 184107 (2012).

[63] A. Bussmann-Holder *et al.*, Phys. Rev. B **83**, 212102 (2011).

[64] T. Birol and C. J. Fennie, Phys. Rev. B **88**, 094103 (2013).

[65] P. G. Reuvekamp *et al.*, Phys. Rev. B **90**, 104105 (2014).

[66] L. J. Spalek *et al.*, Phys. Rev. B **90**, 054119 (2014).

[67] Z. Guguchia *et al.*, Phys. Rev. B **90**, 064413 (2014).

[68] P. G. Reuvekamp *et al.*, Phys. Rev. B **90**, 094420 (2014).

[69] R. J. Hill, *The Rietveld Method*, R. A. Young, Editor, p. 95, Oxford Univ. press, Oxford (1995).

[70] J. R. Carvajal, *An Introduction to the Program FullProf 2000*, Laboratoire Leon Brillouin, CEA-CNRS, Saclay (2001).

[71] *Quantum Design, Magnetic Property Measurement System: SQUID-VSM User's Manual* (2009).

[72] http://www.tf.uni-kiel.de/servicezentrum/neutral/praktika/anleitungen/m106.

[73] *Physical Property Measurement System, Vibrating Sample Magnetometer (VSM) Option User's Manual*, Part Number 1096-100, A-2 (Quantum Desigm).

[74] L. J. Vander Pauw, Philips Res. Repts. **13**, 1 (1958).

[75] J. H. Scofield, Rev. Sci. Instrum. **58**, 985 (1987).

[76] J. C. Lashley *et al.*, Cryogenics **43** 369 (2003).

[77] *Physical Property Measurement System, Heat Capacity Option User's Manual,* Part Number 1085-150, H-1 (Quantum Design).

[78] J. S. Hwang, K. J. Lin, and C. Tien, Rev. of Sci. Inst. **68**, 94 (1997).

[79] M. Rotter *et al.*, Rev. Sci. Instrum. **69**, 2742 (1998).

[80] A. Midya *et al.*, Phys. Rev. B **93**, 094422 (2016).

[81] A. P. Petrović *et al.*, Phys. Rev. B **87**, 064103 (2013).

[82] A. Oleaga *et al.*, J. Phys.: Condens. Matter **17**, 6729 (2005).

[83] A. Oleaga *et al.*, Phys. Rev. B **85**, 184425 (2012).

[84] M. Imada, A. Fujimori, and Y. Tokura, Rev. Mod. Phys. **70**, 1039 (1998).

[85] L. Klein *et al.*, J. Phys.: Condens. Matter. **8**, 10111 (1996).

[86] M. Vojta, Rep. Prog. Phys. **66**, 2069 (2003).

[87] M. Brando *et al.*, Rev. Mod. Phys. **88**, 025006 (2016).

[88] S. A. Grigera *et al.*, Science **294**, 329 (2001).

[89] J. Kondo, Prog. Theor. Phys. **27**, 772 (1962).

[90] P. Nozieres, *Theory of Interacting Fermi Systems,*(Benjamin, New York, 1964).

[91] R. P. Smith *et al.*, Nature (London) **455**, 1220 (2008).

[92] J. Liu *et al.*, Nat. Commun. **4**, 2714 (2013).

[93] J.-S. Zhou *et al.*, Phys. Rev. Lett. **94**, 226602 (2005).

[94] Q. Si and F. Steglich, Science **329**, 1161 (2010).

[95] C. Pfleiderer *et al.*, Nature (London) **414**, 427 (2001).

[96] C. Pfleiderer *et al.*, Nature (London) **427**, 227 (2004).

[97] J. Custers *et al.*, Nature (London) **424**, 524 (2003).

[98] L. Klein *et al.*, Phys. Rev. Lett. **77**, 2774 (1996).

[99] G. Koster *et al.*, Rev. Mod. Phys. **84**, 253 (2012).

[100] E. A. Yelland *et al.*, Phys. Rev. B **72**, 184436 (2005).

[101] T. Katsufuji and Y. Tokura, Phys. Rev. B **60**, R15021 (1999).

[102] K. S. Takahashi *et al.*, Phys. Rev. Lett. **103**, 057204 (2009).

[103] S. Roy, N. Khan, and P. Mandal, APL Mater. **4**, 026102 (2016).

[104] L. Li *et al.*, Phys. Rev. B **92**, 024109 (2015).

[105] L. Li *et al.*, APL Mater. **2**, 110701 (2014).

[106] V. G. Zubkov *et al.*, J. Alloys Compd. **226**, 24 (1995).

[107] P. V. Prakash Madduri and S. N. Kaul, Phys. Rev. B **95**, 184402 (2017).

[108] M. Nicklas *et al.*, Phys. Rev. Lett. **82**, 4268 (1999).

[109] T. R. Kirkpatrick and D. Belitz, Phys. Rev. B **97**, 064411 (2018).

[110] F. Rivadulla *et al.*, Phys. Rev. B **67**, 165110 (2003).

[111] L. M. Wang, H. E. Horng, and H. C. Yang, Phys. Rev. B **70**, 014433 (2004).

[112] K. Ueda and T. Moriya, J. Phys. Soc. Jpn. **39**, 605 (1975).

[113] S. N. Kaul, J. Phys.: Condens. Matter **17**, 5595 (2005).

[114] A. C. Abhyankar *et al.*, J. Phys.: Condens. Matter **20**, 445227 (2008).

[115] D. L. Mills, A. Fert, and I. A. Campbell, Phys. Rev. B **4**, 196 (1971).

[116] J. Blasco and J. A. Garcia, J. Phys.: Condens. Matter. **6**, 10759 (1994).

[117] C. Krellner *et al.*, Phys. Rev. B **76**, 104418 (2007).

[118] V. N. Nikiforov *et al.*, Eur. Phys. J. B. **86**, 238 (2013).

[119] N. Takeda and M. Ishikawa, J. Phys.: Condens.Matter **15**, L229 (2003).

[120] Z. Wang *et al.*, Phys. Rev. Lett. **117**, 206601 (2016).

[121] V. Fritsch *et al.*, Phys. Rev. B **71**, 132401 (2005).

[122] E. V. Sampathkumaran *et al.*, Phys. Rev. Lett. **91**, 036603 (2003).

[123] R. Mallik *et al.*, Europhys. Lett. **41**, 315 (1998).

[124] Y. Hiranaka *et al.*, J. Phys. Soc. Jpn. **82**, 083708 (2013).

[125] A. Nakamura *et al.*, J. Phys. Soc. Jpn. **84**, 053701 (2015).

[126] M. B. Maple *et al.*, *in Handbook on the Physics and Chemistry of Rare Earths*, edited by K. A. Gschneidner and L. Eyring (North-Holland, Amsterdam, 1978), p. 797.

[127] X. Lin, B. Fauqué, and K. Behnia, Science **349**, 945 (2015).

[128] T. Sarkar, R. L. Greene, and S. Das Sarma, arXiv:1805.08360.

[129] Y. Kususe *et al.*, Jpn. J. Appl. Phys. **53**, 05FJ07 (2014).

[130] K. Rubi *et al.*, Appl. Phys. Lett. **104**, 032407 (2014).

[131] D. X. Li *et al.*, Appl. Phys. Lett. **102**, 152409 (2013).

[132] C. P. Reshmia, S. S. Pillai, K. G. Suresh, M. R. Varma, Journal of Magnetism and Magnetic Materials **324**, 1962-1966 (2012).

[133] Z.-J. Mo *et al.*, J. Alloys Compd. **649**, 674 (2015).

[134] K. Ahn *et al.*, J. Appl. Phys. **106**, 043918 (2009).

[135] K. Ahn *et al.*, J. Appl. Phys. **97**, 063901 (2004).

[136] A. Midya *et al.*, Appl. Phys. Lett. **101**, 132415 (2012).

[137] A. Midya *et al.*, Appl. Phys. Lett. **96**, 142514 (2010).

[138] A. Midya *et al.*, Phys. Rev. B **84**, 235127 (2011).

[139] M. J. Shao *et al.*, Appl. Phys. Lett. **100**, 222404 (2012).

[140] L. H. Yin *et al.*, Appl. Phys. Lett. **104**, 032904 (2014).

[141] M. Balli *et al.*, Appl. Phys. Lett. **104**, 232402 (2014).

[142] M. Annaorazov, *in Double Exchange in Heusler Alloys and Related Materials*, edited by K. Bärner (Research Signpost, Trivandrum, Kerala, India, 2007), p. 117.

[143] J. Liebe *et al.*, Appl. Phys. Lett. **68**, 2343 (1996).

[144] B. J. Kennedy *et al.*, J. Phys.: Condens. Matter **26**, 495901 (2014).

[145] N. Khan *et al.*, Phys. Rev. B **82**, 064422 (2010).

[146] J. Wu and C. Leighton, Phys. Rev. B **67**, 174408 (2003).

[147] T. Samanta, I. Das, and S. Banerjee, Appl. Phys. Lett. **91**, 152506 (2007).

[148] K. Dey *et al.*, J. Mater. Chem. C **5**, 1646 (2017).

[149] Z. J. Mo *et al.*, Appl. Phys. Lett. **102**, 192407 (2013).

[150] A. M. Tishin, *in Handbook of Magnetic Materials, edited by K. H. Buschow,* (Elsevier, Amsterdam, 1999), Vol. 12, p. 395.

[151] E. Palacios *et al.*, Phys. Rev. B **90**, 214423 (2014).

[152] X. Moya *et al.*, Nat. Phys. **11**, 202 (2015).